

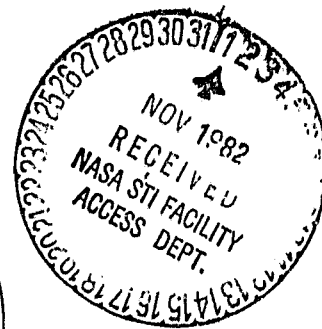
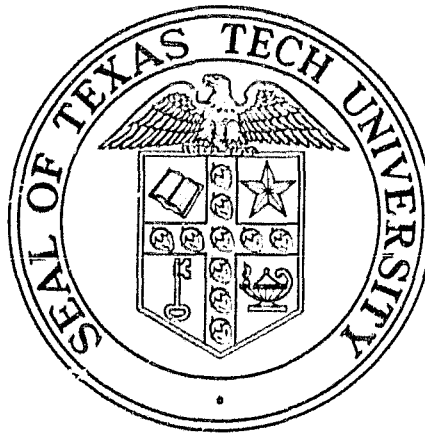
## **General Disclaimer**

### **One or more of the Following Statements may affect this Document**

- This document has been reproduced from the best copy furnished by the organizational source. It is being released in the interest of making available as much information as possible.
- This document may contain data, which exceeds the sheet parameters. It was furnished in this condition by the organizational source and is the best copy available.
- This document may contain tone-on-tone or color graphs, charts and/or pictures, which have been reproduced in black and white.
- This document is paginated as submitted by the original source.
- Portions of this document are not fully legible due to the historical nature of some of the material. However, it is the best reproduction available from the original submission.

# Laboratory Modeling and Analysis of Aircraft-Lightning Interactions

by  
C. D. Turner  
T. F. Trost



Report on  
N.A.S.A. Grant NAG-1-28

August 1982

(NASA-CR-169455) LABORATORY MODELING AND  
ANALYSIS OF AIRCRAFT-LIGHTNING INTERACTIONS  
(Texas Technological Univ.) 168 p  
HC A08/MF A01

N83-10023

CSCL 01C

Unclas  
G3/03 38379

Department of Electrical Engineering  
Texas Tech University  
Lubbock, Texas 79409

LABORATORY MODELING AND ANALYSIS OF  
AIRCRAFT-LIGHTNING INTERACTIONS

by

C. D. Turner  
T. F. Trost

Department of Electrical Engineering  
Texas Tech University  
Lubbock, Texas 79409

August 1982

Prepared for

National Aeronautics and Space Administration  
Langley Research Center  
Hampton, Virginia 23665

Under Grant No. NAG-1-28  
"Lightning Sensors and Data Interpretation"

## TABLE OF CONTENTS

	Page
LIST OF TABLES. . . . .	iv
LIST OF FIGURES . . . . .	v
ABSTRACT. . . . .	viii
I. INTRODUCTION . . . . .	1
II. EXPERIMENTAL AND MEASUREMENT TECHNIQUES. . .	4
Apparatus. . . . .	4
Data Acquisition System. . . . .	6
Data Acquisition Code. . . . .	10
Model and Sensors. . . . .	12
Time Domain Reflectometry. . . . .	28
III. NUMERICAL TECHNIQUES . . . . .	30
Fast Fourier Transform . . . . .	30
Prony Analysis . . . . .	32
Prony Analysis Code. . . . .	40
Stick Modeling . . . . .	42
IV. CIRCULAR CYLINDERS . . . . .	44
V. F-106B SCALE MODEL . . . . .	64
Time Domain Reflectometry. . . . .	64
Current Injection. . . . .	68
Configurations 1 and 2 . . . . .	68
Configuration 3. . . . .	78
Configuration 4. . . . .	83
VI. COMPARISONS WITH IN-FLIGHT DATA. . . . .	100
Overview . . . . .	100

	Page
Direct Strikes. . . . .	101
Nearby Strikes. . . . .	112
VII. CONCLUSIONS . . . . .	123
LIST OF REFERENCES . . . . .	126
APPENDIX I. LISTING OF DATA ACQUISITION CODE. . . . .	129
APPENDIX II. LISTING OF PRONY CODE. . . . .	135

# LIST OF TABLES

Table	Page
4.1. Resonances of Circular Cylinders. . . . .	54
4.2. Natural Frequencies of Circular Cylinders . . . .	60
5.1. Resonances of F-106B Model. . . . .	90
5.2. Resonances of F-106B Model. . . . .	91
5.3. Natural frequencies of F-106b Model . . . . .	97
6.1. F-106B Resonances From In-Flight Direct Lightn- ing Strikes . . . . .	110
6.2. Natural Frequencies From Direct-Strike In-Flight Data. . . . .	111
6.3. F-106B Natural Frequencies From Nearby Lightning Strikes . . . . .	119

## LIST OF FIGURES

Figure	Page
2.1. Modeling apparatus . . . . .	5
2.2. Block diagram of data acquisition system . . . . .	7
2.3. Trigger and window generation circuitry. . . . .	9
2.4. Buffer amplifier circuit with $R = 6.2 \text{ k}\Omega$ , $R' = 27 \text{ k}\Omega$ , and a gain of 10. . . . .	11
2.5. Comparison of model and F-106B . . . . .	13
2.6. Sensor polarities for F-106B model . . . . .	15
2.7. Photograph of F-106B model above the ground plane. . . . .	16
2.8. B-dot sensor and associated circuit and waveforms. . . . .	17
2.9. D-dot sensor and associated circuit and waveforms. . . . .	19
2.10. Conical calibrator . . . . .	22
2.11. Voltage step applied to conical calibrator . . . . .	23
2.12. Output and integrated output for the B-dot sensor . . . . .	24
2.13. Output and integrated output for the 1 cm D-dot sensor . . . . .	26
2.14. Output and integrated output for the 2 cm D-dot sensor . . . . .	27
3.1. Flow chart of Prony code . . . . .	41
4.1. First four cylinder modes. . . . .	45
4.2. Measured waveforms from the thin cylinder. . . . .	47
4.3. Measured waveforms from the thick cylinder . . . . .	48
4.4. Pulse generator output waveform. . . . .	49

4.5.	Transfer function magnitudes for the thin cylinder . . . . .	50
4.6.	Transfer function magnitudes for the thick cylinder . . . . .	51
4.7.	Transfer function phases for the thin cylinder . . . . .	52
4.8.	Transfer function phases for the thick cylinder . . . . .	53
4.9.	Field waveforms for the thin cylinder. . . . .	56
4.10.	Field waveforms for the thick cylinder . . . . .	57
4.11.	Prony analysis results from the circular cylinders. . . . .	59
5.1.	TDR oscillograms for fuselage only . . . . .	65
5.2.	TDR oscillograms for F-106B model. . . . .	66
5.3.	Attachment configurations for the F-106B model .	69
5.4.	Measured waveforms from model configuration 1. .	70
5.5.	Measured waveforms from model configuration 2. .	71
5.6.	Transfer function magnitudes for model configuration 1. . . . .	72
5.7.	Transfer function magnitudes for model configuration 2. . . . .	73
5.8.	Transfer function phases for model configuration 1 . . . . .	74
5.9.	Field waveforms for model configuration 1. . . .	76
5.10.	Field waveforms for model configuration 2. . . .	77
5.11.	Measured waveforms from model configuration 3. .	79
5.12.	Transfer function magnitudes for model configuration 3. . . . .	80
5.13.	Field waveforms for model configuration 3. . . .	82



5.14.	Measured waveforms from model configuration 4 . . .	84
5.15.	Transfer function magnitudes for model configuration 4 . . . . .	85
5.16.	Field waveforms for model configuration 4 . . . . .	86
5.17.	Approximate equivalent circuit for apparatus and model with connecting wires . . . . .	88
5.18.	Stick model configuration . . . . .	92
5.19.	Dominant natural frequencies of model configurations 1 and 2 . . . . .	94
5.20.	Dominant natural frequencies of model configuration 3. . . . .	95
5.21.	Dominant natural frequencies of model configuration 4. . . . .	96
6.1.	B-dot record from direct strike 80-038-01 . . .	.102
6.2.	B-dot record from direct strike 80-038-05 . . .	.103
6.3.	B-dot record from direct strike 80-038-03A. . .	.104
6.4.	B-dot record from direct strike 80-038-03B. . .	.105
6.5.	B-dot record from direct strike 80-038-04 . . .	.106
6.6.	D-dot record from direct strike 80-038-04 . . .	.107
6.7.	D-dot record from direct strike 80-018-01 . . .	.108
6.8.	B-dot record from direct strike 80-026-10 . . .	.114
6.9.	D-dot record from direct strike 80-026-10 . . .	.115
6.10.	D-dot record from nearby strike 81-026-03 . . .	.116
6.11.	D-dot record from nearby strike 81-026-07 . . .	.117
6.12.	F-106B natural frequencies. . . . .	.120
6.13.	F-106B natural frequencies. . . . .	.122

## ABSTRACT

Modeling studies of the interaction of a delta-wing aircraft with direct lightning strikes have been carried out using an approximate scale model of an F-106B. The model, which is three feet in length, is subjected to direct injection of fast current pulses supplied by wires, which simulate the lightning channel and are attached at various locations on the model. Measurements are made of the resulting transient electromagnetic fields using time-derivative sensors. The sensor outputs are sampled and digitized by computer. The noise level is reduced by averaging the sensor output from ten input pulses at each sample time. Computer analysis of the measured fields includes Fourier transformation and the computation of transfer functions for the model. Prony analysis is also used to determine the natural frequencies of the model.

Initially, electric and magnetic field measurements were made with the F-106B model replaced by a simple circular cylinder. Analysis of the waveforms has produced important new information about the effect of wire attachments on scatterers. The natural frequencies of cylinders with wires show much greater damping and slightly higher resonant frequencies than do those of isolated cylinders. The former is due to the wires carrying energy from the cylinder, adding to the radiation damping already present. The latter is due to the wires changing the geometry of the ends, which reduces their capacitance and makes the cylinder electrically shorter. The results concerning the

natural frequencies of the cylinders also give confidence that the basic measurement and analysis technique is correct.

Comparisons of the model transfer functions with spectral amplitudes computed for in-flight data obtained on the F-106B by N.A.S.A. show good agreement regarding the frequencies of the resonances. The frequencies vary somewhat depending on the wire attachment points. The average values are 7.5, 13, 19, 24, 29, 35, and 41 MHz. These frequencies are all matched in in-flight data except for 19 MHz. In flight it is 21 MHz.

Comparisons of model natural frequencies extracted by Prony analysis with those for in-flight direct strike data usually show lower damping in the in-flight case. This is indicative of either a lightning channel with a higher impedance than the wires on the model, only one attachment point, or short streamers instead of a long channel. There is also some in-flight data for nearby strikes. Here the damping should be and is lighter than on the model. For the first natural frequency (7.5 MHz) the normalized damping rate is about -0.16 for the nearby strikes and -0.24 for the model.

## CHAPTER I

### INTRODUCTION

The work presented in this report was carried out as part of the N.A.S.A. Storm Hazards research program. It represents one step toward a general understanding of the electromagnetic environments encountered on aircraft during lightning strikes. The work involves a controlled laboratory experiment using an aircraft model and a comparison of the resulting fields with those observed on the N.A.S.A. F-106B research aircraft during lightning strikes. Exterior electric and magnetic fields have been studied.

The central issue of the report is the nature of the resonances, or natural frequencies, of the aircraft with an attached lightning channel. Resonance is a fundamental physical phenomenon and represents one of several aspects of an aircraft-lightning interaction which are important areas of study. In the in-flight situation, the resonances of the aircraft modify the fields imposed by the lightning by enhancing the spectral components lying at or near the resonance frequencies. Thus, some knowledge of the resonances is necessary for interpreting the measured lightning data. In addition, the lightning channel plays a role in determining the characteristics of the resonances including their frequencies and damping rates. Thus, detailed studies of the resonances observed during lightning strikes can yield information about the channels. The resonances are not the same, for example, as they would be for the case of a

nearby lightning flash or a nuclear EMP, where there is no channel attachment. Of course, the channels have time-dependent and nonlinear properties; our technique does not attempt to model these.

The laboratory measurements were done in the time domain using short pulses. The pulses are applied on a wire, which represents the channel. The technique is similar to that discussed in a Commission A (Electromagnetic Metrology) session at the January, 1982, URSI meeting [1]. It appears that ours is the only time-domain facility where direct current injection is used instead of an incident wave input. Some results from other workers are contained in the references [2,3,4].

Our approach to the evaluation of resonances employs two types of analysis: first, ordinary Fourier spectrum analysis and, second, Prony analysis. These and other techniques have been compared in a recent review paper [5]. The application of the Prony analysis [6-11] derives from the singularity expansion method (SEM) of Baum [12] where the fields on an object are expressed in terms of a set of natural frequencies. Prony's method extracts these natural frequencies from the time-domain waveforms. The concept of natural frequencies has already been used to characterize the response of an aircraft to an EMP [27] and in radar target identification schemes [28,29].

The present investigation is an extension of work reported previously which consisted of the first results from the modeling

experiment [13] and preliminary analysis of in-flight data from the F-106B [14]. A few of the results from this previous work are included in the present report, for the sake of completeness. Several related reports, which are not referenced in the previous work, have also appeared [15-18].

The new contributions of the present work include laboratory measurements of the fields on circular cylinders and on the aircraft model for 4 different wire attachment configurations. Also included is extensive use of Prony analysis on the waveforms from the cylinders and the aircraft model and also from the F-106B for both the 1980 and 1981 flights. The presentation is as follows: Chapter II describes the laboratory measurement techniques. Chapter III describes the Prony (and Fourier) analysis, which is applied in Chapters IV, V, and VI. Chapter IV covers the cylinder results, and Chapter V gives the results for the aircraft model. Chapter VI compares the model results with those from the F-106B. Conclusions are drawn in Chapter VII.

## CHAPTER II

### EXPERIMENTAL AND MEASUREMENT TECHNIQUES

#### Apparatus

The modeling apparatus is shown in Figure 2.1. It consists of a ground plane (12 by 12 feet), pulse generator (Tektronix 109), sampling oscilloscope (Tektronix 561A\*), and a computer for digitizing and recording the data (DEC PDP 11/04). The object under test is located 10 feet above the ground plane, with wires attached to simulate the lightning channel. An approximate scale model of the F-106B, equipped with small B-dot and D-dot sensors for measuring the transient electromagnetic fields, is shown in Figure 2.1 [13].

A pulse of 0.75 ns duration and risetime of 0.25 ns is launched at the bottom of the lower wire. The pulse travels up the lower wire, over the model, and on up the outer conductor of the upper wire, which is actually 0.141 semirigid coaxial cable. The sensor outputs are carried on the inside of this cable. No measurable leakage to the inside of the cable has been detected. This is as it should be since the skin depth for the pulse is two orders of magnitude smaller than the cable wall thickness. When the top of the apparatus is reached, a transition is made to 0.5 inch diameter cable to complete the run back to the sampling oscilloscope, which has an equivalent risetime of 25 ps.

---

\* The following plugins are used: Type 3S2 with S-4 sampling heads and Type 3T2.

ORIGINAL PAGE IS  
OF POOR QUALITY

### APPARATUS FOR AIRCRAFT-LIGHTNING MODELING

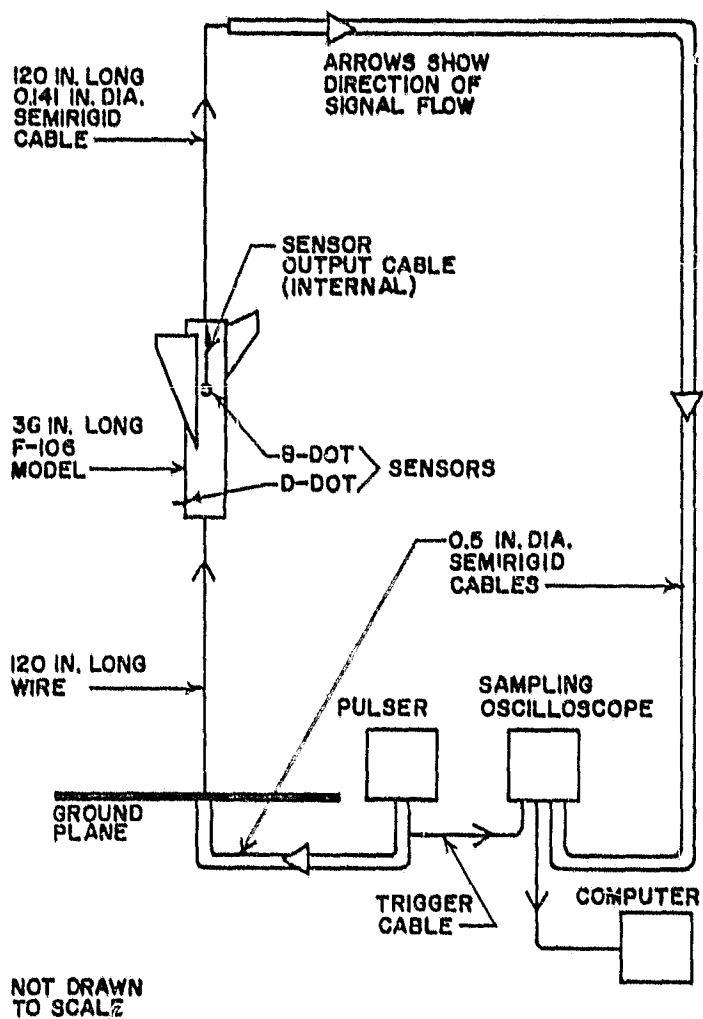


Figure 2.1. Modeling apparatus.



The clear time, or the time before any reflections return to corrupt the data, is 20 ns. This corresponds to the time required for the pulse to reflect from the bottom of the model, travel back down the lower wire and back up to the model after reflecting from the ground plane.

### Data Acquisition System

A detailed block diagram of the data acquisition system is shown in Figure 2.2. The components located between the sampling oscilloscope and computer system were omitted from Figure 2.1 for simplicity. The computer system consists of the computer and floppy disk drive, an A/D converter, a programmable clock, a video alphanumeric and graphics terminal with hard copy unit, and a printing terminal. The A/D converter and programmable clock are special boards which plug directly into the computer backplane. They are both under software control using Fortran subroutines [19]. The A/D converter is a Data Translation DT 1712 which has one 12 bit A/D converter with 8 differential input channels multiplexed into it. The maximum throughput rate is 35 kHz. The input voltage range is  $\pm 10$  volts, so one least significant bit is 4.88 mV. The A/D board requires an external trigger or clock signal to mark the beginning of each conversion. This is supplied by a DEC KW11-K programmable clock. This board contains a 1 MHz crystal controlled oscillator with programmable divider circuitry to produce different clock rates.

The clock can be started by an external trigger pulse, which is the basis for control of the data acquisition

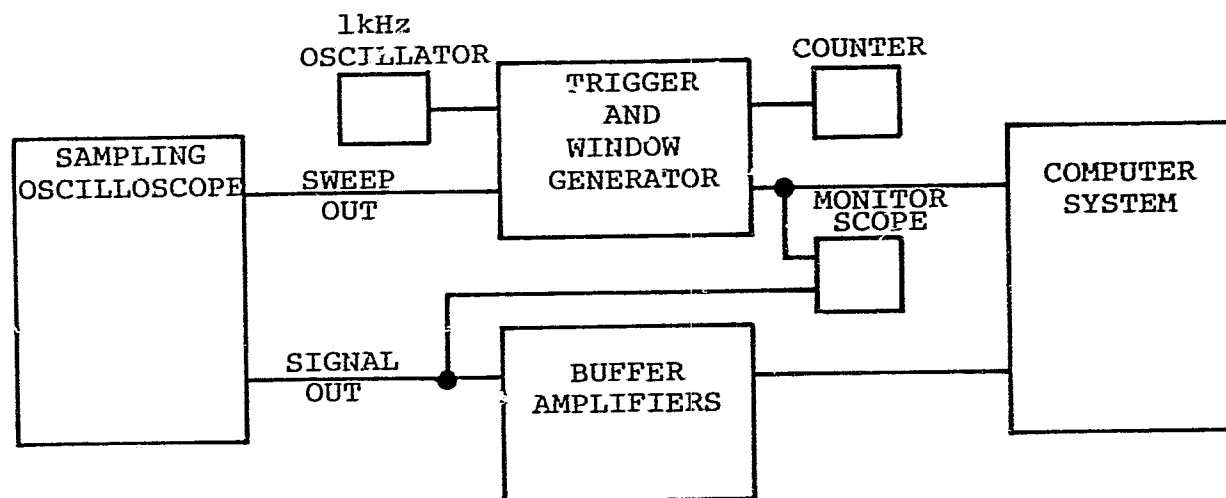
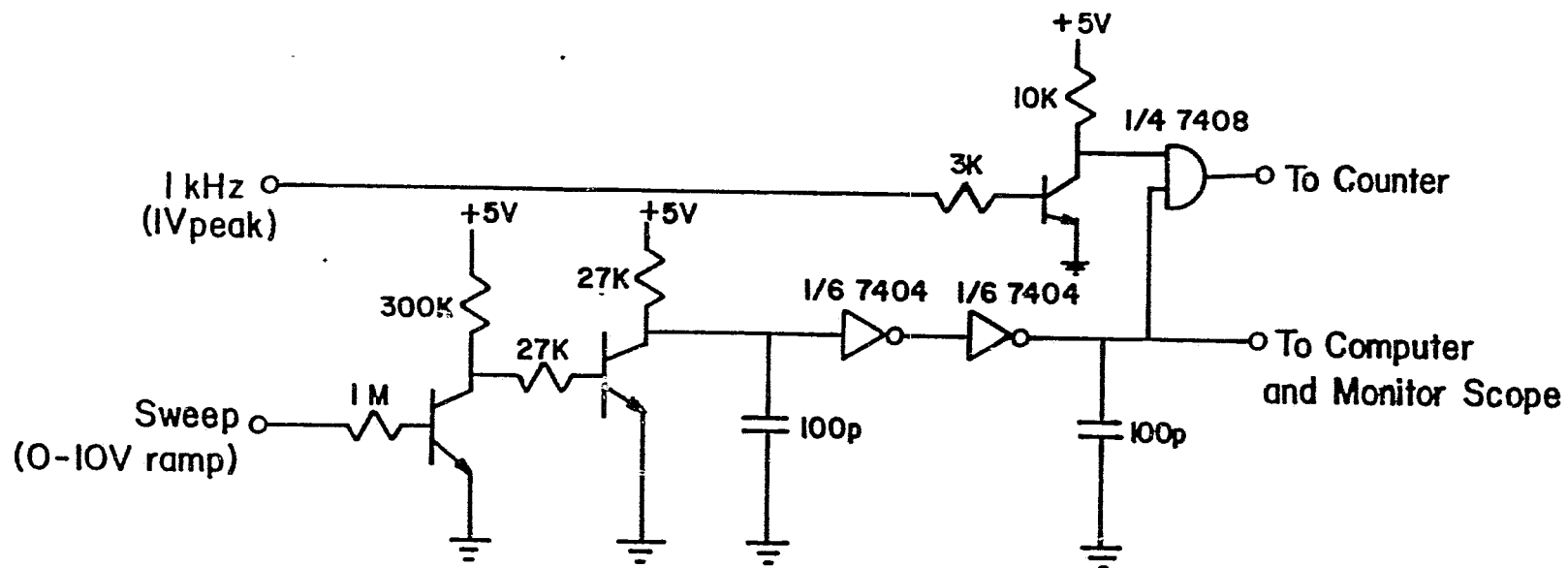


Figure 2.2. Block diagram of data acquisition system.

ORIGINAL PAGE IS  
OF POOR QUALITY

system. The oscilloscope sweep sawtooth is used to generate the "data window" with the trigger and window generation circuitry shown in Figure 2.3. The leading edge of the window is used to trigger the clock. The data window thus determines when data acquisition on a particular sweep will start and how long it will continue. The window actually lasts slightly longer than the 20 ns clear time to make certain that the required number of samples has been taken. The window is also used to measure the actual sweep time of the sampling oscilloscope using the 1 KHz crystal oscillator and counter, and to measure the sweep length by observing the window on the monitor oscilloscope. Since the sampling oscilloscope assembles a waveform from many consecutive signals, its display is not in real time and the actual sweep rate in s/div is needed in order to compute what the clock rate should be to produce the desired equivalent sampling rate. The monitor scope also displays the waveform to be sampled and visually insures that it is entirely within the sampling window.

The oscilloscope displays the sensor signal at an equivalent rate of 2 ns/div and has 10 horizontal divisions covering the 20 ns clear time of the experimental setup. This is to be sampled at an equivalent sampling rate of 20 GHz, corresponding to a sampling interval of 50 ps. This high sampling rate will remove any possibility of aliasing in the data. Since the oscilloscope is sweeping at an equivalent rate of 2 ns/div, 40 samples/div are required for a sampling interval of 50 ps. If the actual sweep rate of the oscilloscope is



ALL TRANSISTORS 2N2222

Figure 2.3. Trigger and window generation circuitry.

measured to be  $T$  sec/div, then the sampling rate of the A/D converter should be

$$R = 40/T \quad \text{samples/sec.}$$

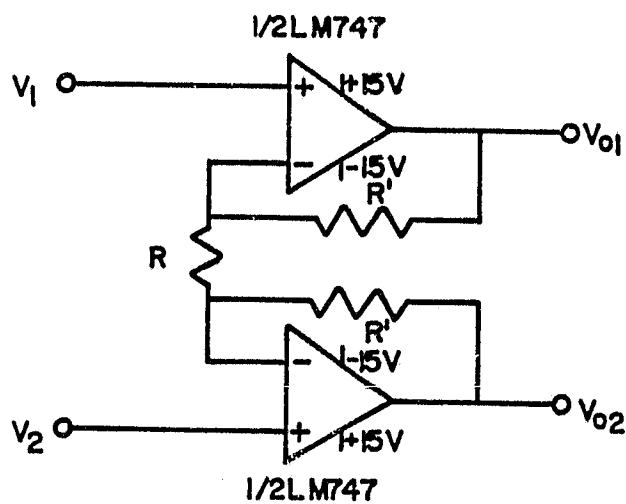
In order to achieve a jitter free display, the sampling oscilloscope itself is set internally to run at the fixed rate of 100 samples/div. This gives an actual sweep rate for the oscilloscope of approximately 0.13 sec/div and an actual sampling rate of about 308 samples/sec.

The vertical outputs of the sampling oscilloscope have a 10 k ohm output impedance which is too high to allow proper settling time for the input multiplexers. The settling time is the time for the charge injected into the input lines by the solid state multiplexers to settle to less than  $1/2$  of one LSB of error. This is a function of the cable capacitance and the source impedance time constant. So, if a high source impedance is present, only very short input cables can be used. To alleviate this problem, buffer amplifiers of the type shown in Figure 2.4 have been designed and constructed. They are double ended on both input and output. They have a high input impedance to avoid loading the oscilloscope and a low output impedance to solve the settling time problem. They also are used to adjust the gain of the signal from the oscilloscope in order to utilize the entire  $\pm 10$  volt dynamic range of the A/D converter.

#### Data Acquisition Code

The data acquisition code written in Fortran is given in Appendix I. The code actually acquires 11 successive sweeps

ORIGINAL PAGE IS  
OF POOR QUALITY



$$V_{01} - V_{02} = (1 + 2R'/R)(V_1 - V_2)$$

Figure 2.4. Buffer amplifier circuit with  $R = 6.2 \text{ k}\Omega$ ,  $R' = 27 \text{ k}\Omega$ , and a gain of 10.

from the oscilloscope. The first is ignored to allow the triggering of the sampling sweep to stabilize. The last ten are averaged point by point in order to reduce the baseline noise in the measurement. This averaged waveform is then stored on magnetic disk. Detailed operator instructions for running the code are given elsewhere [20].

### Model and Sensors

The approximate scale model of the F-106B delta-wing aircraft is constructed as follows: The fuselage consists of a 3 foot length of aluminum cylinder, 4 inches in diameter. Flat end caps are machined to fit into each end and are secured with screws. The wings and tail are cut from 1/16 inch brass sheet to scale with the aluminum cylinder. The overall scale of the model is 1/18.8 of the actual F-106B. A comparison of the model to the actual aircraft is shown in Figure 2.5. The agreement is quite good except in the cockpit area. No attempt has been made to include the cockpit on the scale model and the effect of its omission on the external response of the model is expected to be slight.

Two B-dot sensors and one D-dot sensor have been placed on the model in the locations corresponding to their actual locations on the F-106B. The B-dot sensors, one sensitive to longitudinal currents and one to transverse currents\*, are on the fuselage over the starboard and port wings, respectively.

---

\* We follow the terminology used by N.A.S.A. for the sensors on the airplane: "longitudinal" and "transverse" refer to the direction of current, not the direction of B.

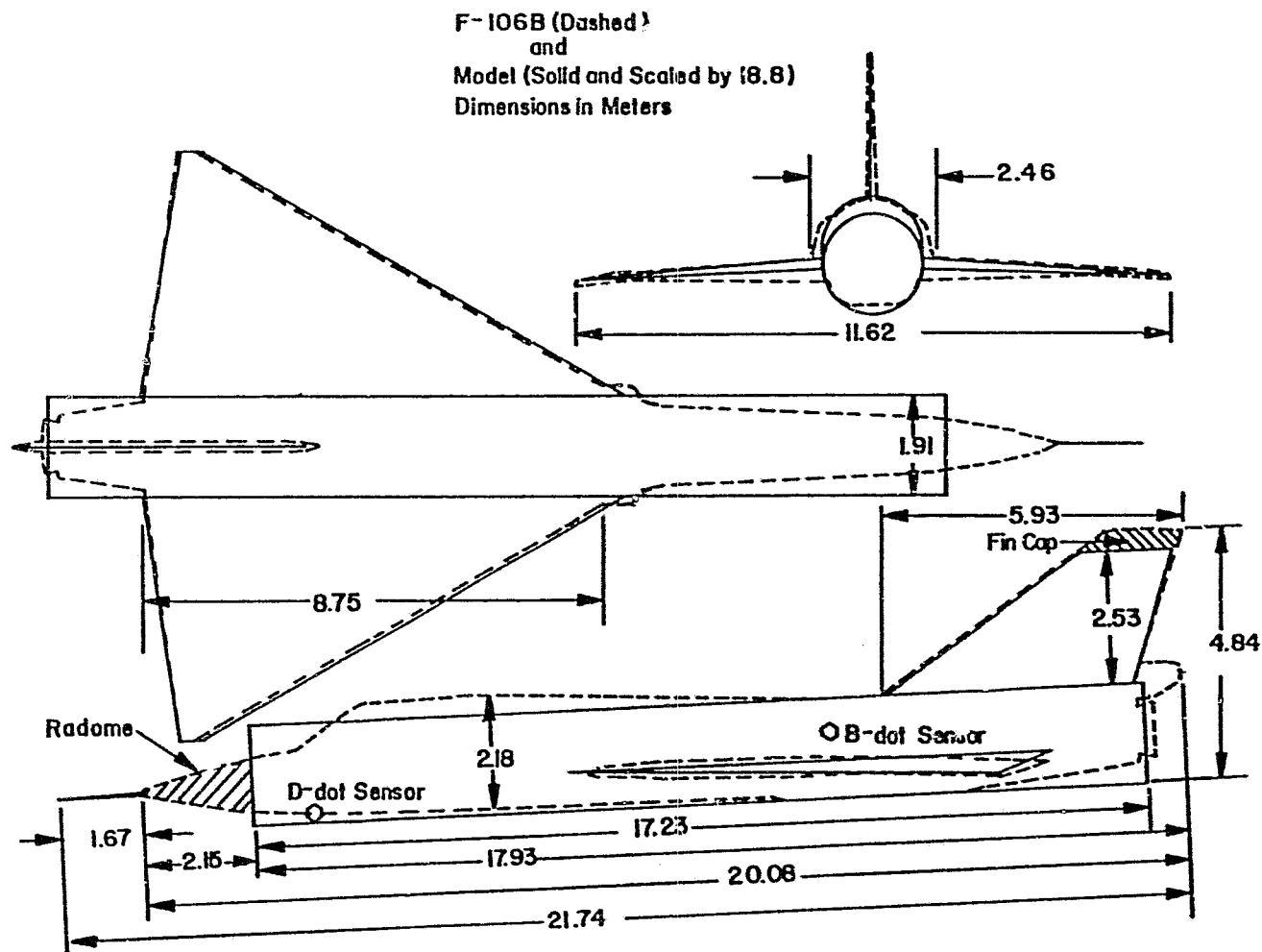


Figure 2.5. Comparison of model and F-106B.



The D-dot sensor is under the nose or chin of the aircraft. The output polarities for these sensors are shown in Figure 2.6. Current increasing fore to aft produces a negative response from the longitudinal B-dot sensor, as does current flow from starboard to port for the transverse B-dot sensor. Electric field increasing in the outward normal direction produces a positive response from the D-dot sensor. A photograph of the model in position above the ground plane is shown in Figure 2.7. Wires are attached to the forward and rear fuselage as was shown in Figure 2.1. The two B-dot sensors can also be seen in the photograph.

The B-dot sensor is shown in Figure 2.8, along with its equivalent circuit and its response to a step magnetic field. It is a loop made by bending 0.141 inch diameter semirigid coaxial cable into a 0.9 cm mean radius semicircle and cutting a gap in the outer conductor. The size of the sensor has to be chosen large enough to obtain adequate sensitivity but small enough so the bandwidth will be adequate. It should also be small with respect to dimensions on the model. This radius, 0.9 cm, is the smallest radius in which the 0.141 cable can be bent without damage. Simple current estimates for the model indicated that this should be large enough for adequate signal. The bandwidth,  $f_0$ , is calculated from the inductance by assuming the simple equivalent circuit in Figure 2.8b, loaded by the 50 ohm line. The output falls by 3 dB when  $2\pi f_0 L$  equals 50 ohms, which is the expression for  $f_0$ . Also, the sensor risetime can be

ORIGINAL PAGE IS  
OF POOR QUALITY

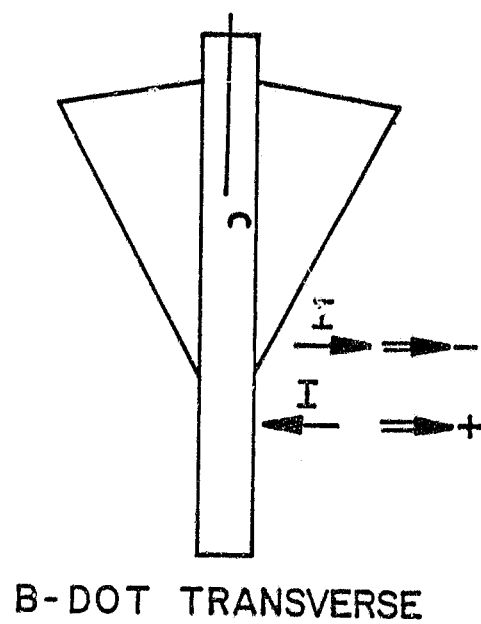
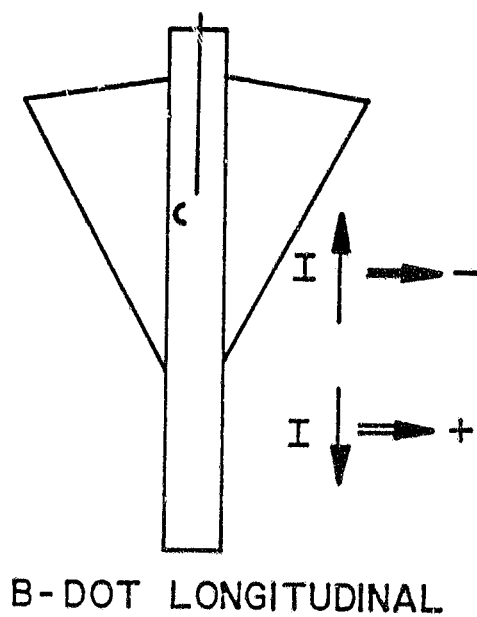
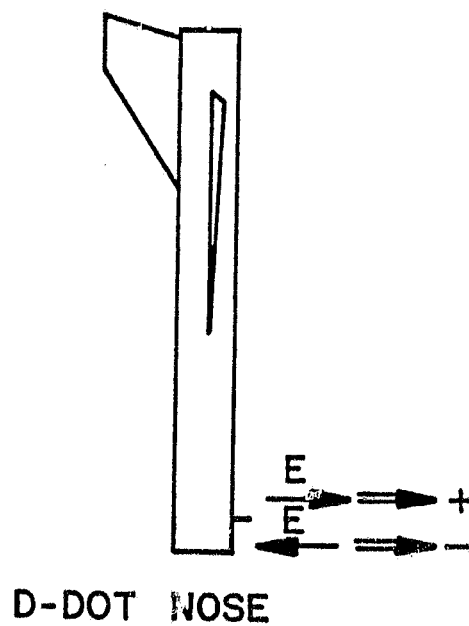


Figure 2.6. Sensor polarities for F-106B model.

ORIGINAL FILE IS  
OF POOR QUALITY

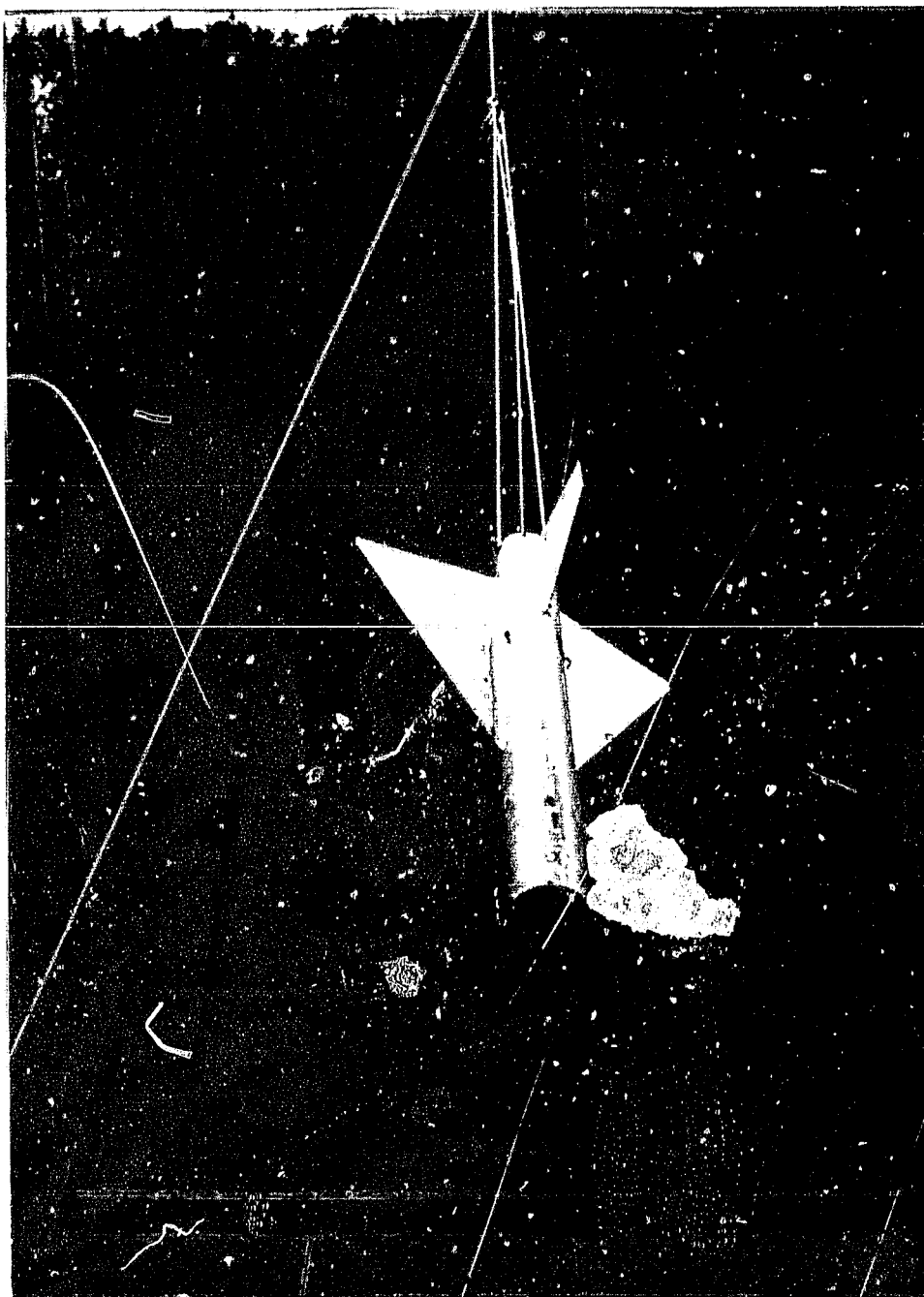
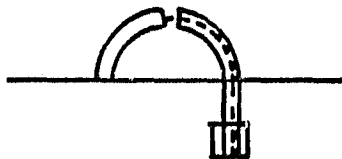
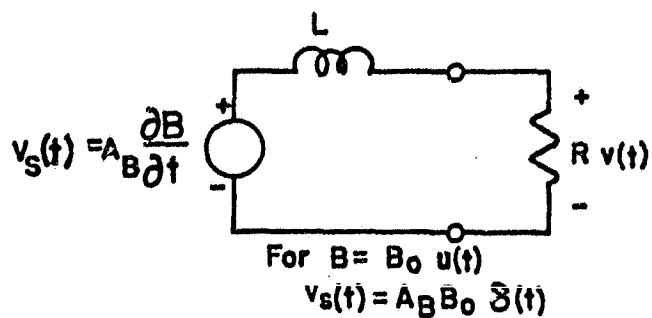


Figure II-7. Photograph of F-106B model above the ground plane.

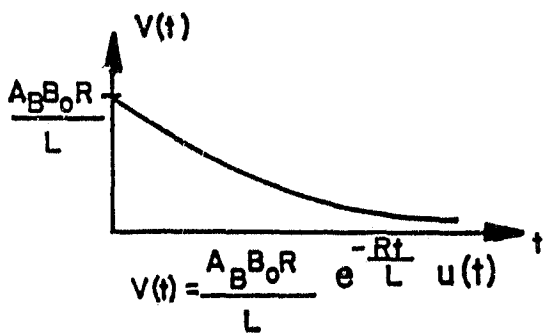
ORIGINAL PAGE IS  
OF POOR QUALITY



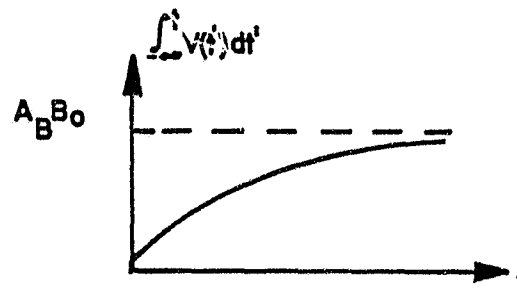
a. Sensor



b. Equivalent circuit



c. Output voltage for step input



d. Integrated output voltage

Figure 2.8. B-dot sensor and associated circuit and waveforms.

calculated using the formula  $t_r f_o = 0.35$ . The inductance of the semicircular loop can be calculated by using the formula [21]:

$$L \approx \frac{1}{2} \frac{2\pi g}{10^9} \left( \ln \frac{4g}{r} - \frac{7}{4} \right) \quad \text{for } r \ll g$$

where

$g$  = mean diameter of loop (cm)

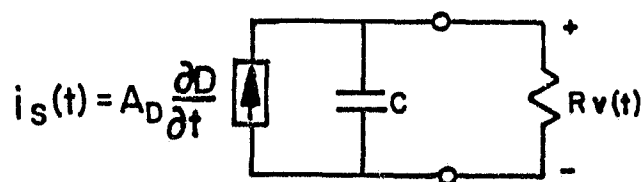
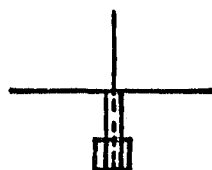
$r$  = radius of wire (cm).

The factor  $1/2$  is put in since the sensor is a semicircular loop on a ground plane. Here, with  $r = 0.1791$  cm (0.0705 in) and  $g = 1.8$  cm (0.7 in),  $L = 1.1 \cdot 10^{-8}$  H. Thus, the bandwidth is  $f_o = 50/2\pi L = 724$  MHz, and the risetime is  $t_r = 0.35/f_o = 484$  ps.

The sensitivity (or equivalent area) of the B-dot sensor,  $A_B$ , can be approximated by the geometrical area of the loop. The area is  $1/2(\pi r^2)$ , where  $r = 0.9$  cm, so  $A_B = 1.27 \cdot 10^{-4}$  m<sup>2</sup>.

The D-dot sensor is shown in Figure 2.9, along with its equivalent circuit and response to a step electric field. It is simply a 1 or 2 cm monopole antenna with a small ground plane. It was determined that these lengths would provide adequate sensitivity using some electric field estimates on the model. The monopole needs to be short enough, though, so that errors due to the fact that the field falls off as  $1/r$  from the cylindrical surface will be negligible. The same is true of the B-dot sensor described above. Indeed, these errors are slight as determined by calculations of correction factors due to the  $1/r$  field variation. Unlike the B-dot sensor, neither the effective area nor the bandwidth can be calculated for this

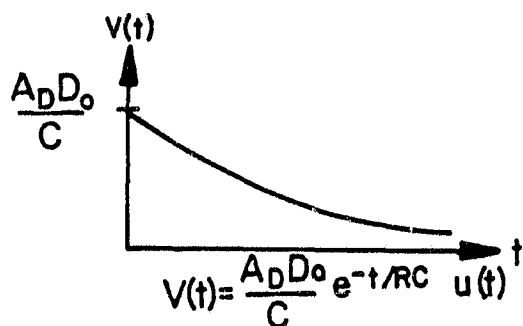
ORIGINAL PAGE IS  
OF POOR QUALITY



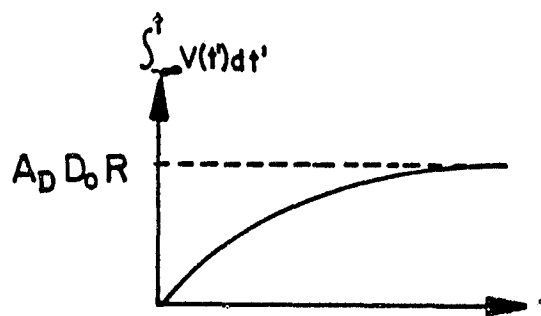
For  $D = D_0 u(t)$   
 $i_s(t) = A_D D_0 \delta(t)$

a. Sensor

b. Equivalent circuit



c. Output voltage for step input



d. Integrated output voltage

Figure 2.9. D-dot sensor and associated circuit and waveforms.

D-dot sensor. The effective length can be assumed to be equal to the physical length, but this is related to the effective area by the capacitance which cannot be calculated.

In order to calibrate the sensors, measuring the effective areas and risetimes of each, the sensors may be exposed to a B- or D- field with a step change in time. The sensor output resulting from the step is integrated and  $A_B$  or  $A_D$  found from the final value reached by this integral. This is shown in Figures 2.8 and 2.9, where  $B_0$  and  $D_0$  are the values reached by the magnetic and electric fields at the sensors. The equations are almost identical in the two cases. In Figure 2.8, the B-field is given in terms of the unit step,  $u(t)$ , and the sensor voltage source then contains an impulse function,  $\delta(t)$ . The sensor output voltage computed from the equivalent circuit is shown in Figure 2.8c. The impulse charges the inductor instantaneously, followed by an exponential decay. The final value of the integral, from Figure 2.8d, is  $A_B B_0$  from which  $A_B$  is obtained. The same procedure is applied in a dual manner to the D-dot sensor in Figure 2.9, except that the final value of the integral is  $A_D D_0 R$ . The sensitivity of the D-dot sensor is then  $A_D R \text{ V/(A/m}^2\text{)}$ .

The bandwidth of each sensor can be computed by measuring the 10% to 90% risetime of the integrated output, and then applying the formula  $t_r f_0 = 0.35$ .

The sensor calibration is done on the conical transmission line calibrator shown in Figure 2.10. It consists of a conical section of transmission line formed by the conical monopole and the 12 x 12 foot ground plane. The electromagnetic fields produced on this line can be calculated by using the formulas [22]:

$$B_{\phi}(r, \theta) = \frac{\mu_0 I}{2\pi r \sin \theta} \quad D_{\theta}(r, \theta) = \frac{\epsilon_0 \eta V}{2\pi r K \sin \theta}$$

where

V = voltage on cone  
 I = current on cone  
 r = radial distance to point of interest  
 $\theta$  = polar angle to point of interest  
 $\eta$  = impedance of free space = 377 ohms  
 K = impedance of conical line =  $\eta/2\pi \ln \cot \psi/2$   
 $\psi$  = cone half-angle.

The sensor under test is placed on the ground plane in the location shown, which gives maximum clear time, 8 ns. A step is applied to the cone producing a spherical electromagnetic wave with fields described by the above equations. The step is shown in Figure 2.11. It has a very fast rise to approximately 90% and then a slow increase after that which seems characteristic of line type pulse generators.

The output and integrated output for the B-dot sensor are shown in Figure 2.12. For this measurement, the sensor was placed only 2 feet from the cone rather than 4 in order to obtain adequate signal. The sensitivity of the sensor is determined by the final value of the integrated output, as described above. This value is equated to  $A_B B_0$ , where



ORIGINAL PAGE IS  
OF POOR QUALITY

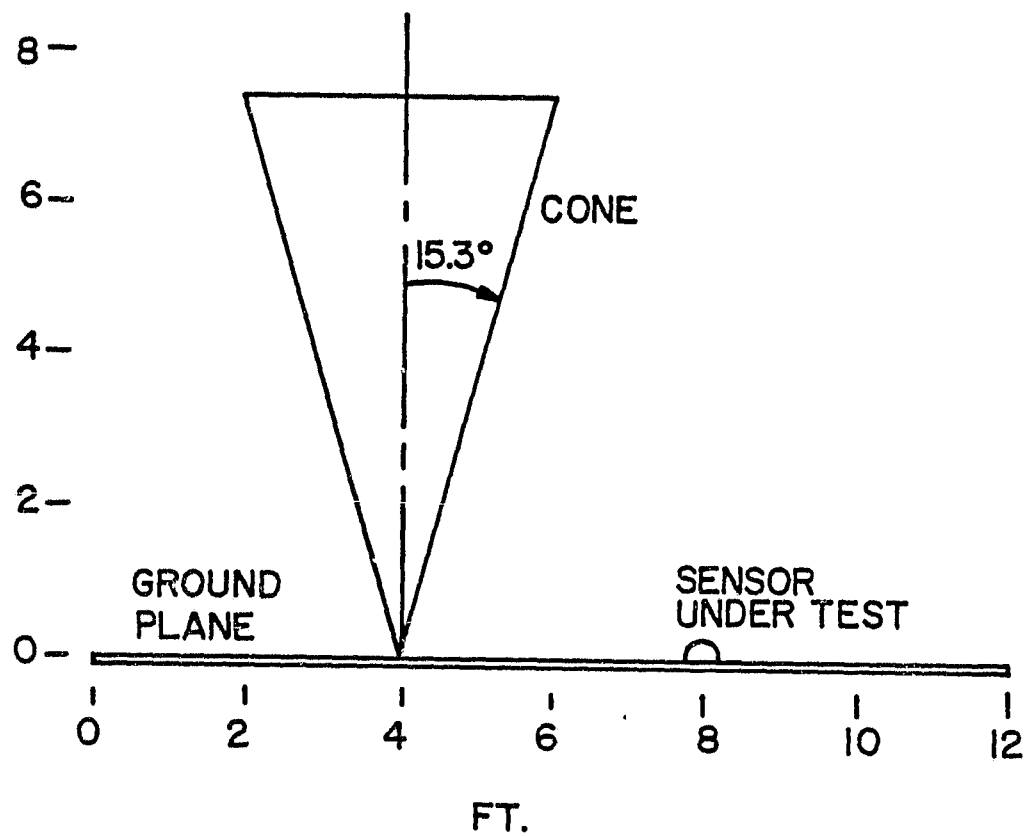


Figure 2.10. Conical calibrator.

ORIGINAL PAGE IS  
OF POOR QUALITY

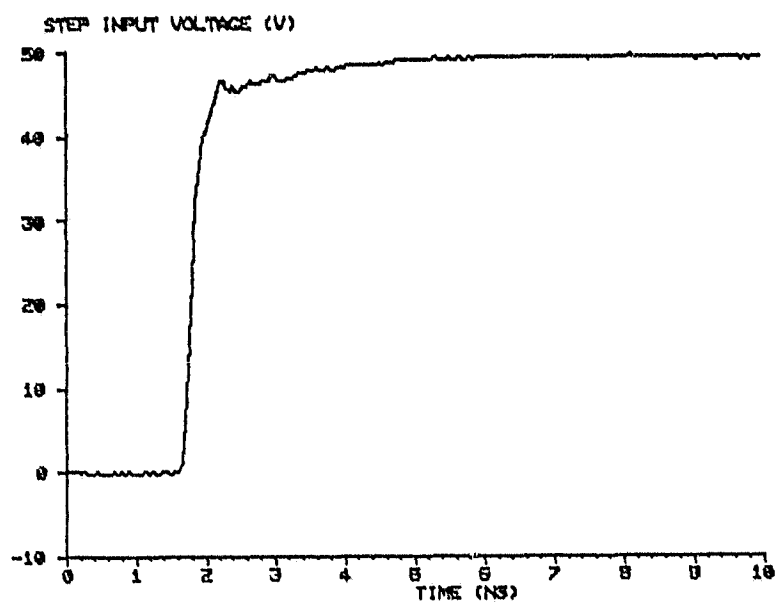


Figure 2.11. Voltage step applied to conical calibrator.

ORIGINAL PAGE IS  
OF POOR QUALITY

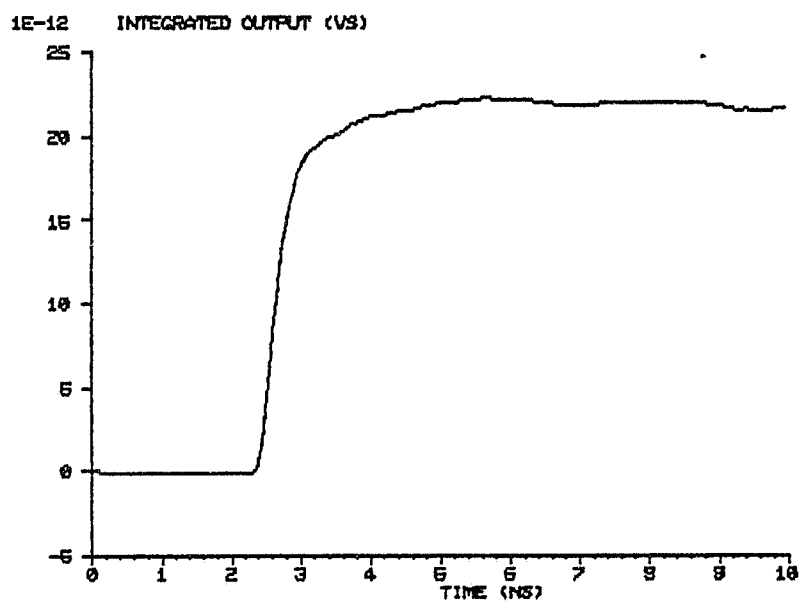
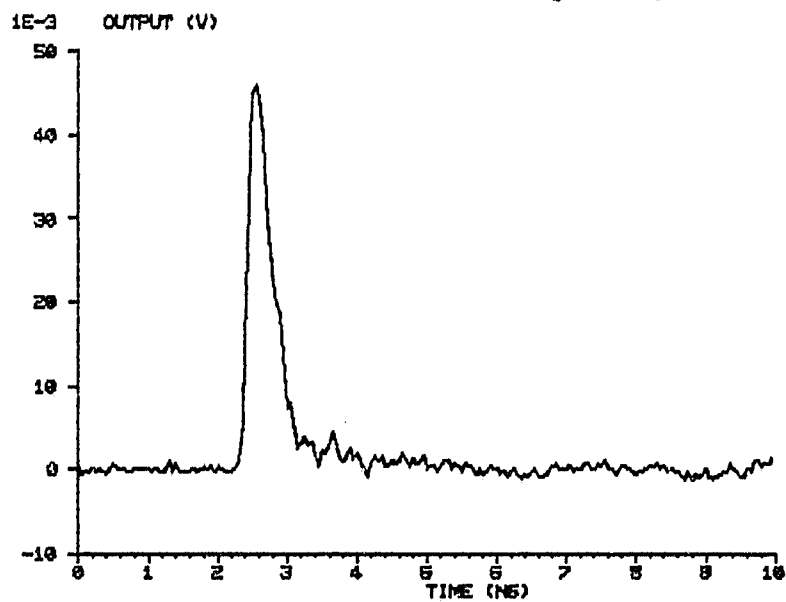


Figure 2.12. Output and integrated output for the B-dot sensor.

$B_0$  is the value reached by the magnetic field at the sensor. For the position 2 feet from the cone,  $B_0 = 1.97 \cdot 10^{-7}$  T. The final value of the integral is  $21.9 \cdot 10^{-12}$  vs, giving the effective area  $A_B = 1.11 \cdot 10^{-4}$  m<sup>2</sup>. This is somewhat less than that computed using the geometrical area. This indicates that for this type of B-dot sensor, the effective area is about 14% below the mean geometrical area.

In order to account for the risetime of the pulse generator and measurement system, the risetime of the sensor can be estimated by using the following method [23]:

$$t_{r_{\text{total}}}^2 = t_{r_{\text{system}}}^2 + t_{r_{\text{sensor}}}^2$$

so

$$t_{r_{\text{sensor}}} = \sqrt{t_{r_{\text{total}}}^2 - t_{r_{\text{system}}}^2}$$

From Figure 2.11, the system risetime is 350 ps. From Figure 2.12, the total risetime of the B-dot sensor is 670 ps, giving an sensor risetime of 570 ps and a bandwidth of  $f_0 = 615$  MHz, lower than that predicted by the inductance calculation above.

The outputs and integrated outputs for the 1 cm and 2 cm D-dot sensors are shown in Figures 2.13 and 2.14, respectively. Similar calculations to those above for the B-dot sensor yield a sensitivity of  $8.89 \cdot 10^{-3}$  V/(A/m<sup>2</sup>) for the 1 cm sensor and  $22.8 \cdot 10^{-3}$  V/(A/m<sup>2</sup>) for the 2 cm sensor. As

ORIGINAL PAGE IS  
OF POOR QUALITY

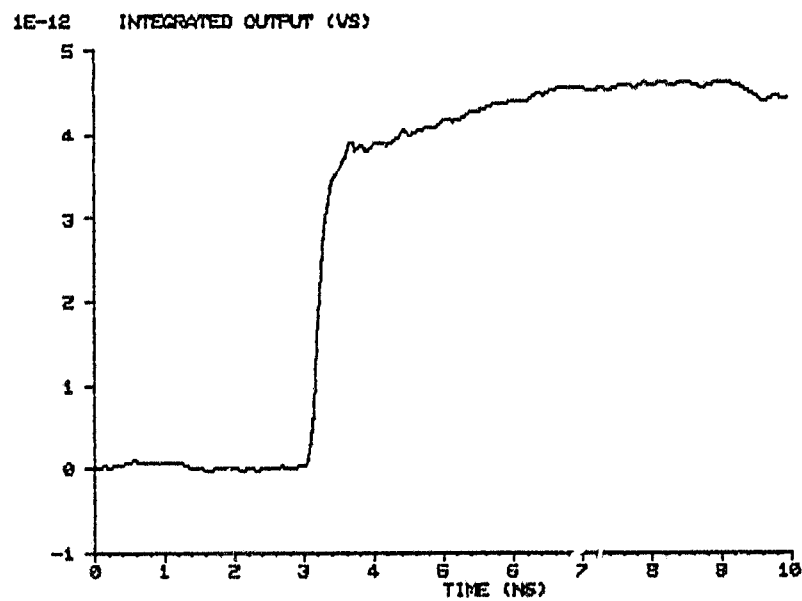
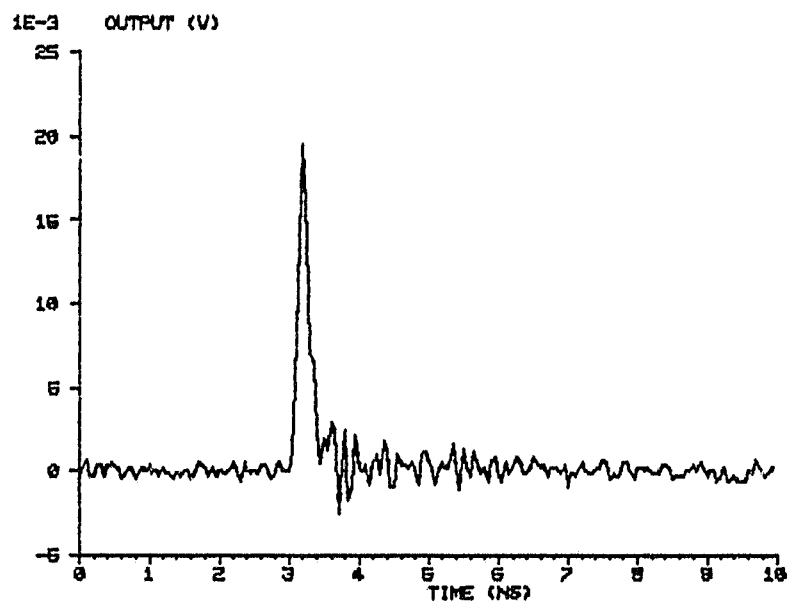


Figure 2.13. Output and integrated output for the 1 cm D-dot sensor.

ORIGINAL PAGE IS  
OF POOR QUALITY

27

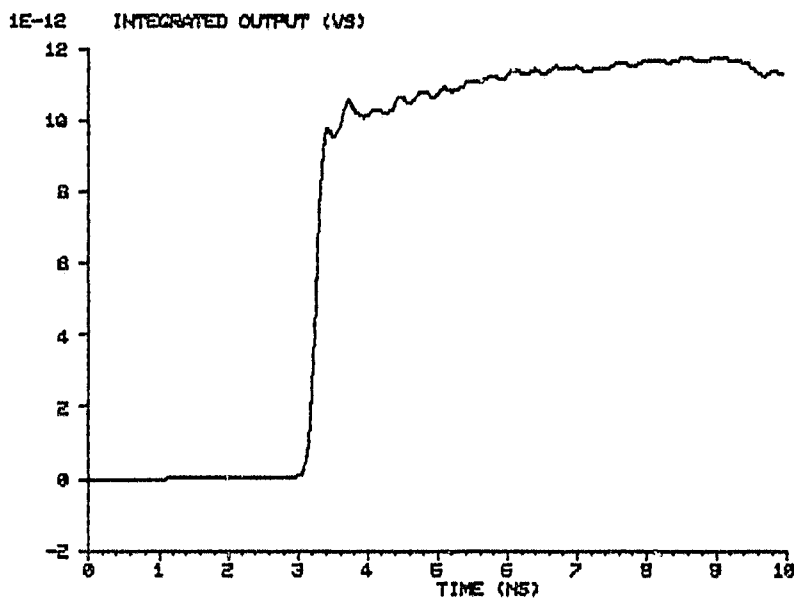
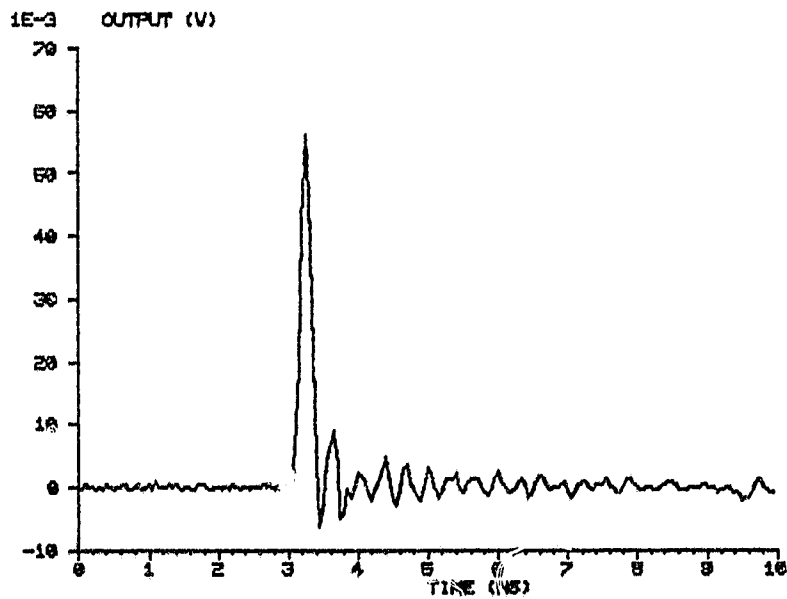


Figure 2.14. Output and integrated output for the 2 cm D-dot sensor.

noted earlier, the effective length of the monopole is related to the effective area by the capacitance as follows:

$$A_D = \frac{l_e C}{\epsilon_0}$$

If the effective length is assumed to be the physical length, then the capacitance can be calculated using the above formula and the effective area calculated above. If this is done, the values are  $C = 1.54 \cdot 10^{-13}$  F for the 1 cm sensor and  $C = 2.1 \cdot 10^{-13}$  F for the 2 cm sensor. The bandwidth of the sensors can then be estimated in a manner similar to that used for the B-dot sensor. The bandwidth is calculated by assuming the equivalent circuit shown in Figure 2.9b, loaded by the 50 ohm line. The output falls by 3 dB when  $1/(2\pi f_0 C)$  equals 50 ohms. The risetime can then be calculated using  $t_r f_0 = 0.35$ . This yields a risetime of 16.9 ps for the 1 cm sensor and 23.1 ps for the 2 cm sensor. These are more than an order of magnitude below the system risetime so they cannot be measured on the calibration system. Thus, the bandwidth of the model measurements will not be limited by the D-dot sensors but only by the B-dot sensor.

### Time Domain Reflectometry

The technique of Time Domain Reflectometry (TDR) can be used to learn a considerable amount about the response of the F-106B to an electromagnetic transient. The technique consists of launching a fast risetime voltage step along the input line to the model and observing the reflec-

tions with a sampling oscilloscope. The TDR display is then a plot of the magnitude of the reflection coefficient ( $\rho$ ) versus time. The equipment used here is the Tektronix 7603 oscilloscope with the 7S12 TDR/sampler plug-in. The 7S12 uses the S-52 pulse generator head ( $t_r = 25$  ps) and the S-6 sampling head ( $t_r = 30$  ps). The results from this technique will be presented in a later chapter.



### CHAPTER III

#### NUMERICAL TECHNIQUES

The numerical methods used in analysis of the data measured in the laboratory and the in-flight data are the fast Fourier transform (FFT) and Prony analysis. A stick modeling technique for the aircraft is also used in an attempt to calculate the natural resonances of the F-106B for comparison with measurements.

#### Fast Fourier Transform

The FFT performs a fast calculation of the discrete Fourier transform (DFT) on an N-point real data sequence  $f_0, f_1, \dots, f_{N-1}$  using the following summation:

$$F_K = \sum_{n=0}^{N-1} f_n e^{-j2\pi nK/N} \quad \text{for } K = 0, 1, \dots, N-1$$

Similarly, the inverse DFT is calculated using:

$$f_n = \sum_{K=0}^{N-1} F_K e^{j2\pi nK/N} \quad \text{for } n = 0, 1, \dots, N-1$$

The finite data sequence to which the FFT is to be applied may be viewed as being obtained by windowing an infinite length sequence with a cutoff function. Multiplication in the time-domain by this window function means the resulting transform is the convolution of the desired transform with the transform of the window function. In the

case of a rectangular window, sidelobes characteristic of the  $(\sin \pi f)/\pi f$  function are introduced. Therefore, the implicit assumption that the data outside the window is zero introduces leakage or power spreading into adjacent frequency regions.

The data windowing also determines the frequency resolution of the FFT. The resolution is limited to the main lobe width of the window transform. For the rectangular window, the width of the main lobe of its transform,  $(\sin \pi f)/\pi f$ , is approximately the inverse of the observation time in seconds, or  $1/N\Delta t$  Hz.

Zero padding, or adding zeros to the end of a data sequence before transforming, will serve to interpolate the spectral values between those which would have been obtained otherwise. In this way, the appearance of the spectrum can be smoothed. Also, padding can help to resolve ambiguities in the spectrum and to reduce quantization error in the estimate of frequencies of spectral peaks [5].

The FFT is used in this work for spectral analysis and to compute transfer functions, i.e., to deconvolve the pulse generator output from the measured field waveforms. Since the input waveform has no frequency content above 1500 MHz, the transfer functions become noisy and meaningless above this frequency. For this reason, the transfer functions are low pass filtered there.

### Prony Analysis

The introduction of the singularity expansion method (SEM) [12] as a procedure for representing and calculating the transient electromagnetic response of antennas and scatterers has had tremendous impact on the field of electromagnetics. Its development was stimulated by observation of the transient responses of various complicated scatterers, especially aircraft. The impulse response waveforms of these objects are dominated by a few exponentially damped sinusoids.

The Laplace transform of each damped sinusoid contains a pair of complex conjugate poles in the complex frequency plane. The poles represent the damped sinusoids and are intrinsic to the object; they are called the natural frequencies of the object. Under broadband excitation, the object will have a large response at frequencies near its poles. The charge, current, or field distribution associated with each natural frequency is called a natural mode. The natural frequencies and mode distributions are characteristic of the object alone and are not functions of the input (incident field or current). The amplitude coefficients of the natural modes of course do depend on the input. In the case of lightning striking an aircraft, the lightning channel and the aircraft constitute the object. Thus a change in channel attachment points would change the natural frequencies. The lightning current is the input and determines the degree of excitation of the various modes.

Prony analysis [6-8] is a technique for extracting the poles (natural frequencies) and residues (containing mode information) of an object directly from its time-domain response. The method involves the use of Prony's algorithm for fitting a sum of complex exponentials to a curve and some other techniques to ensure that the results are physical. Once the poles and residues have been obtained, the impulse response or the frequency-domain transfer function could be determined without the use of a Fourier transform.

For a continuous signal  $I(t)$ , the sum may be written as

$$I(t) = \sum_{m=1}^N A_m e^{s_m t}$$

where the  $s_m$ 's are the poles and the  $A_m$ 's the residues, both complex. For a discrete (or sampled) signal  $I(t_n)$ ,

$$I(t_n) = \sum_{m=1}^N A_m e^{s_m n \Delta t} \quad (3.1)$$

Here,  $\Delta t$  is the sampling interval of the waveform which contains  $2N$  points.  $N$  is the number of terms in the expansion, generally referred to as the number of degrees of freedom in the waveform. The waveform is chosen to have  $2N$  points for a specific reason which will become apparent later.

For the type of transient waveforms discussed earlier which tend toward zero as time increases, the real parts of the poles will be negative. Thus, the expansion is seen to be a series of damped sinusoids. Also, the resulting waveform must be real, and therefore the residues will occur in complex conjugate pairs as will the poles. Prony's algorithm for computing the poles and residues for a given waveform is described in the following. For later convenience, write Eq. (3.1) as

$$I_n = \sum_{m=1}^N A_m (e^{S_m \Delta t})^n = \sum_{m=1}^N A_m z_m^n, \text{ for } n = 0, 1, \dots, 2N-1 \quad (3.2)$$

Now, consider a polynomial of the form

$$(z-z_1)(z-z_2) \dots (z-z_N) = 0,$$

where the  $z_m$ 's are those of Eq. (3-2). The polynomial may be written as

$$\sum_{p=0}^N \alpha_p z^p = 0$$

or

$$\alpha_0 + \alpha_1 z + \alpha_2 z^2 + \dots + \alpha_N z^N = 0 \quad (3.3)$$

The roots of this polynomial will be related to the poles by

$$\begin{aligned} z_m &= e^{S_m \Delta t} \\ S_m &= \frac{1}{\Delta t} \ln z_m \end{aligned} \quad (3.4)$$

Now, the  $\alpha$ 's must be found, and then the poles will be given by the zeros of Eq. (3.3). For the discrete case, Eq. (3.1) must hold for each of the  $2N$  points in the waveform. Therefore

$$\begin{aligned} I_0 &= A_1 + A_2 + \dots + A_N \\ I_1 &= A_1 z_1 + A_2 z_2 + \dots + A_N z_N \\ I_2 &= A_1 z_1^2 + A_2 z_2^2 + \dots + A_N z_N^2 \\ &\vdots \\ I_{2N-1} &= A_1 z_1^{2N-1} + A_2 z_2^{2N-1} + \dots + A_N z_N^{2N-1} \end{aligned} \quad (3.5)$$

Multiplying the first equation in Eq. (3.5) by  $\alpha_0$ , the second by  $\alpha_1$ , and so on until multiplying the  $N$ th by  $\alpha_N$ , and adding the resulting  $N+1$  equations gives the following:

$$\begin{aligned} \alpha_0 I_0 &= \alpha_0 A_1 + \alpha_0 A_2 + \dots + \alpha_0 A_N \\ \alpha_1 I_1 &= \alpha_1 A_1 z_1 + \alpha_1 A_2 z_2 + \dots + \alpha_1 A_N z_N \\ \alpha_2 I_2 &= \alpha_2 A_1 z_1^2 + \alpha_2 A_2 z_2^2 + \dots + \alpha_2 A_N z_N^2 \\ &\vdots \\ \alpha_N I_N &= \alpha_N A_1 z_1^N + \alpha_N A_2 z_2^N + \dots + \alpha_N A_N z_N^N \end{aligned}$$

---


$$\sum_{p=0}^N \alpha_p I_p = 0$$

The right hand side is zero due to Eq. (3.3). Similarly,

multiplying the second equation in Eq. (3.5) by  $\alpha_0$ , the third by  $\alpha_1, \dots$ , and the  $(N+1)^{th}$  by  $\alpha_N$ , and adding the resulting equations gives

$$\begin{aligned}\alpha_0 I_1 &= \alpha_0 A_1 Z_1 + \alpha_0 A_2 Z_2 + \dots + \alpha_0 A_N Z_N \\ \alpha_1 I_2 &= \alpha_1 A_1 Z_1^2 + \alpha_1 A_2 Z_2^2 + \dots + \alpha_1 A_N Z_N^2 \\ \alpha_2 I_3 &= \alpha_2 A_1 Z_1^3 + \alpha_2 A_2 Z_2^3 + \dots + \alpha_2 A_N Z_N^3 \\ &\vdots \\ \alpha_N I_{N+1} &= \alpha_N A_1 Z_1^{N+1} + \alpha_N A_2 Z_2^{N+1} + \dots + \alpha_N A_N Z_N^{N+1}\end{aligned}$$


---

$$\sum_{p=0}^N \alpha_p I_{p+1} = 0$$

The right hand side is again zero due to Eq. (3.3). Continuing this procedure  $N$  times, yields on the  $N^{th}$

$$\begin{aligned}\alpha_0 I_{N-1} &= \alpha_0 A_1 Z_1^{N-1} + \alpha_0 A_2 Z_2^{N-1} + \dots + \alpha_0 A_N Z_N^{N-1} \\ \alpha_1 I_N &= \alpha_1 A_1 Z_1^N + \alpha_1 A_2 Z_2^N + \dots + \alpha_1 A_N Z_N^N \\ \alpha_2 I_{N+1} &= \alpha_2 A_1 Z_1^{N+1} + \alpha_2 A_2 Z_2^{N+1} + \dots + \alpha_2 A_N Z_N^{N+1} \\ &\vdots \\ \alpha_N I_{2N-1} &= \alpha_N A_1 Z_1^{2N-1} + \alpha_N A_2 Z_2^{2N-1} + \dots + \alpha_N A_N Z_N^{2N-1}\end{aligned}$$


---

$$\sum_{p=0}^N \alpha_p I_{p+(N-1)} = 0$$

These N different equations may be combined as

$$\sum_{p=0}^N \alpha_p I_{p+k} = 0, \quad \text{for } k = 0, 1, \dots, (N-1)$$

If we let  $\alpha_N = 1$ , then

$$\sum_{p=0}^{N-1} \alpha_p I_{p+k} = -I_{N+k}, \quad \text{for } k = 0, 1, \dots, (N-1)$$

The above equation represents N equations and N unknowns, the  $\alpha$ 's. These equations are written in matrix form as

$$\begin{bmatrix} I_0 & I_1 & I_2 & \dots & I_{N-1} \\ I_1 & I_2 & I_3 & \dots & I_N \\ I_2 & I_3 & I_4 & \dots & I_{N+1} \\ \cdot & & & & \\ \cdot & & & & \\ \cdot & & & & \\ I_{N-1} & I_N & I_{N+1} & \dots & I_{2N-2} \end{bmatrix} \begin{bmatrix} \alpha_0 \\ \alpha_1 \\ \alpha_2 \\ \cdot \\ \cdot \\ \cdot \\ \alpha_{N-1} \end{bmatrix} = \begin{bmatrix} -I_N \\ -I_{N+1} \\ -I_{N+2} \\ \cdot \\ \cdot \\ \cdot \\ -I_{2N-1} \end{bmatrix} \quad (3.6)$$

For the case considered here where the number of points in the waveform is equal to twice the number of degrees of freedom, Eqs. (3.6) may be solved directly for the  $\alpha$ 's. Then, the roots of the  $N^{\text{th}}$  order polynomial in Eq. (3.3) yield the poles using Eq. (3.4). Using the poles and substituting into the first N equations of Eq. (3.5), the residues can be found. If the number of waveform points is greater than twice the number of degrees of



freedom, Eq. (3.6) will have more equations than unknowns and the method of least squares may be used to solve them approximately.

In several ways the Prony analysis is an extremely useful numerical tool. If, for example, a given waveform is known to contain 10 poles, only 20 points of the waveform are required in order to determine its poles and residues. The waveform can then be extrapolated forward in time using Eq. (3.1). Also, the data has been compressed so that a waveform with hundreds of sample points can be saved by storing only a small number of poles and residues.

Prony analysis does suffer from some disadvantages. Aliasing can occur in the same manner as with the DFT if the sampling rate is not at least twice the frequency of the highest pole. It is also difficult to know how many degrees of freedom to assume for the data, sometimes called the Prony order. If the order is assumed too small, the resulting poles will be incorrect. If the order is too large, the correct poles will be given along with some number of other poles which depends on how high the assumed order is. The presence of these extra poles will not greatly affect the desired poles. Our procedure for determining the correct order is to begin with a small order and increase it until consistent results are obtained when the order is changed.

The frequency resolution of the Prony analysis is similar to that described earlier for the FFT. The resolution depends on the total observation time which is analyzed. Therefore, the maximum amount of data should be used while still keeping a short enough sampling interval to prevent aliasing [9].

Once the poles are calculated, they are examined for any which have positive real parts. These are obviously not physical and are removed before any residues are calculated. Generally, these result from assuming too large an order and their residues are several orders of magnitude below the desired pole residues. In order to determine which of the remaining poles represent physical natural frequencies of the object, a technique called sliding window Prony [9-11] is used. The unwanted poles, called curve fitting poles, are put in by the algorithm just to fit the curve and are due primarily to noise. The sliding window technique involves doing several successive Prony analyses on a single waveform. After each, the window of  $2N$  points required by the analysis is moved by one sample point. This is normally done 3 to 10 times and the poles are plotted in the complex plane. The poles which represent physical natural frequencies will tend to cluster and the curve fitting poles will scatter and move around in the complex plane as the window is shifted. The natural frequency is taken to be the average value of the poles in the cluster.

If the input waveform from the pulse generator contains any poles, these will show up in the Prony analysis of the field measurement waveform. To avoid this, the transfer function is used to apply a mathematical input, containing known pole locations, to the system. The resulting output waveform is free of unknown pole contributions from the input. A square pulse input is used in this work, which has poles only at zero and minus infinity.

The transfer function could be obtained from the poles and residues by using the following expression:

$$H(j\omega) = \sum_{m=1}^N \frac{A_m}{-\sigma_m + j(\omega - \omega_m)} + C$$

where the poles  $s_m$  have been written in terms of their real and imaginary parts as

$$s_m = \sigma_m + j \omega_m$$

The constant  $C$  gives rise to a delta function at  $t = 0$ .

### Prony Analysis Code

The Prony analysis code written in Fortran is given in Appendix II. A flow chart of the code is shown in Figure 3.1. Available Fortran subroutines are used to solve sets of linear equations and to find the zeros of a polynomial [24]. Due to computer limitations, a maximum order of 36 can be handled, which corresponds to 36 poles and residues. After the poles and residues have been computed from each

ORIGINAL PAGE IS  
OF POOR QUALITY

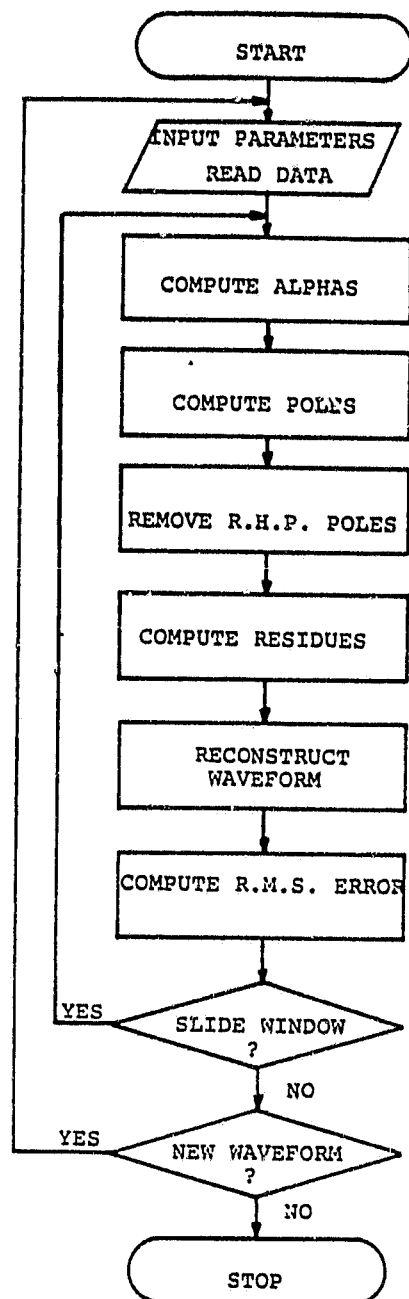


Figure 3.1. Flow chart of Prony code.

window, the waveform is reconstructed using Eq. (3.1). The RMS error between the original and reconstructed waveforms is calculated to give an indication of how well the curve has been fitted. Errors of up to 10% are considered acceptable, but 1 to 2% is typical. Detailed operator instructions for running the code are given elsewhere [20].

### Stick Modeling

In an attempt to predict the natural resonances of the F-106B for comparison with the Prony results, a stick-model technique is used [25]. The fuselage, wings, and tail of the aircraft are modeled using thin, perfectly conducting sticks. This works fairly well for normal aircraft, but the delta-wing does not lend itself to modeling by a single stick. Nevertheless, useful results may be obtained from the method. The model is in free space, with an electromagnetic wave polarized along the fuselage incident upon it. To first order, the current on each stick can be written as a directly induced component plus a sine and cosine component. An expression is written for each stick in the following form:

$$I_n(\xi) = I_{ind,n}(k, \xi, \theta) + S_n \sin[k(\xi - l_n)] + C_n \cos[k(\xi - l_n)]$$

The  $S_n$  and the  $C_n$  must be chosen to satisfy the boundary conditions at the junctions and at the ends. At the ends, the current must vanish. At the junctions, the current must be conserved and the charge density must be continuous. After applying these conditions, a matrix set of equations is obtained for the  $S_n$  and  $C_n$ . The natural frequencies are found

by setting the incident field  $E_0 = 0$  and examining these equations for nontrivial solutions. The result is a transcendental equation whose zeros give the frequencies of the natural resonances. For a more detailed explanation, the reader is referred to reference [25]. Results from this method will be given in a later chapter.

## CHAPTER IV

### CIRCULAR CYLINDERS

Prior to applying the techniques described in the previous two chapters to the F-106B model, it was desired to test them to see if they give reasonable results on simpler objects. The natural frequencies for isolated thin cylinders have been calculated by Tesche [26]. If a simple circular cylinder with end caps were connected in place of the aircraft model, the results could be compared with those of Tesche for isolated cylinders. In this way, if natural frequencies related in a reasonable way to Tesche's were found, the experimental procedure would be verified and at the same time valuable information obtained on the effect of wire attachments on natural frequencies.

The experiments consisted of making B-dot and D-dot measurements on two different cylinders, one 2 inches and the other 6 inches in diameter. Each cylinder is 3 feet long. The sensors were placed exactly in the center (lengthwise) of the cylinders. The reason for this placement is described as follows: The situation is similar to that where the cylinder is isolated and a plane electromagnetic wave is incident upon it polarized with the electric field in the longitudinal direction. The modes with current flow in the longitudinal direction will be excited. These modes must have current minima or nodes and voltage maxima or antinodes at each end. These modes are shown in Figure 4.1. From this figure, it is seen that the B-dot sensor is located

ORIGINAL FORM OF  
OF POOR QUALITY

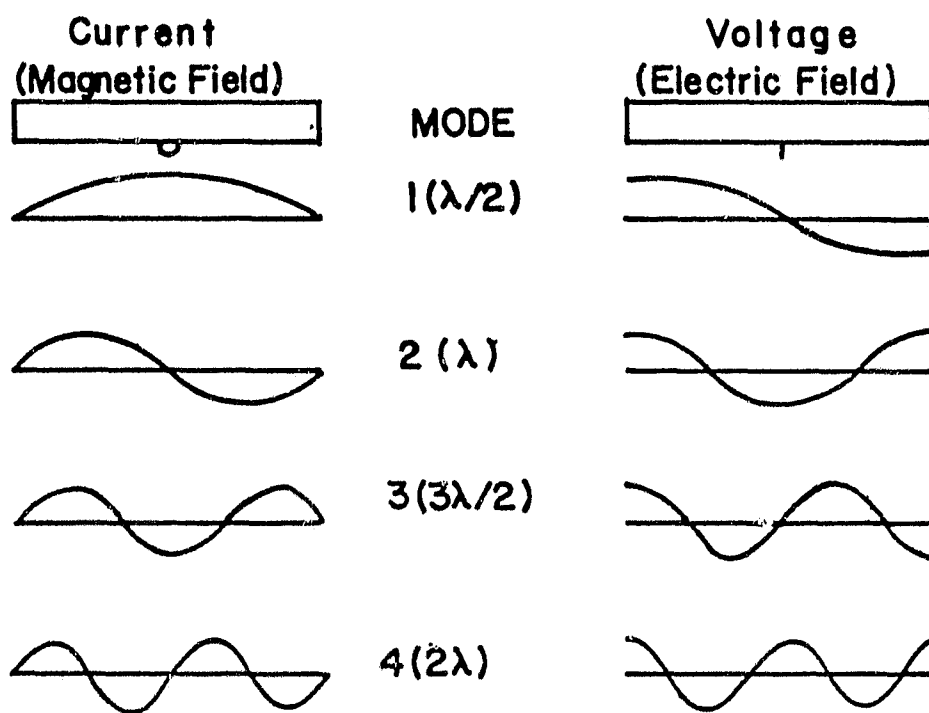


Figure 4.1. First four cylinder modes.



exactly on a current node for the even modes. Similarly, the D-dot sensor is located on a voltage node for the odd modes. Consequently, the B-dot sensor will detect only the odd modes and the D-dot will detect only the even modes. Each waveform will therefore contain only half of the natural frequencies and thus be simpler to Prony analyze.

The measured B-dot and D-dot waveforms for the thin (2 in) and the thick (6 in) cylinders, with wires, are given in Figures 4.2 and 4.3, respectively. The input waveform from the pulse generator is shown in Figure 4.4. The measured waveforms were integrated to obtain the fields and the input waveform deconvolved from them to produce the transfer function magnitudes shown in Figures 4.5 and 4.6. The corresponding phases for each are shown in Figures 4.7 and 4.8. The peaks in the magnitude spectra indicate the resonant frequencies of the cylinders. The values of the first 4 resonant frequencies for each cylinder are listed in Table 4.1. Due to the bandwidth limitation of the B-dot sensor, only the first 4 can be reliably examined. Note the missing modes in the spectra for each sensor as described earlier. The lowest resonance at 156 MHz corresponds to the half-wavelength resonance of the cylinder. The cylinder is 3 feet (0.91 m) long, so the frequency having twice this as its wavelength is

$$f = \frac{c}{\lambda} = \frac{3 \cdot 10^8}{2 \cdot 0.91} = 164 \text{ MHz}$$

ORIGINAL PAGE IS  
OF POOR QUALITY

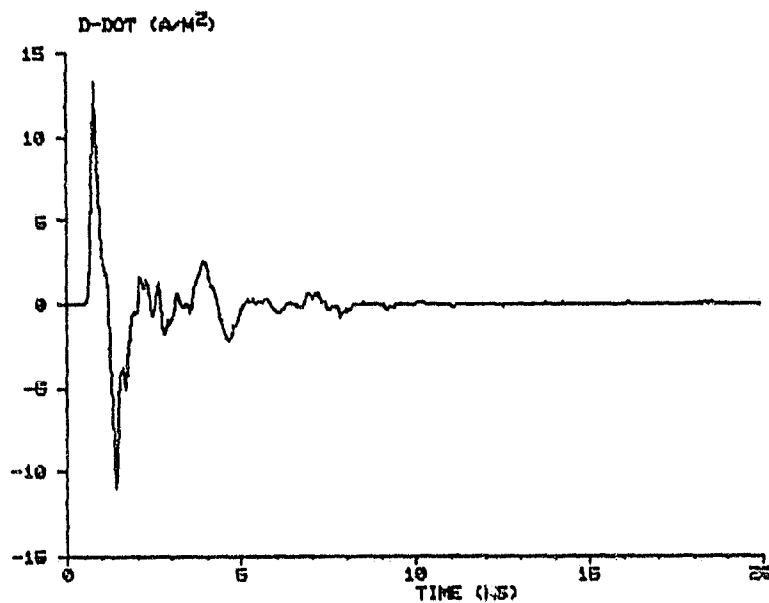


Figure 4.2. Measured waveforms from the thin cylinder.

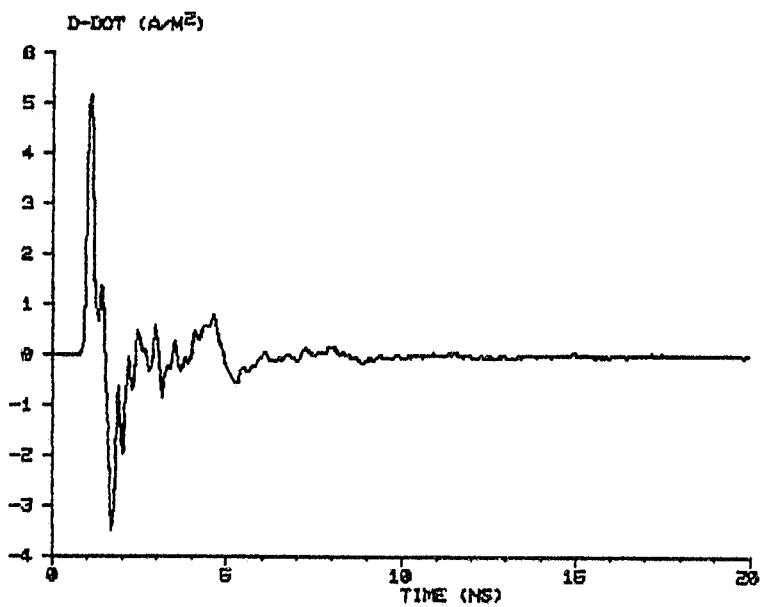
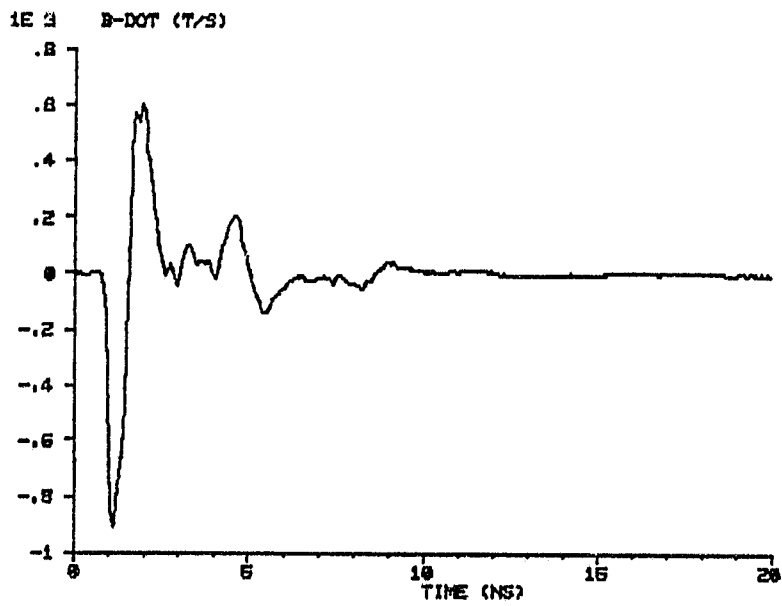


Figure 4.3. Measured waveforms from the thick cylinder.

ORIGINAL PAGE IS  
OF POOR QUALITY

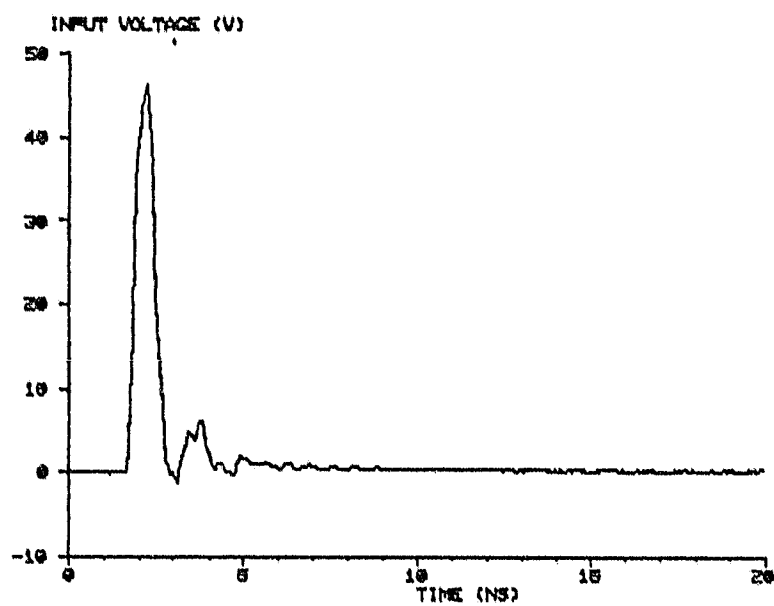


Figure 4.4. Pulse generator output waveform.

ORIGINAL PAGE IS  
OF POOR QUALITY

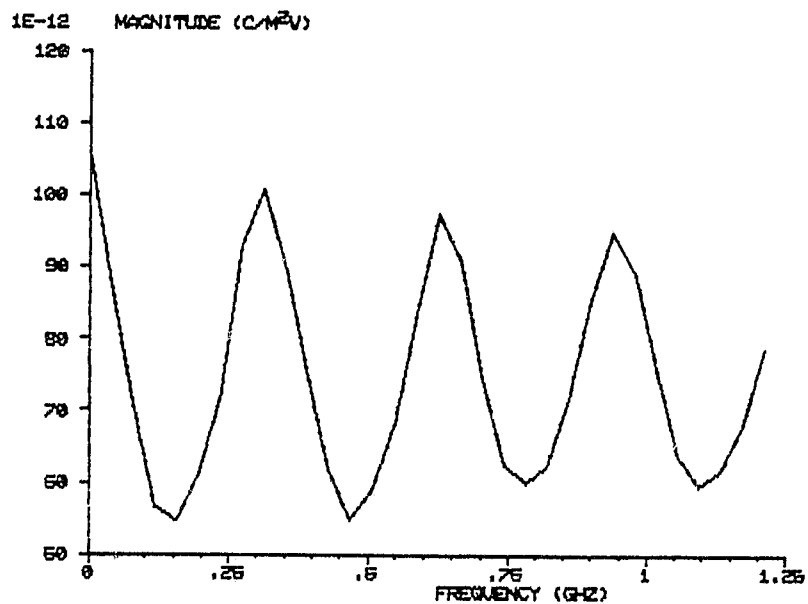
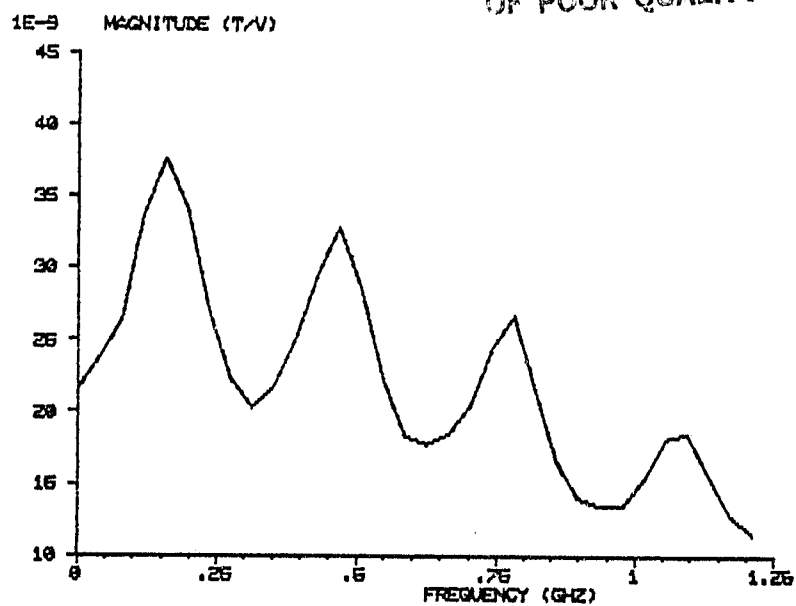


Figure 4.5. Transfer function magnitudes for the thin cylinder.

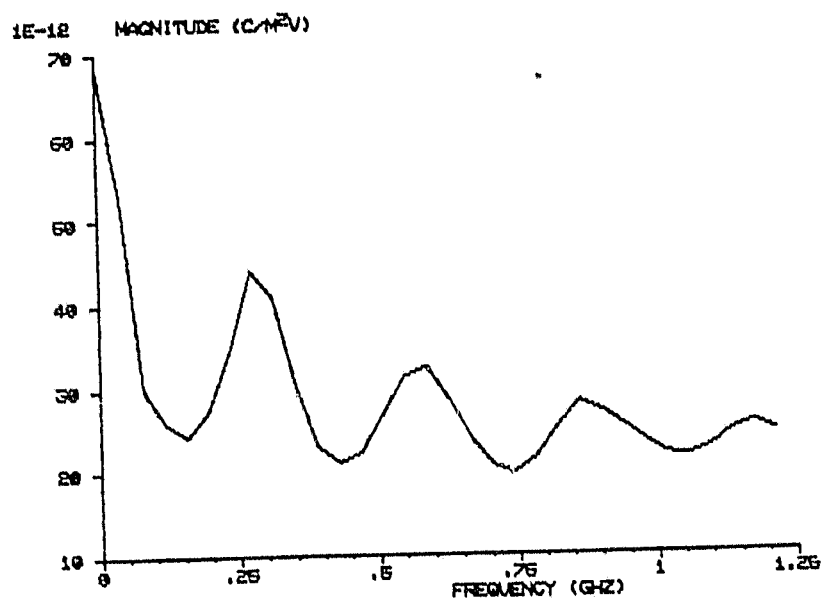
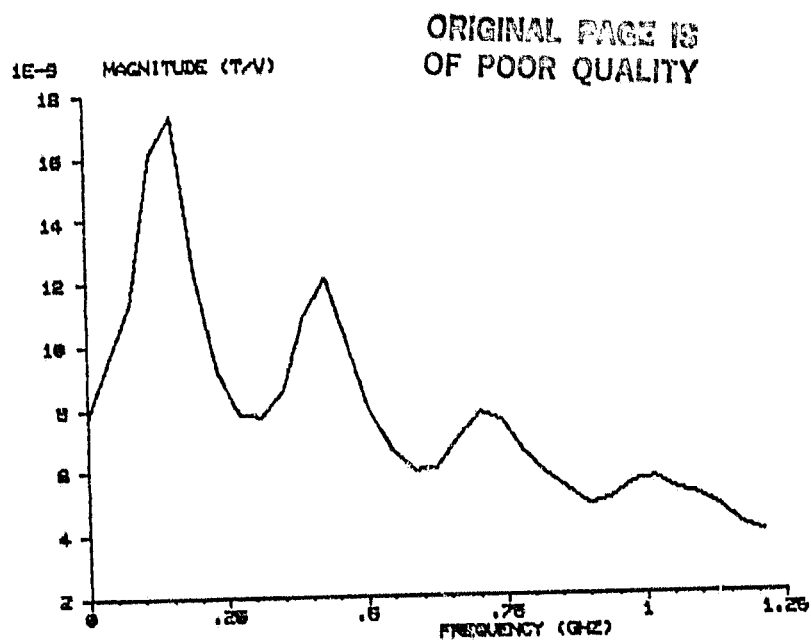
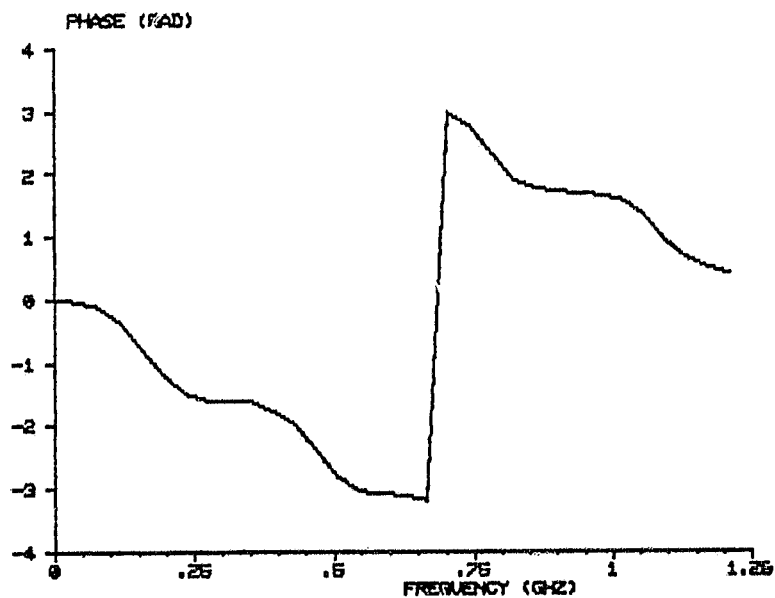
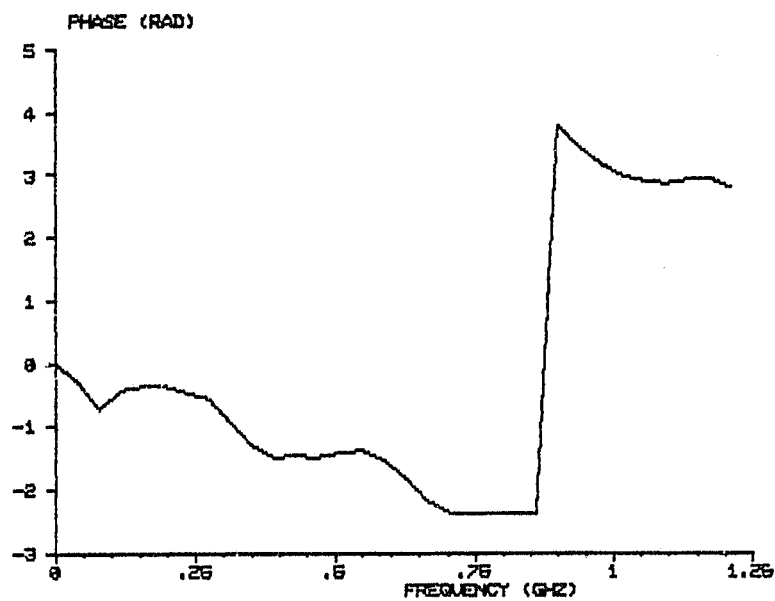


Figure 4.6. Transfer function magnitudes for the thick cylinder.

ORIGINAL PAGE IS  
OF POOR QUALITY



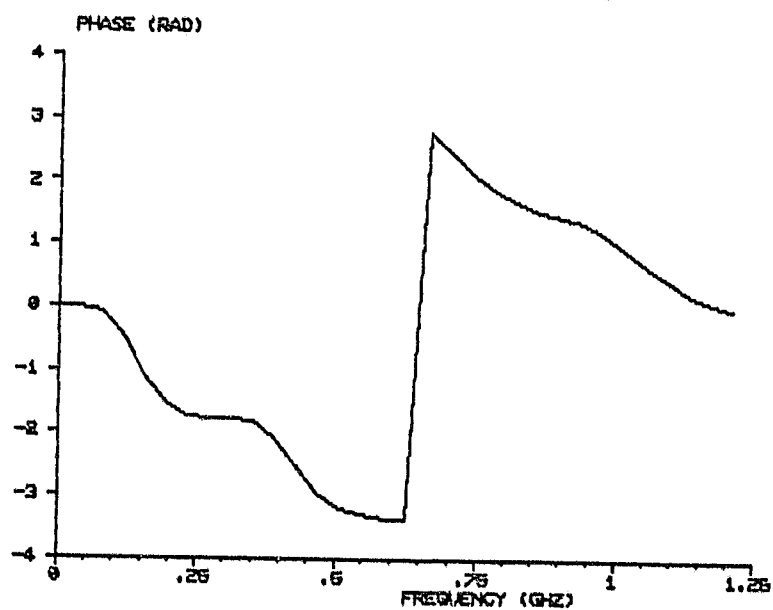
B



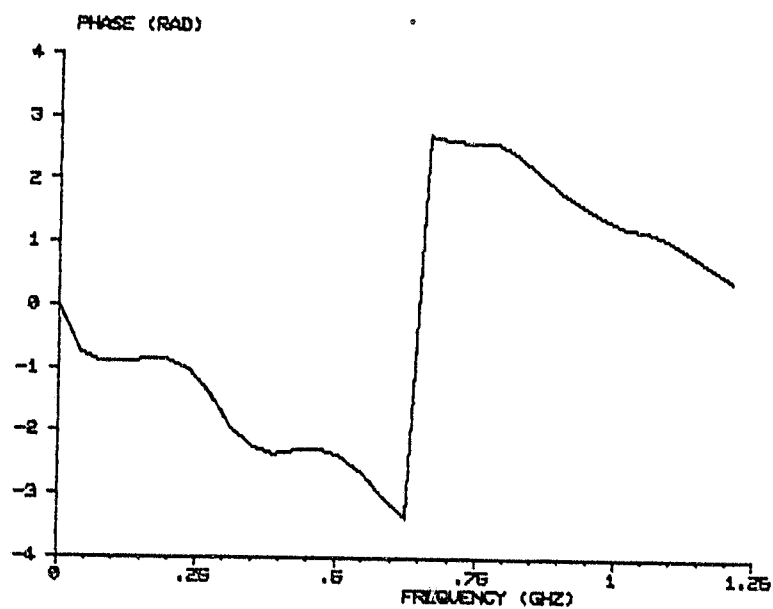
D

Figure 4.7. Transfer function phases for the thin cylinder.

ORIGINAL PAGE IS  
OF POOR QUALITY



B



D

Figure 4.8. Transfer function phases for the thick cylinder.



TABLE 4.1. RESONANCES OF CIRCULAR CYLINDERS

THIN CYLINDER

MODES PRESENT	f, MHZ	MODES PRESENT	f, MHZ
B		D	
1	156	-	-
-	-	2	313
3	469	-	-
-	-	4	625

THICK CYLINDER

MODES PRESENT	f, MHZ	MODES PRESENT	f, MHZ
B		D	
1	156	-	-
-	-	2	273
3	430	-	-
-	-	4	586

The frequency resolution for the spectra is 39 MHz, so quantization error is large enough to account for errors in spectral estimation. Note that for the thin cylinder, all higher order resonances are harmonics of the lowest resonance. This is not true for the thick cylinder. If the thin cylinder were infinitely thin, it would have harmonically related resonances at  $\lambda/2$ ,  $\lambda$ ,  $3\lambda/2$ , etc. The thick cylinder has more end capacitance than does the thin one which makes it look electrically longer and lowers the resonant frequencies. The Prony analysis will later show that the first resonant frequency of the two cylinders is not the same and that the thin cylinder also has its resonant frequencies affected by its finite thickness.

Using the transfer functions, the square pulse was applied to produce output waveforms for use in the Prony analysis. These are shown in Figures 4.9 and 4.10 for the thin and thick cylinders, respectively. The waveforms from the thin cylinder show very sharp reflections from the ends as compared to those from the thick cylinder. The large ends cause greater dispersion of the waveform on the thick cylinder. The reflections die out within 15 ns, indicating that by then, all energy is removed from the cylinder through radiation and by flowing onto the wires. Note that in the D waveform for the thick cylinder, the effect of the end

ORIGINAL PAGE IS  
OF POOR QUALITY

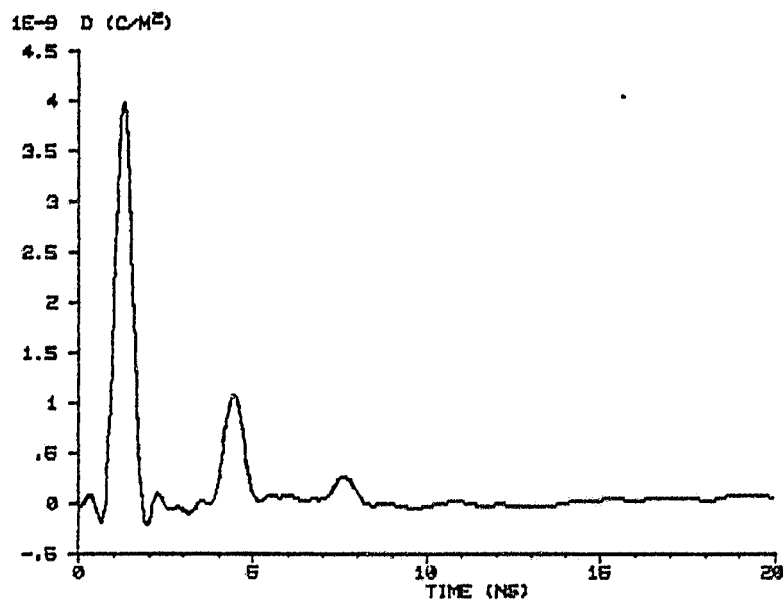
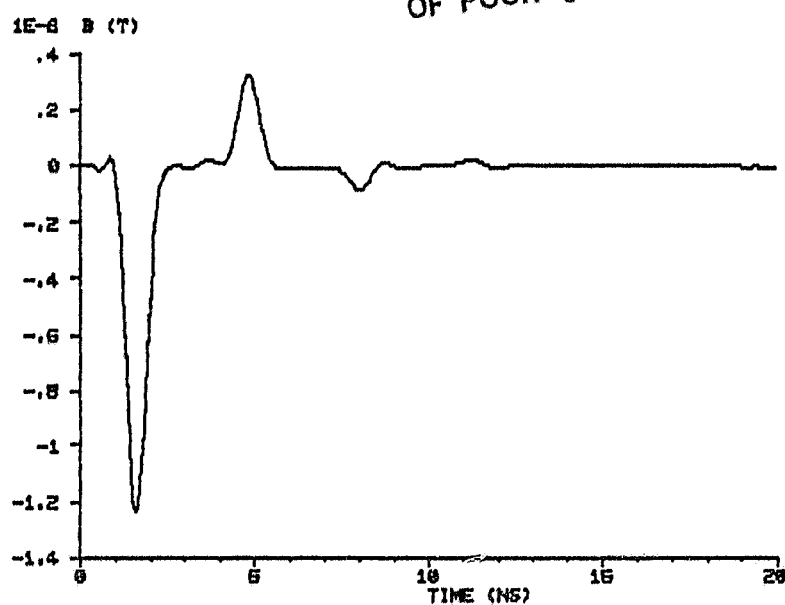


Figure 4.9. Field waveforms for the thin cylinder.

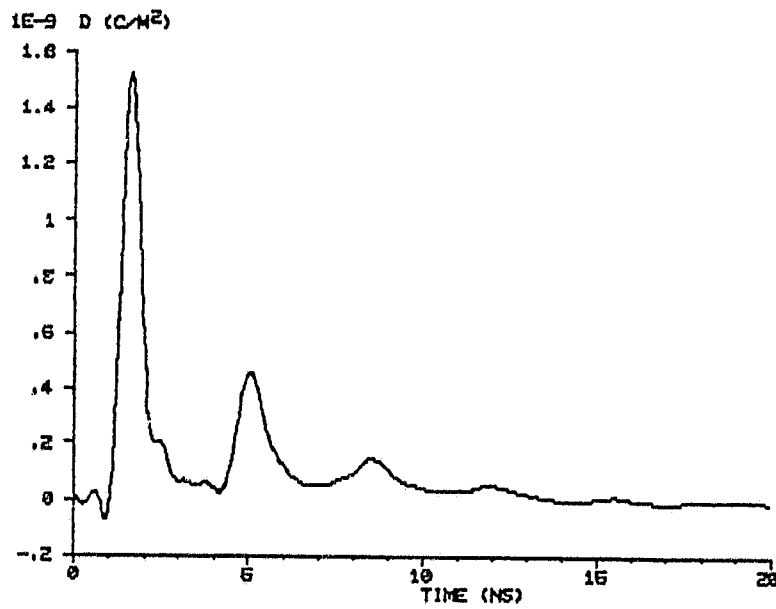
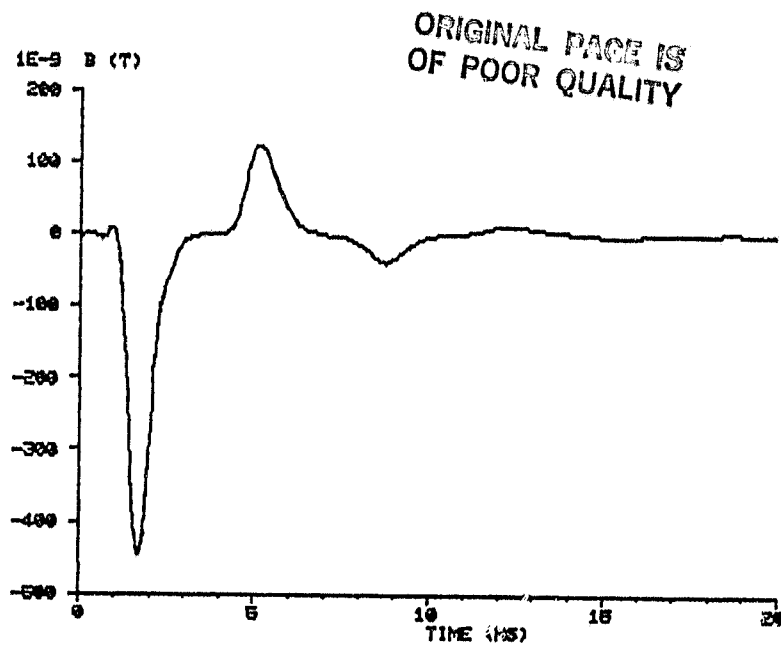


Figure 4.10. Field waveforms for the thick cylinder.

capacitance can be readily seen as an exponential discharge toward zero. The cylinder and wires are like a parallel RC circuit with an impulse function input. The capacitor is charged instantaneously by the impulse and then discharges afterward.

Prony analysis was next applied to the waveforms in Figures 4.9 and 4.10. Ten windows were used on each waveform in the sliding window method. Initially, an order of 10 was assumed and then the order was increased until consistent results were obtained. This occurred at an order of 20 and above. The results shown were obtained using an order of 20. Every 4th point was taken yielding a sampling interval of 200 ps and a folding frequency of 2.5 GHz, well above the highest frequency content of the waveforms. This gave an observation time of 8 ns which was enough to provide adequate frequency resolution.

The results from the Prony analysis are shown in Figure 4.11. Four different sets of natural frequencies are plotted in the complex frequency plane, with the first 4 shown for each set. The natural frequencies are also listed in Table 4.2. The vertical axis is the imaginary part of the natural frequency indicating the frequency of the resonance. The horizontal axis is the real part corresponding to the damping rate of the resonance. Only the upper left quadrant is shown, but each natural frequency

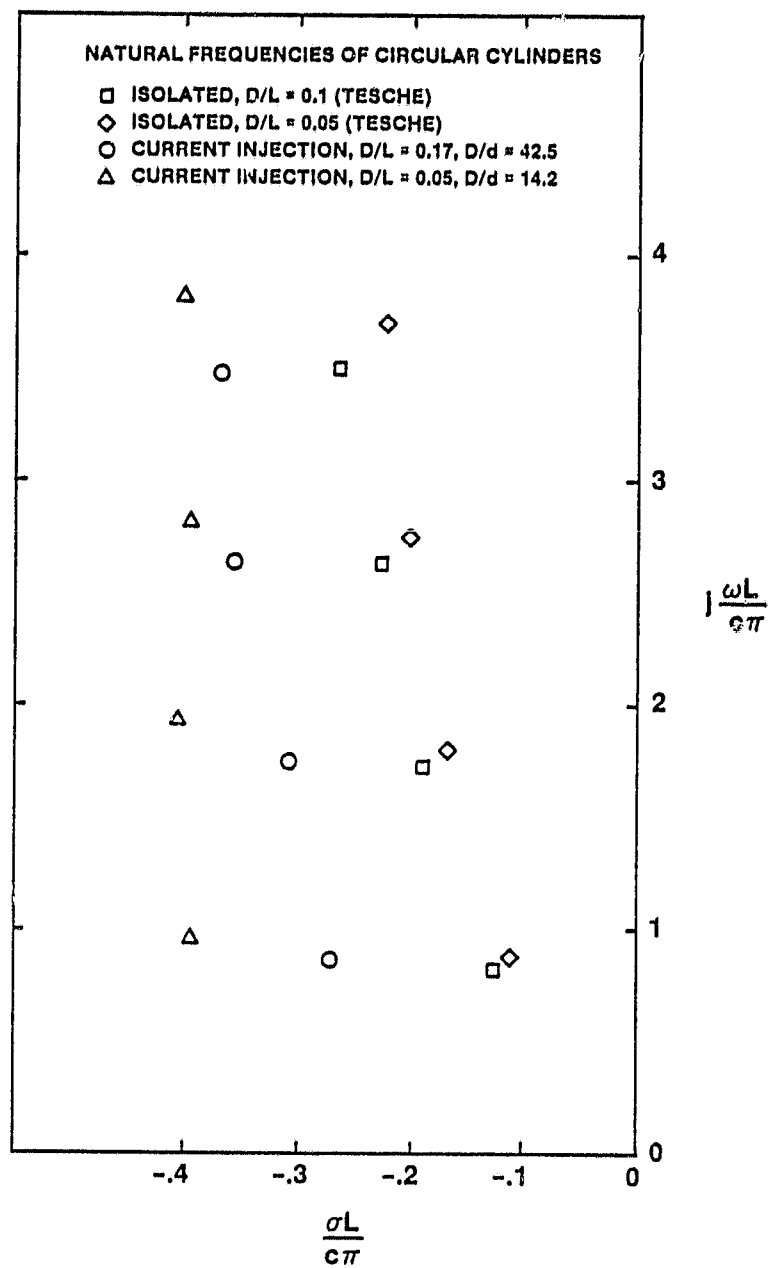


Figure 4.11. Prony analysis results from the circular cylinders.

TABLE 4.2. NATURAL FREQUENCIES OF CIRCULAR CYLINDERS

Isolated		Wire Attachment	
Thin	Thick	Thin	Thick
$-0.114 + j0.869$	$-0.125 + j0.822$	$-0.394 + j0.980$	$-0.273 + j0.869$
$-0.168 + j1.806$	$-0.190 + j1.772$	$-0.407 + j1.960$	$-0.310 + j1.750$
$-0.205 + j2.742$	$-0.228 + j2.635$	$-0.395 + j2.840$	$-0.359 + j2.643$
$-0.225 + j3.700$	$-0.265 + j3.500$	$-0.403 + j3.840$	$-0.370 + j3.473$

ORIGINAL PAGE IS  
OF POOR QUALITY

has its corresponding complex conjugate in the lower left quadrant. The natural frequencies are scaled by the factor  $L/c\pi$  as described earlier.

The two sets of natural frequencies closest to the imaginary axis are for isolated cylinders of different thicknesses as computed by Tesche. The leftmost sets are those computed here for the cylinders with wires attached. The information on the cylinder thickness and wire size is given on Figure 4.11. Tesche did not compute the natural frequencies for a cylinder as thick as the 6 inch one used here, so those plotted are for the thickest that he did consider.

The natural frequencies for isolated cylinders lie in nearly a vertical line, with damping increasing slightly with frequency. The natural frequencies of an infinitely thin cylinder would lie on the imaginary axis at 1.0, 2.0, etc. Therefore, the thin cylinder is closer to the imaginary axis and more nearly vertical. As the cylinder is made thicker, the resonant frequencies decrease due to the capacitance of the ends which make it look electrically longer. The damping also increases since the thick cylinder radiates more readily than does the thin one. The natural frequencies thus move down and to the left with increasing cylinder thickness.

In the isolated case, only radiation and small ohmic losses remove energy from the cylinder. The addition of wires adds another energy loss mechanism since current can



flow off the cylinder onto the wires. On the thin cylinder with wires, the cylinder to wire ratio is less than for the thick cylinder and thus the impedance change at the junction is smaller. Consequently, the wires will carry off proportionately more current from the thin cylinder than from the thick one. This is reflected in the real parts of the natural frequencies, which indicate considerably more damping for the thin cylinder than for the thick one. The resonant frequencies of the thin cylinder are almost harmonically related and increased above those of the same size isolated cylinder. This is caused by the wires which change the geometry of the ends, reducing their capacitance and making the cylinder electrically shorter than when isolated. The same would be true for the thick cylinder, but is not apparent from Figure 4.11 since Tesche did not compute results for a cylinder as thick as this. If he had, they would lie slightly below and to the left of those shown.

If the cylinder thickness were reduced until, in the limit, it became the same size as the wires, the resonances would vanish. This corresponds to the real part of the natural frequencies moving to minus infinity. The imaginary parts would at the same time be asymptotically approaching 1.0, 2.0, etc. On the other hand, increasing the cylinder to wire ratio approaches the isolated case since the wire will have less and less current transferred to it.

It is interesting to compare the motion of the natural frequencies as the cylinder is made thicker for the isolated and wire-attached cases. In the isolated case, they move down and to the left indicating a lower resonant frequency and greater damping due to more radiation. However, in the case with the wires attached, they move down and to the right indicating a lower resonant frequency but less damping. Therefore, the effect of the wires in allowing less energy to flow off for a larger cylinder to wire ratio is overcoming the greater radiation of the thicker cylinder.

These results indicate that our entire method (measurement plus Prony analysis) is working well. The natural frequencies computed for the cylinders with wires differ from those for isolated cylinders in a logical manner. The wires increase the damping of each resonance by a factor of from 1.25 to 4 since they remove energy from the cylinders. They also increase the frequencies of the resonances slightly since they make the cylinders electrically shorter.

## CHAPTER V

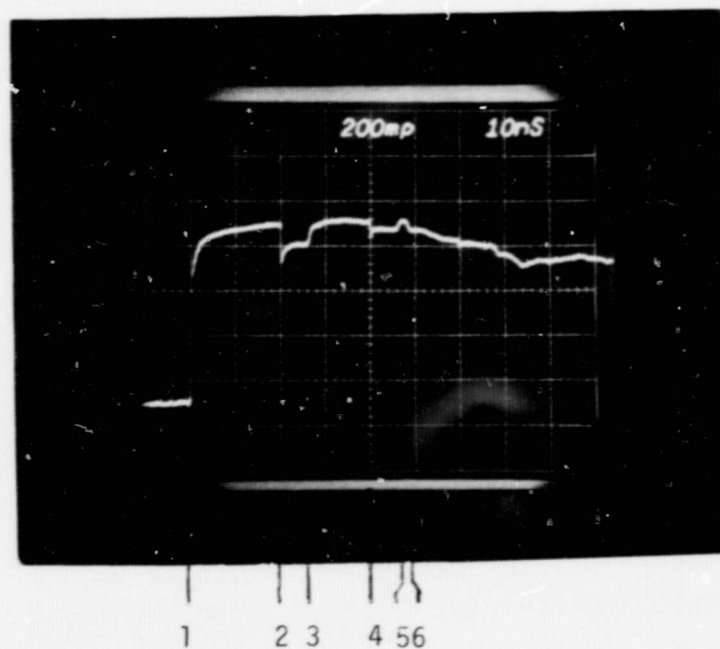
### F-106B SCALE MODEL

#### Time Domain Reflectometry

TDR was used to study the model in two stages. First, the model was tested without its wings and tail leaving only the cylindrical fuselage. This was followed by a test with the model intact. The tests were conducted using the same experimental apparatus which was shown in Figure 2.1, but with the TDR connected to the pulse generator cable. These tests help in understanding the effects of the wings and tail on the reflections which occur on the model.

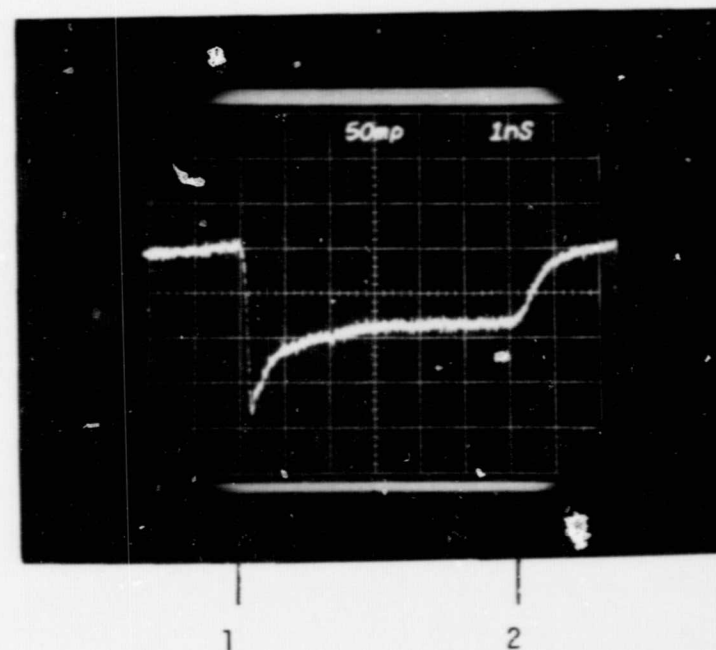
The TDR oscillograms for the fuselage alone are shown in Figure 5.1. The reflections from the various portions of the fuselage are labeled in each of the TDR traces. The initial rise of the trace shows a reflection coefficient of 0.72, corresponding to an impedance of 307 ohms at the bottom of the lower wire. The gradual upward slope of the initial 10 feet of wire indicates a continuously increasing impedance (higher  $\rho$ ) as the wave travels away from the ground plane. The cylinder, being a thicker conductor, represents a lower impedance than the wire as shown by the decrease in  $\rho$  at the cylinder bottom. The capacitance of the end cap is seen as an initially lower impedance then a quick exponential charge up.

The TDR oscillograms for the entire F-106B model are shown in Figure 5.2. Noted on both oscillograms are the



a) Overall trace

1. Ground plane
2. Cylinder bottom
3. Cylinder top
4. Cylinder bottom - 2nd pass
5. Cylinder top - 2nd pass
6. Overall top of apparatus

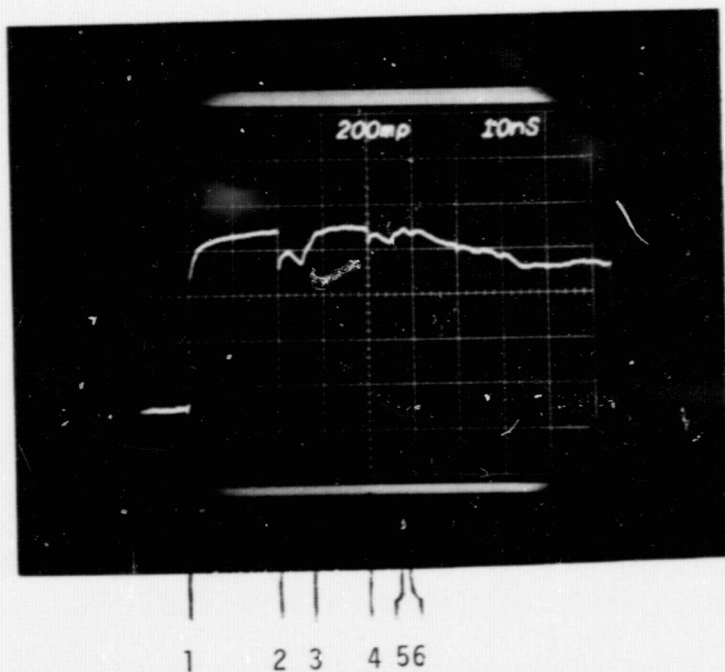


b) Fuselage detail

1. Cylinder bottom
2. Cylinder top

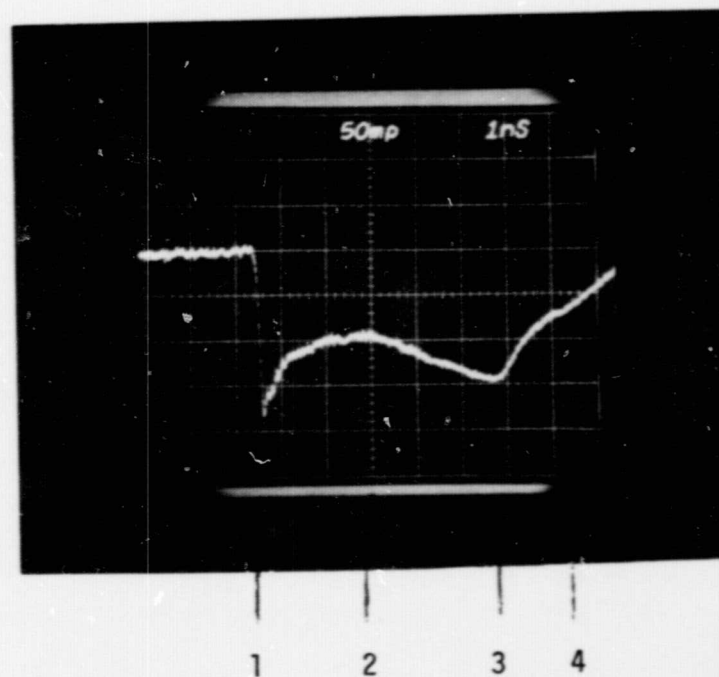
ORIGINAL PAGE IS  
OF POOR QUALITY

Figure V-1. TDR oscillograms from fuselage only.



a) Overall trace

1. Ground plane
2. Model nose
3. Tail
4. Model nose - 2nd pass
5. Tail - 2nd pass
6. Overall top of apparatus



b) Model detail

1. Model nose
2. Start of wings
3. End of wings
4. Tail

ORIGINAL PAGE  
BLACK AND WHITE PHOTOGRAPH

Figure V-2. TDR oscillograms from F-106B model.

various portions of the model, including the added effects of the wings and tail. These traces are the same as those of the fuselage alone until the wings are encountered about 2.4 ns after the nose. The wings represent a decreasing impedance, causing the reflection coefficient to decrease with distance along the model. Also, the main reflection from the end of the model comes from the end of the wings rather than from the end of the fuselage. This is shown by the shorter time (5.5 ns) the wave takes to traverse the model, as compared with 6 ns for the fuselage alone. This assumes that the wave travels at the speed of light on the model. The tail can also be seen as a short flat portion of the reflection coefficient curve about 6.5 ns after the nose. The overall reflection from the end of the model is smeared due to the largeness of the end including the wings, tail, and fuselage.

The two most interesting results from the TDR experiments are first, that the end reflection from the aircraft comes more prominently from the end of the wings than from the end of the fuselage. Second, the effect of the wings is to introduce a decreasing impedance as the wave propagates from nose to tail. This, in turn, makes the current flowing on the skin a function of position on the aircraft. The current is greater toward the tail than toward the nose.

### Current Injection

Transient field measurements on the scale model included the use of four different attachment point configurations in order to produce a variety of possible excitation conditions. These configurations are shown in Figure 5.3. Configuration 1 is longitudinal excitation from nose to end of fuselage. Configuration 2 is similar except that the rear attachment point is on the port wing tip. Configuration 3 is transverse excitation with current entering one wing tip and exiting from the other. Configuration 4 is excitation in the remaining plane, with current entering the middle of the fuselage as in a swept stroke event and exiting from the top of the vertical stabilizer. The peak signal to RMS noise ratio for measurements on all configurations is greater than 30 dB, and usually is above 35 dB.

### Configurations 1 and 2

The measured B-dot and D-dot waveforms for configurations 1 and 2 are shown in Figures 5.4 and 5.5, respectively. As in Chapter IV, these waveforms are integrated to obtain the fields and the input waveform is deconvolved from them to obtain the transfer function magnitudes shown in Figures 5.6 and 5.7. The phases for the transfer functions of configuration 1 only are shown in Figure 5.8. The frequency axes of the transfer functions have been scaled to the size of the actual aircraft. This is all that is required for similitude between model and aircraft. The model is nearly perfectly conducting, and thus conductivity scaling is not necessary.

ORIGINAL PAGE IS  
OF POOR QUALITY

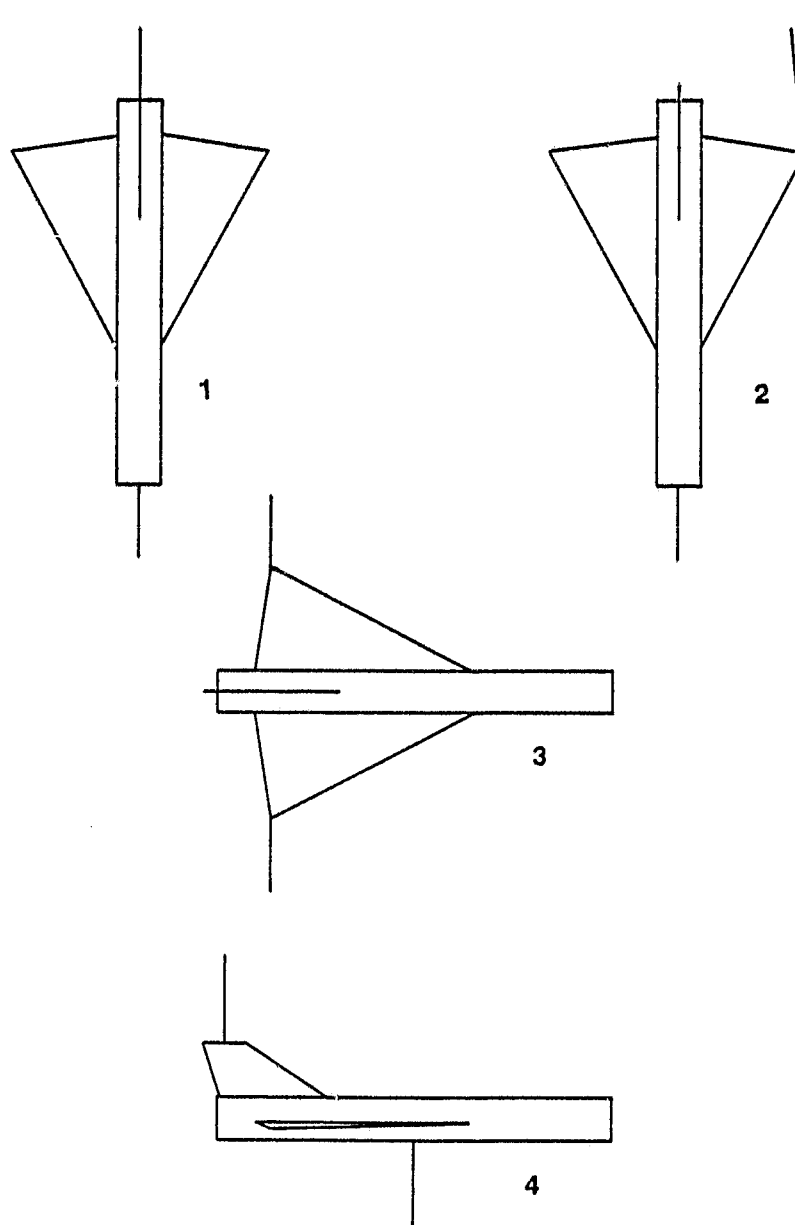


Figure 5.3. Attachment configurations for the F-106B model.



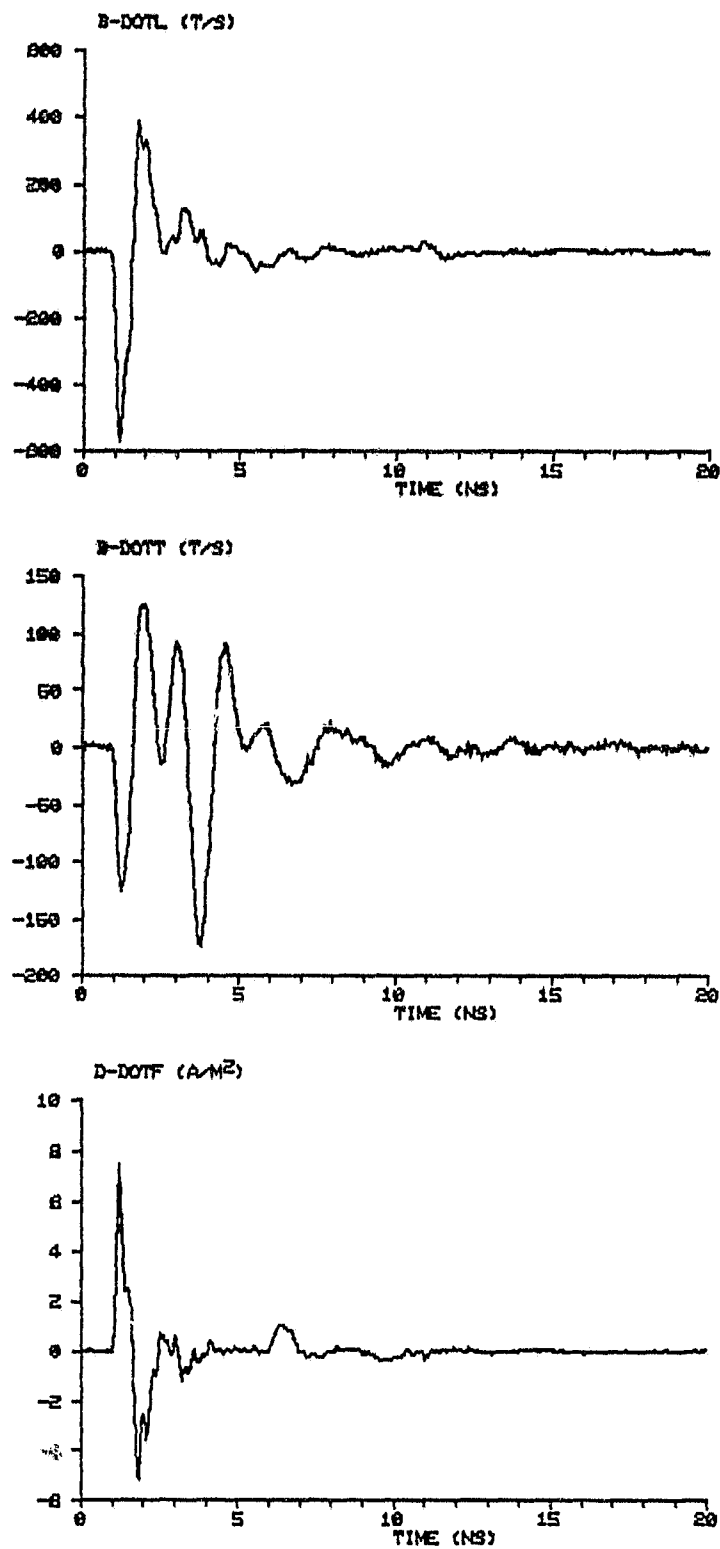


Figure 5.4. Measured waveforms from model configuration 1.

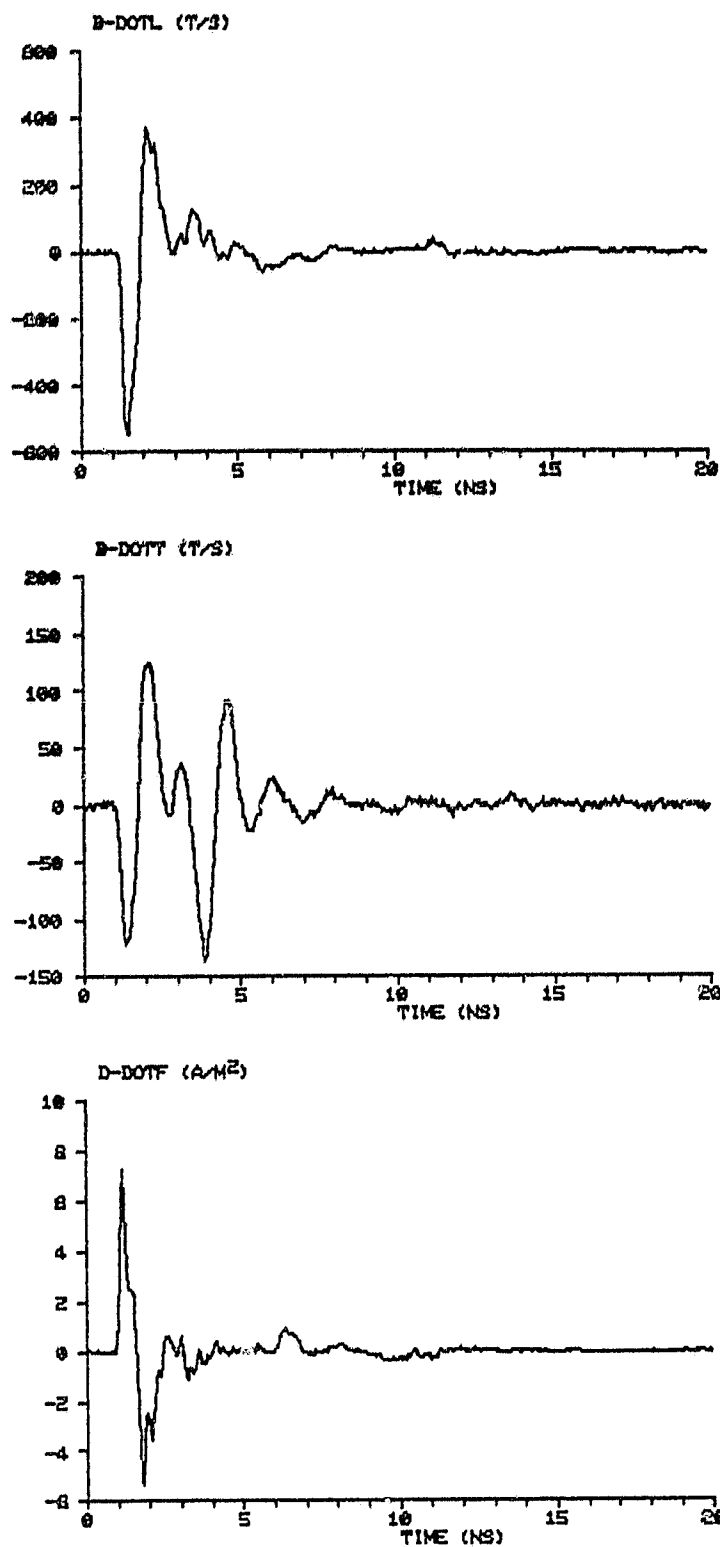
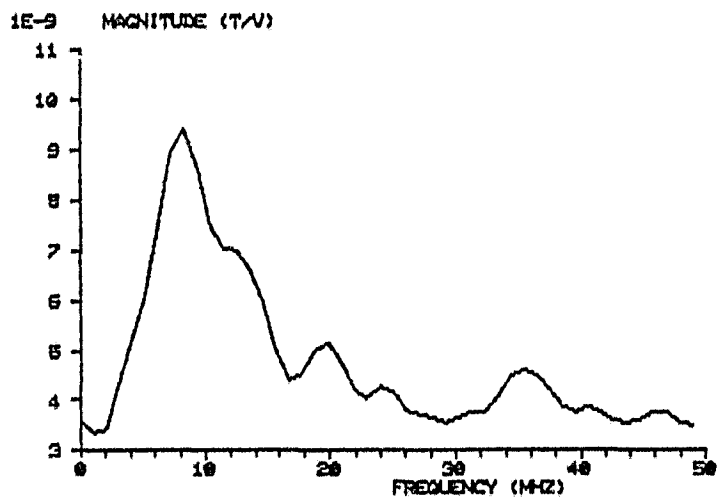
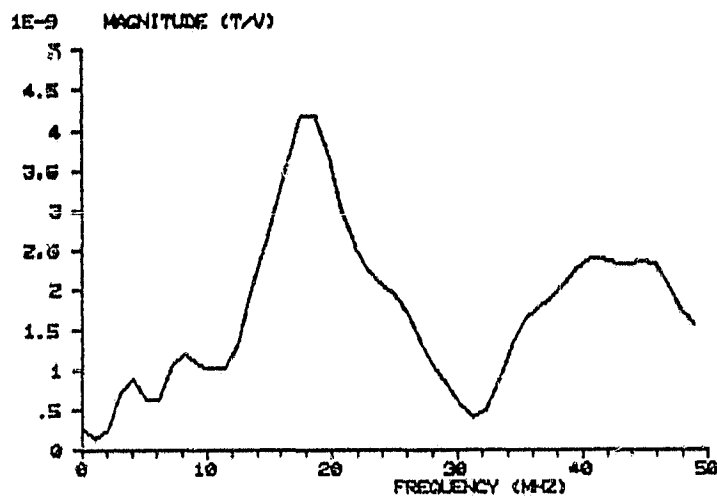


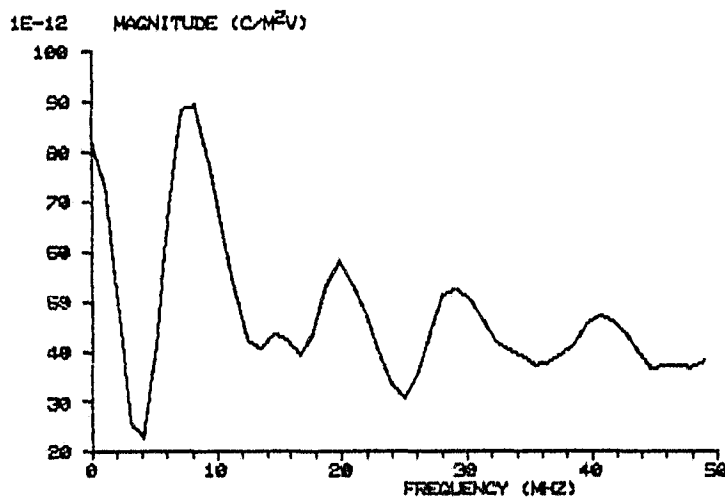
Figure 5.5. Measured waveforms from model configuration 2.



$B_L$



$B_T$



$D_F$

Figure 5.6. Transfer function magnitudes for model configuration 1.

ORIGINAL PAGE IS  
OF POOR QUALITY

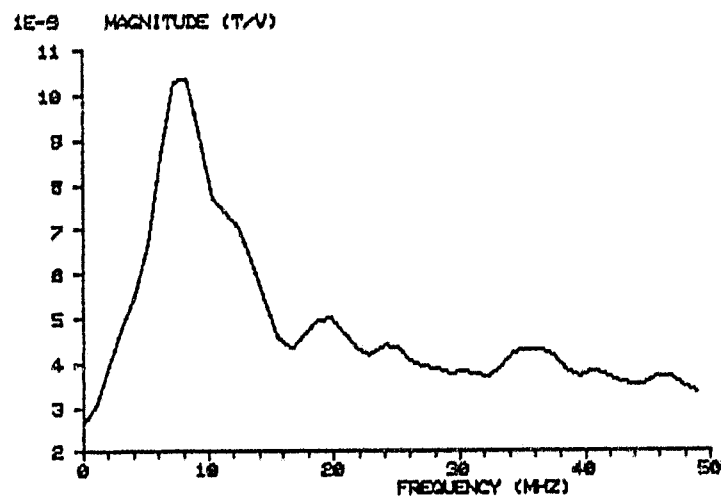
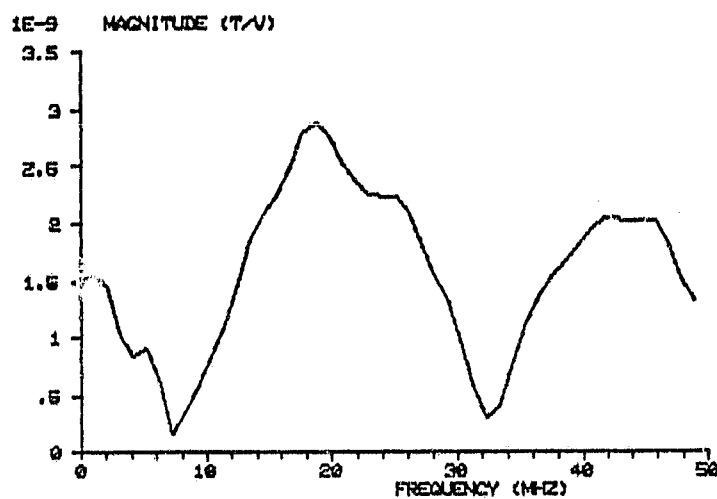
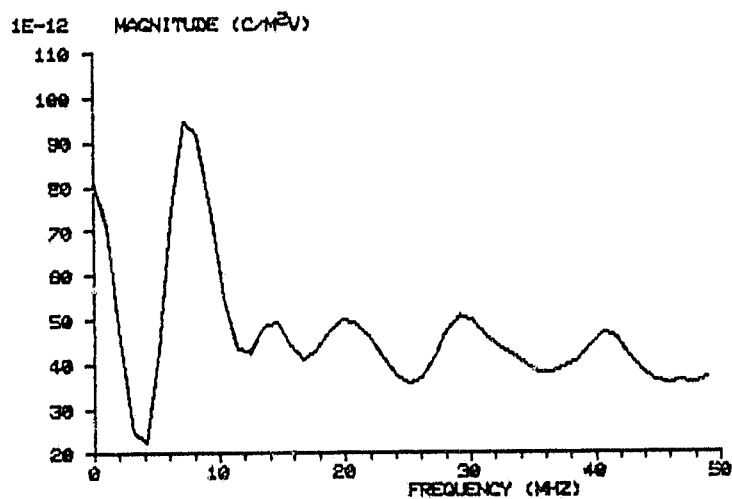
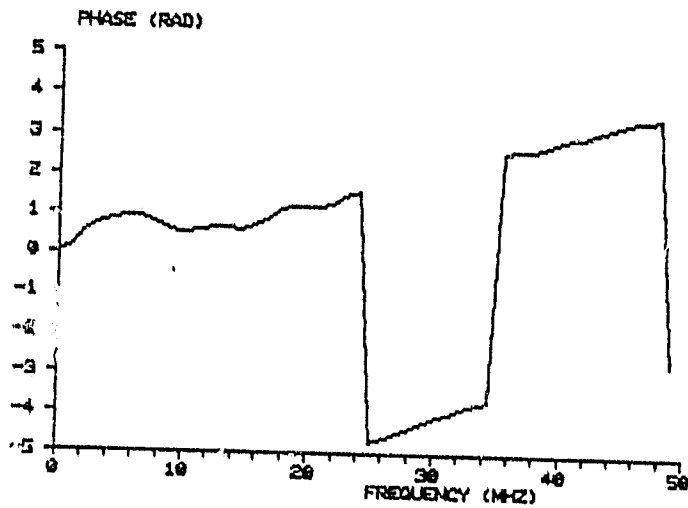
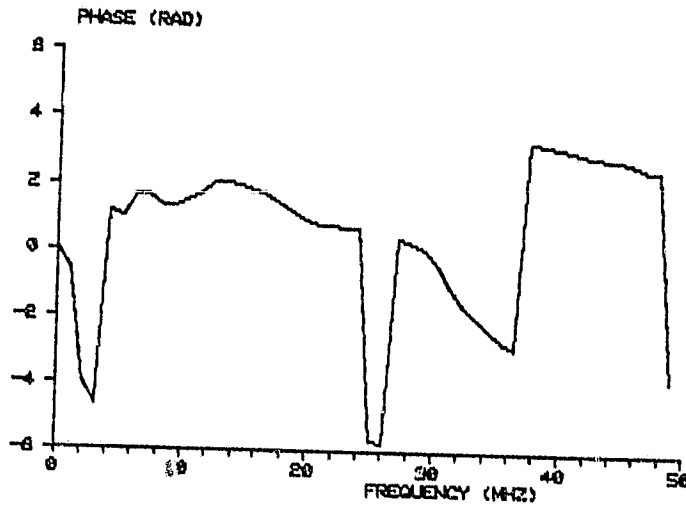
 $B_L$  $B_T$  $D_F$ 

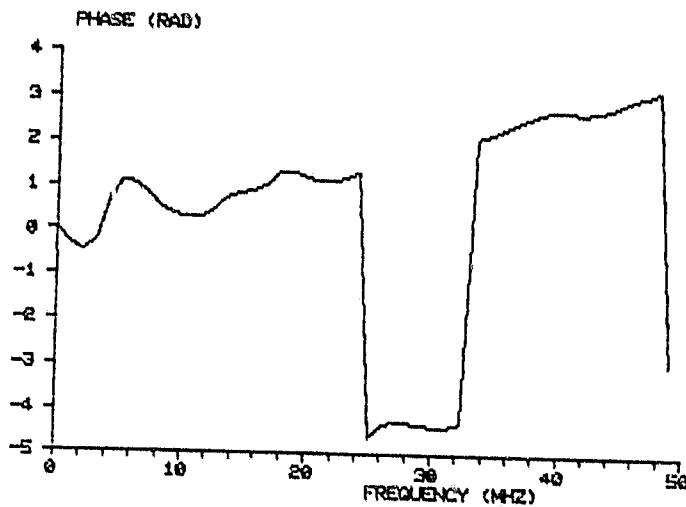
Figure 5.7. Transfer function magnitudes for model configuration 2.



$B_L$



$B_T$



$D_F$

Figure 5.8. Transfer function phases for model configuration 1.

The spectra from longitudinal B are very similar in configurations 1 and 2. Resonances are indicated at 7.5, 13, 19.5, 24, and 35 MHz, the dominant being 7.5 MHz. Spectra from transverse B are also similar, both being dominated by a resonance at 19 MHz. Resonances also appear at 24.5, 35, and 41 MHz. The 19 MHz resonance decreases in Q when the rear attachment point is placed on the wing tip. This indicates that the mode is associated primarily with the delta-wing. For D, the spectra are again very similar, showing resonances at 7.5, 19.5, 29, and 41 MHz. A poorly excited resonance is indicated at about 14 MHz in both spectra.

Using the transfer functions, the square pulse was applied to produce the field waveforms shown in Figures 5.9 and 5.10 for configurations 1 and 2, respectively. The longitudinal B waveforms are identical until the reflections from the trailing edges of the wings and the rear fuselage occur. These are both contained in the first positive going pulse. Recall that negative longitudinal B indicates current flowing fore to aft and positive indicates current flowing in the opposite direction. The reflection from the rear of the fuselage is larger in configuration 2 than in configuration 1. This is because there is no longer a path for the current to leave the model from there, and thus more is reflected back toward the front. The

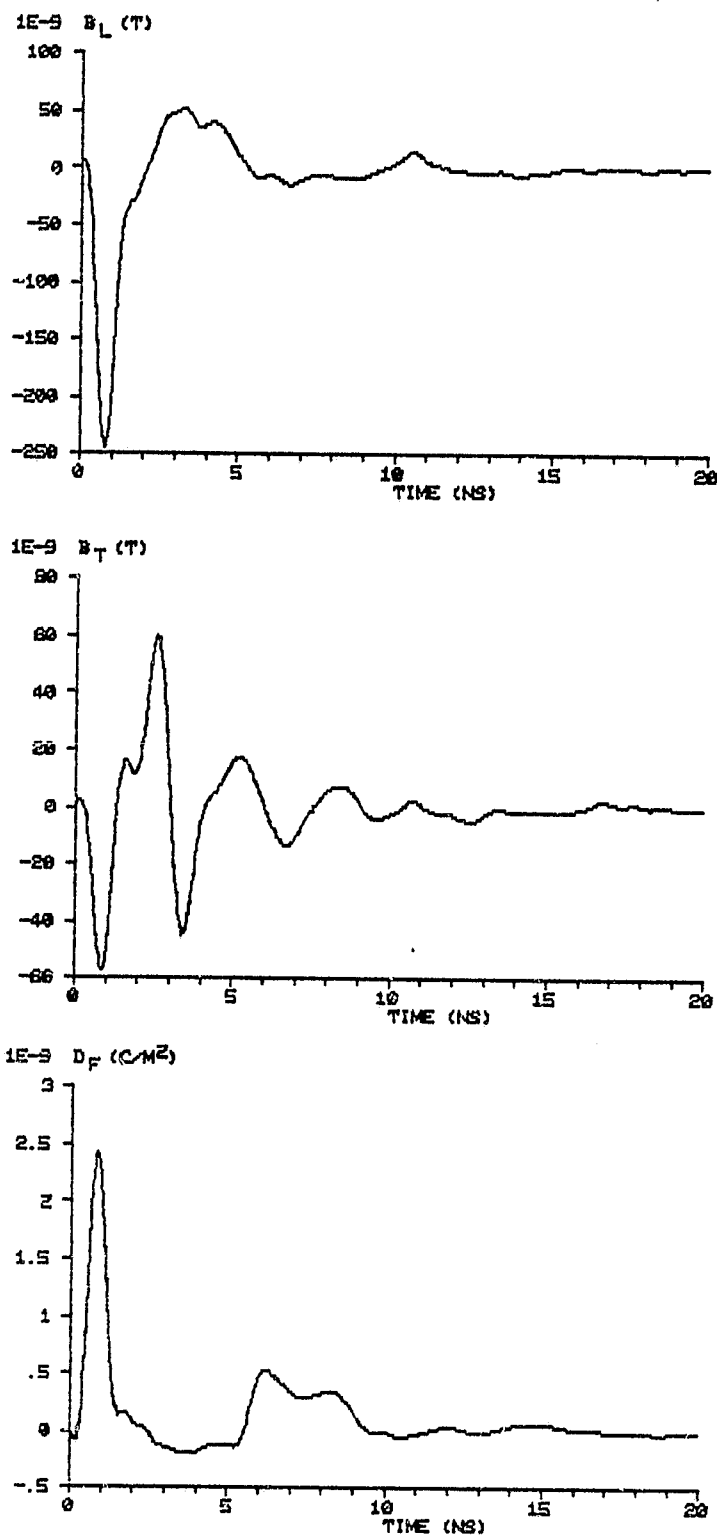


Figure 5.9. Field waveforms for model configuration 1.

ORIGINAL PAGE IS  
OF POOR QUALITY

77

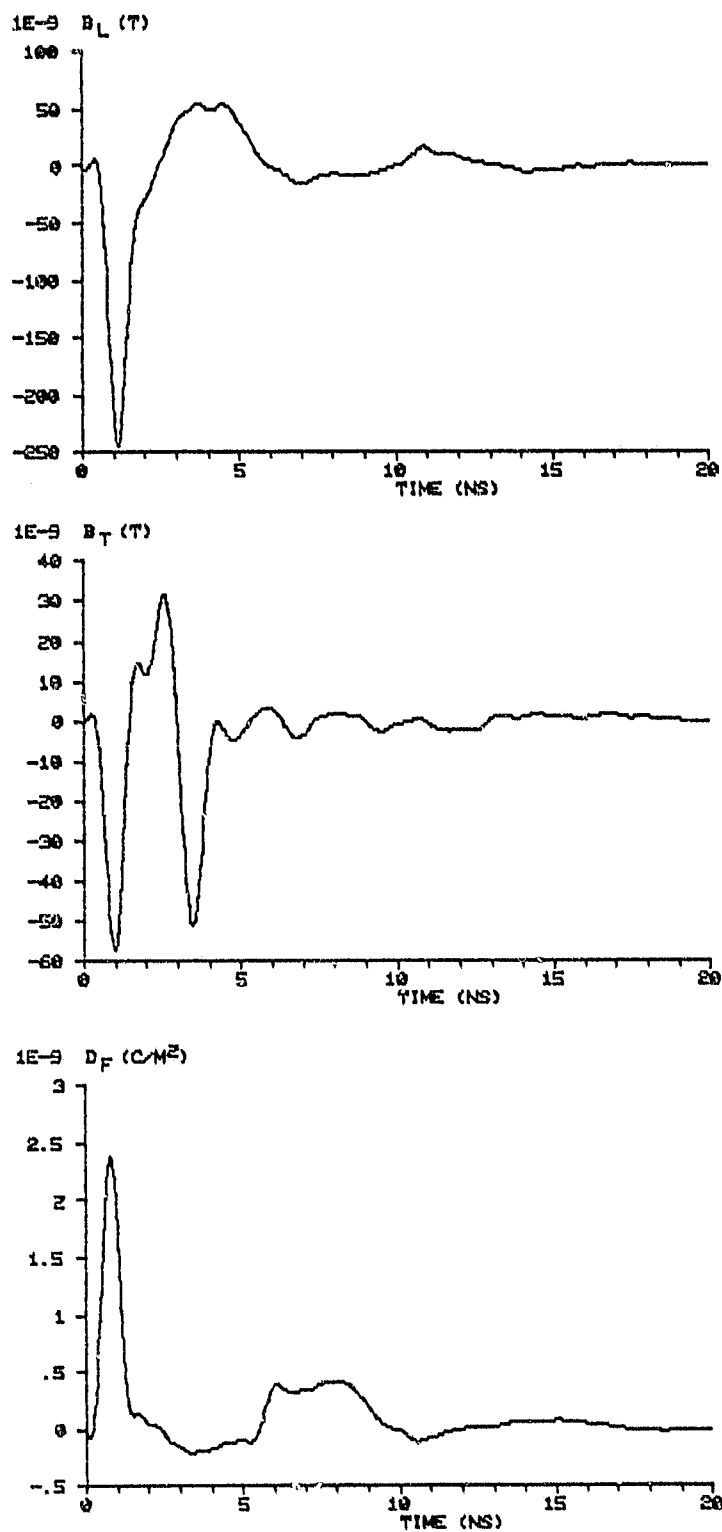


Figure 5.10. Field waveforms for model configuration 2.



transverse B waveforms do not show readily identifiable reflections. They do show highly resonant behavior looking very much like the sum of a few damped sinusoids. The heavier damping for configuration 2 as compared to 1 is apparent from the waveforms. Recall that negative transverse B indicates current flow from starboard to port and positive indicates current flowing in the opposite direction. The D waveforms are again virtually identical until the reflections from the rear occur as in longitudinal B. These are both contained in the second positive going pulse. The reason for the almost constant negative reflection between the two positive pulses is the decreasing impedance along the model caused by the wings, as discussed in the TDR section of this chapter.

### Configuration 3

The B-dot and D-dot waveforms for configuration 3 are shown in Figure 5.11. The transfer function magnitudes for the fields are shown in Figure 5.12. The spectrum from longitudinal B indicates resonances at 6, 19.5, and 29.5 MHz. Changes in the resonant frequencies after such a radical attachment point change are not surprising. The lowering of the lowest resonance is indicative of the fact that no

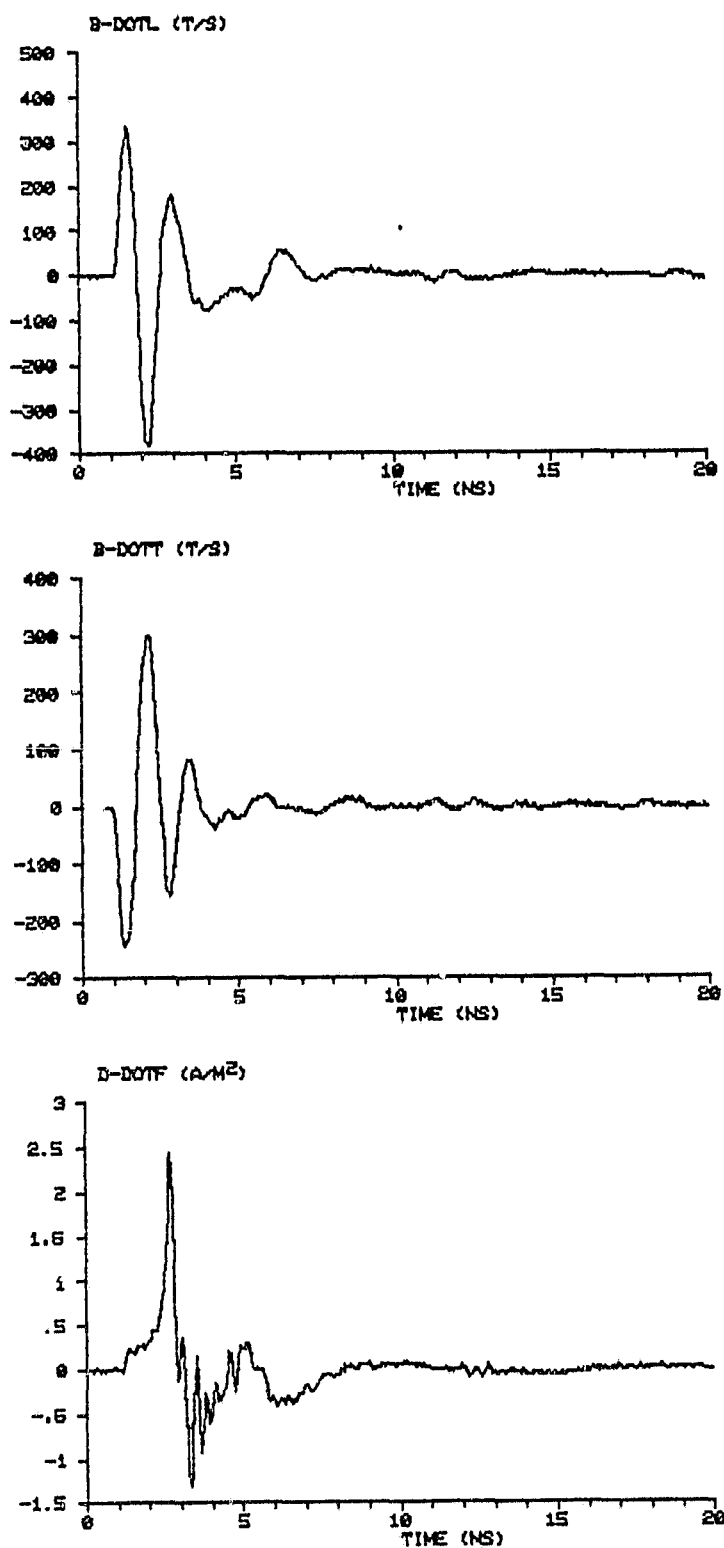
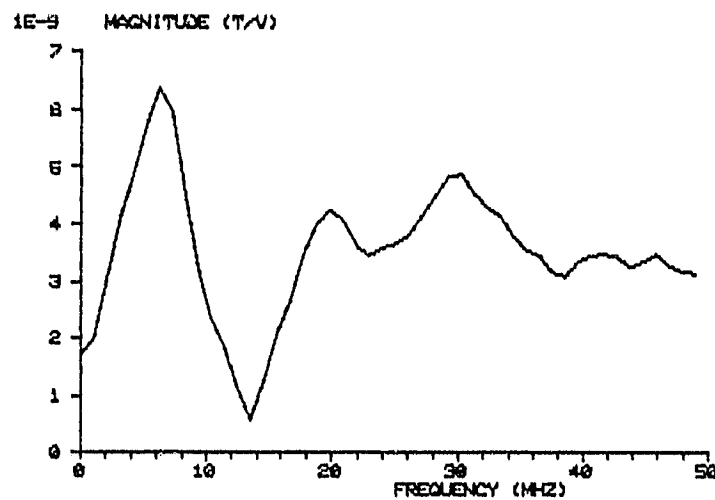
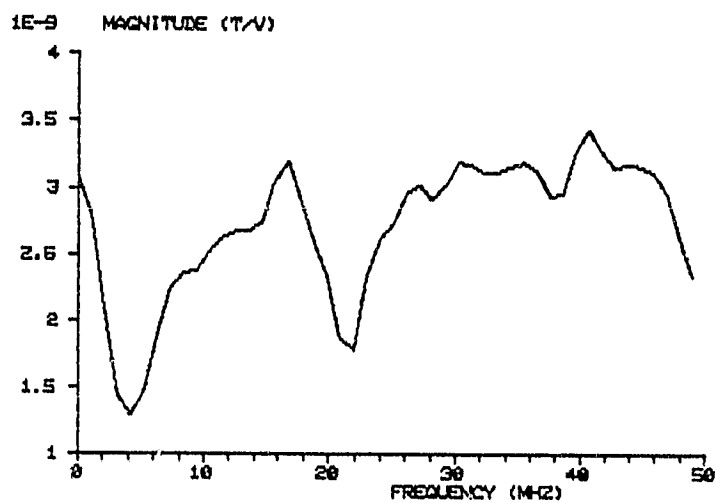


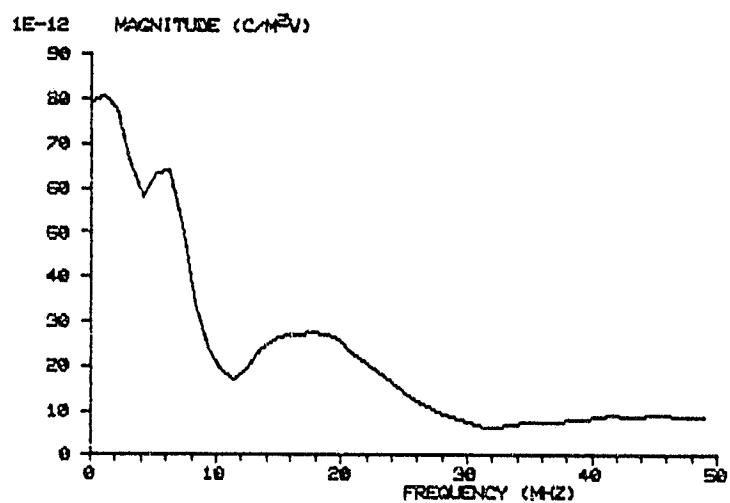
Figure 5.11. Measured waveforms from model configuration 3.



$B_L$



$B_T$



$D_F$

Figure 5.12. Transfer function magnitudes for model configuration 3.

wires now attach to the ends of the fuselage. This lowers the resonant frequency as was demonstrated in the cylinder analysis. The spectrum from transverse B shows the only recorded indication of a 16 MHz resonance. This dominates the lower half of the spectrum, which includes a well defined shoulder at 12 MHz. The upper half shows no dominant resonance except for the small peak at 41 MHz. For D, the spectrum is dominated by low frequencies. The peak at 6 MHz is small and the broad peak from 13 to 20 MHz possibly includes 3 different resonances. This waveform is the only one which does not reach zero before the clear time is over. Therefore, this spectrum will be affected by leakage due to the windowing of the data.

The field waveforms produced from the transfer functions are shown in Figure 5.13. The longitudinal B waveform shows a sizable amount of current flowing longitudinally toward the nose of the model, even with transverse excitation. However, this is to be expected since the current will concentrate itself at locations where the radius of curvature is small, such as the wing edge. The current thus flows toward the nose along the edge of the wing producing a longitudinal component. Otherwise, the field dies out very quickly after only about 7.5 ns. Transverse B shows current flowing initially from starboard to port, as expected from the excitation. As with longitudinal B, the field oscillations

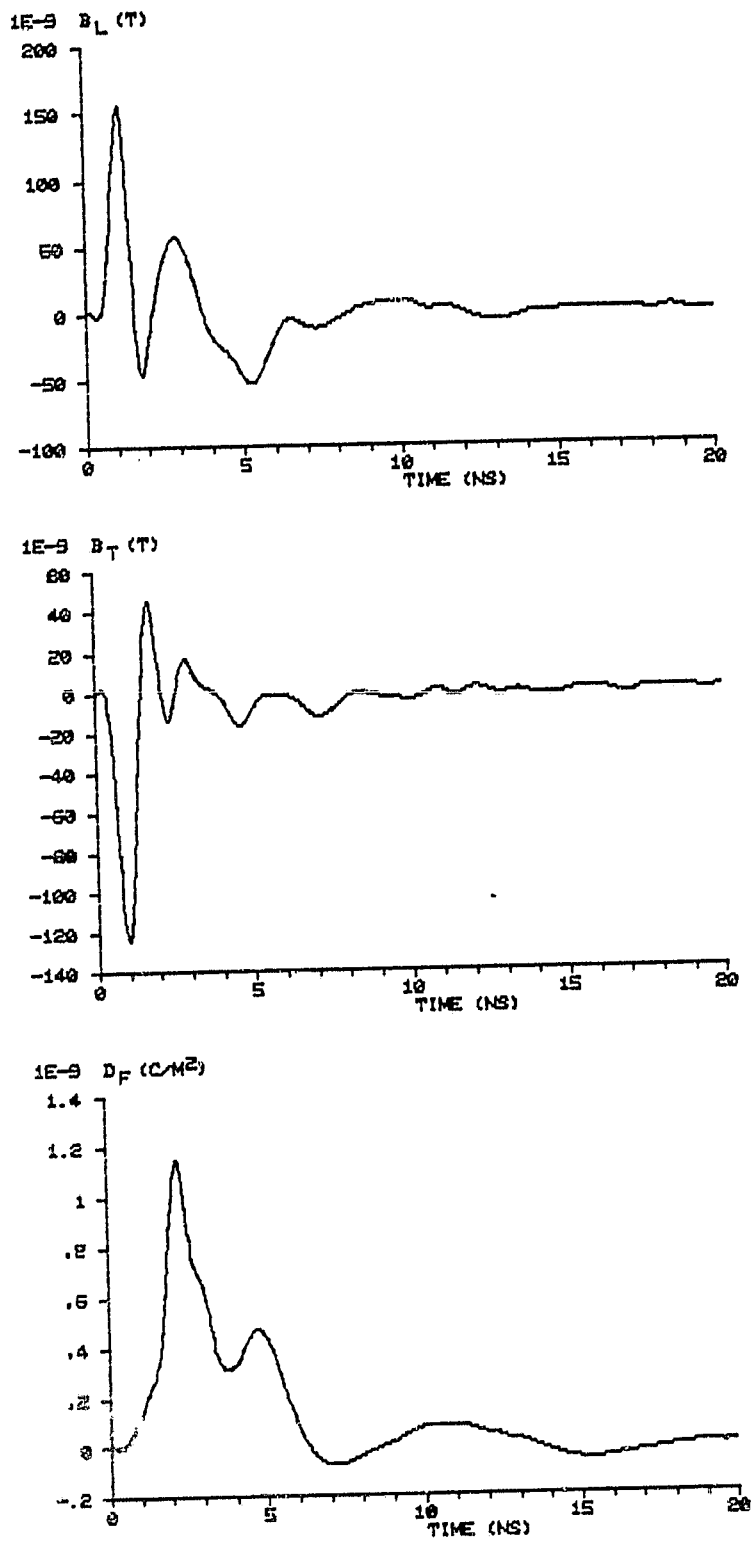


Figure 5.13. Field waveforms for model, configuration 3.

die out within about 7.5 ns. The D waveform has a very slow risetime, indicating that charging of the model is occurring. This charging will be discussed further in connection with configuration 4.

#### Configuration 4

The B-dot and D-dot waveforms for configuration 4 are shown in Figure 5.14. The transfer function magnitudes for the fields are shown in Figure 5.15. The spectrum from longitudinal B shows the 19 MHz resonance dominating, with weakly excited resonances at 14 and 35 MHz. The 7.5 MHz resonance is not excited by this particular configuration since it produces bi-directional current flow on the fuselage. The 7.5 MHz resonance corresponds to current flowing in the same direction as in a half-wavelength antenna. The spectrum from transverse B shows resonances at 13, 30, and 41 MHz. The D spectrum is heavily dominated by low frequencies and is uninteresting except for a small resonance at 19 MHz.

The field waveforms produced from the transfer functions are shown in Figure 5.16. The longitudinal B waveform indicates current initially flowing fore to aft superimposed upon an exponentially decaying current. Oscillations continue in the waveform until nearly 15 ns after the initial pulse. The transverse B waveform shows similar structure but with less of an exponential component. Current

ORIGINAL PAGE IS  
OF POOR QUALITY.

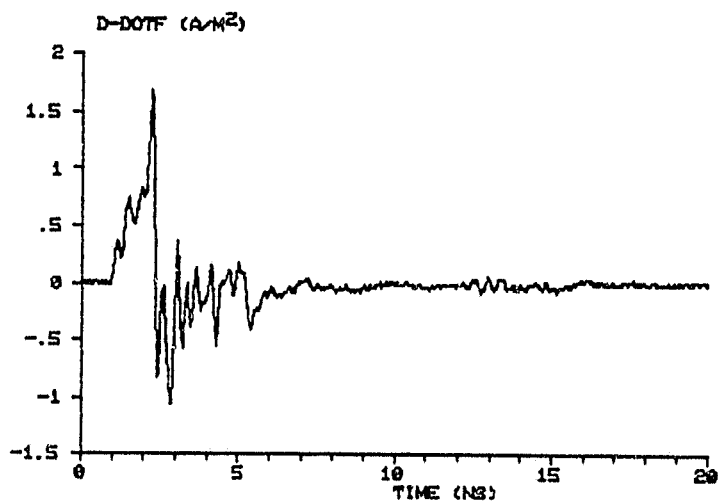
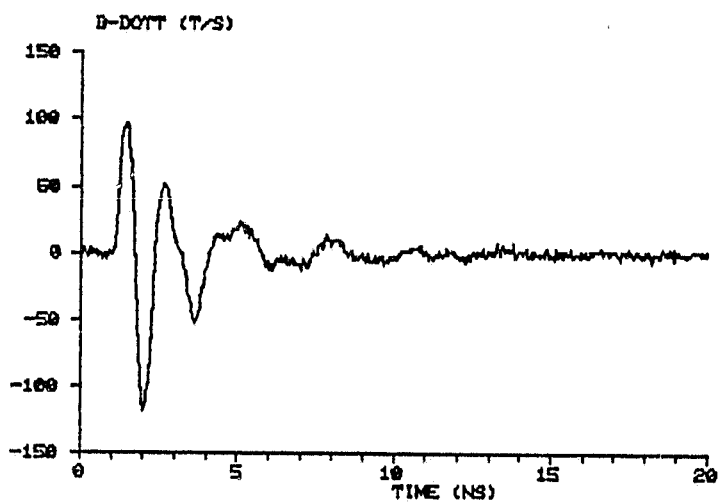
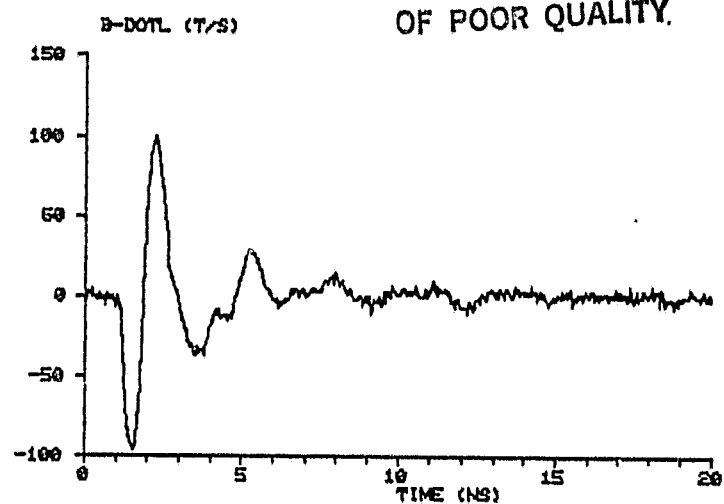
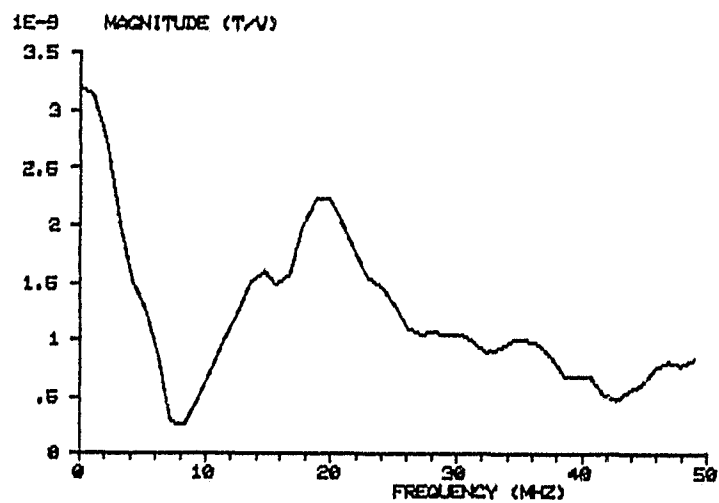
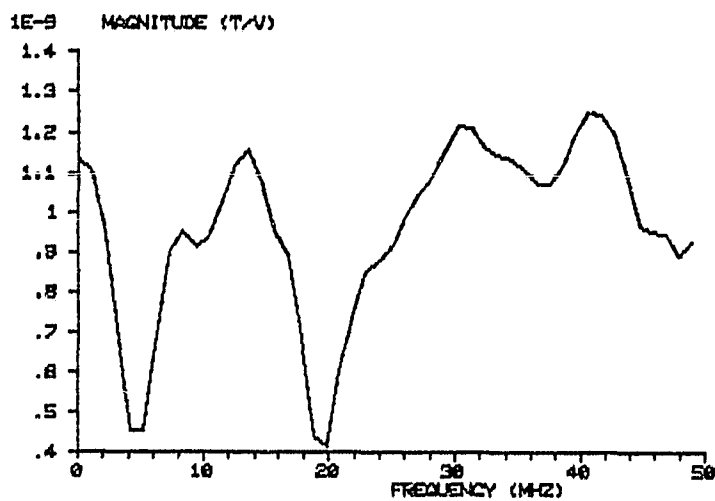


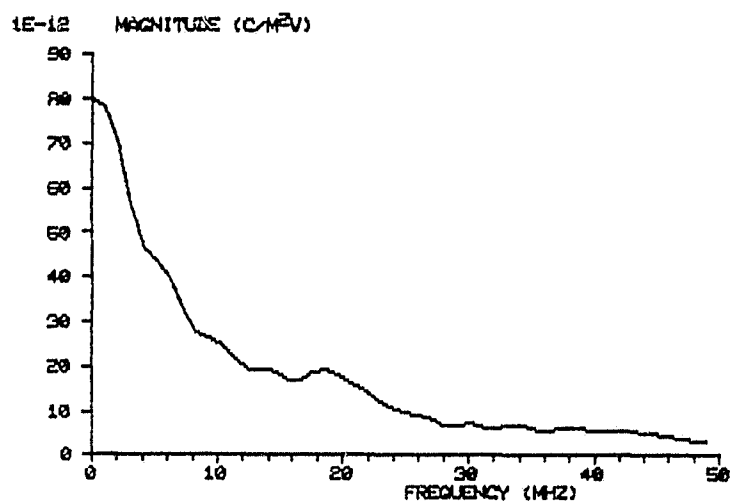
Figure 5.14. Measured waveforms from model configuration 4.



$B_L$



$B_T$



$D_F$

Figure 5.15. Transfer function magnitudes for model configuration 4.



ORIGINAL PAGE IS  
OF POOR QUALITY

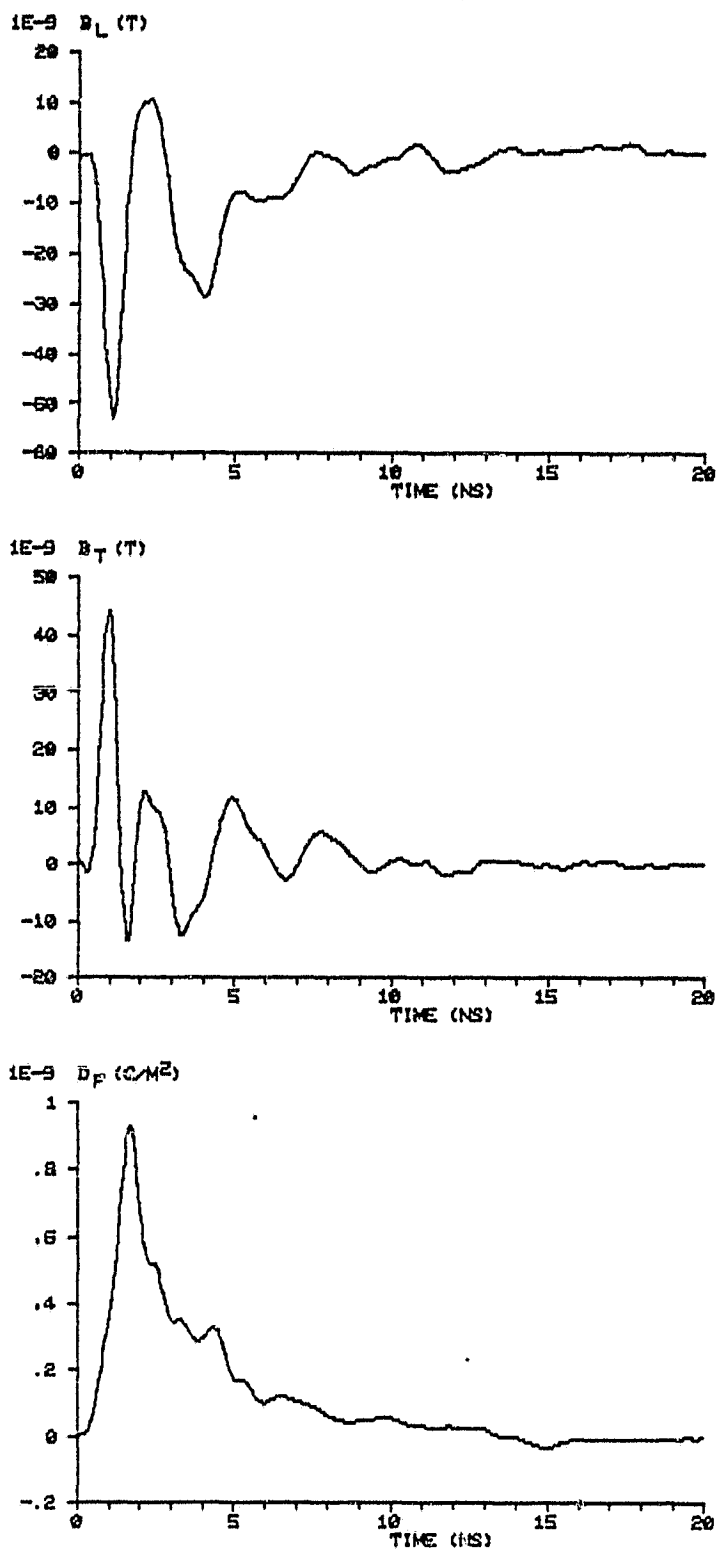
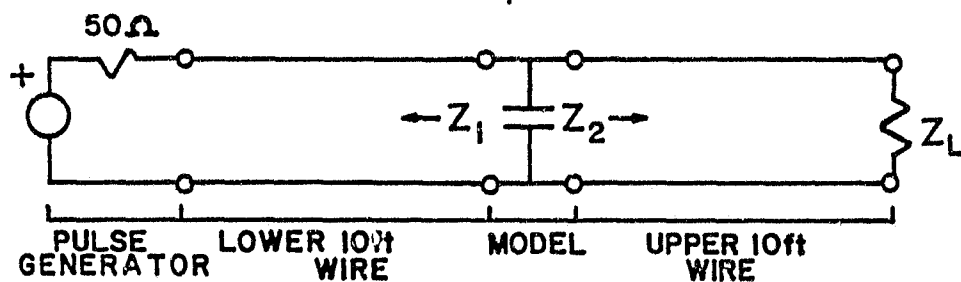


Figure 5.16. Field waveforms for model configuration 4.

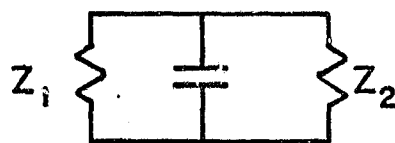
flows initially from port to starboard. The D waveform has a slow risetime and then an exponential decay to zero with little resonant structure on it. The explanation for the shapes of these waveforms is the following. The F-106B model can be thought of as being a capacitive blob placed on one conductor of a transmission line. The model is thus one plate of the capacitor and the ground plane is the other plate. Simple equivalent circuits for the apparatus and for the model and connecting wires are shown in Figures 5.17 a and b, respectively. As the short pulse from the generator arrives at the model, it is charged quickly since the pulse resembles an impulse, which would charge it instantaneously. The charging time corresponds to the risetime of the electric flux density D. The charging current of a capacitor is proportional to the derivative of the voltage across it, so the magnetic flux density waveforms show current pulses during this charging time. In other words, the B waveforms are like the derivative of the D waveform. After the charging is completed, the capacitor discharges at a rate determined by the impedances in the equivalent circuit in Figure 5.17b. This explains the presence of the exponential decay in D and also in the B waveforms since they are proportional to the derivative of D.

A summary of the resonances from the transfer function magnitude spectra of the four configurations is given in

ORIGINAL PHOTO IS  
OF POOR QUALITY



a. Apparatus



b. Model and wires (for  $t \leq 20$  ns)

Figure 5.17. Approximate equivalent circuit for apparatus and model with connecting wires.

5-2

Table 5.1. Table 5.2 lists the resonances in ascending frequency order and indicates which waveforms contain which resonances. The resonant frequencies listed are the average values from the different configurations.

The resonant frequencies listed in Table 5.2 can be compared with those predicted using the stick modeling described in Chapter III. The model used was that shown in Figure 5.18, which also shows the stick lengths used. The resonances for this particular stick model are 6.8, 11, 17.2, 24.5, 28.9, 34.7, and 41.6 MHz. These correspond rather well with those in Table 5.2 except for the 11 and 17.2 MHz values. The 17.2 may be the 19.5 MHz resonance in error, which is possible since all indications are that this resonance is due primarily to the flat plate delta-wing, which is not well modeled by the sticks. It could also be the 16 MHz resonance slightly in error. This would mean that the 19.5 MHz resonance is not predicted at all. The 11 MHz is likely the 12.8 MHz resonance in error, again due to the wings. The general nature of these resonances agrees with those computed for the B-1 aircraft [25]. Specifically, the second resonance is approximately 50% above the first. Overall, the stick model results tend to agree with the locations of the resonances as determined from the transfer functions.

Prony analysis was next applied to all 12 field waveforms from the four configurations. The order was initially

TABLE 5.1. RESONANCES OF F-106B MODEL

Configuration 1 Resonances, MHz

$B_L$	$B_T$	$D_F$
7.5	19	7.5
13	24.5	19.5
19.5	35	29
24	41	41
35		

Configuration 3 Resonances, MHz

$B_L$	$B_T$	$D_F$
6	12	6
19.5	16*	
29.5	41	

Configuration 2 Resonances, MHz

$B_L$	$B_T$	$D_F$
7.5	19	7.5
13	24.5	19.5
19.5	35	29
24	41	41
35		

Configuration 4 Resonances, MHz

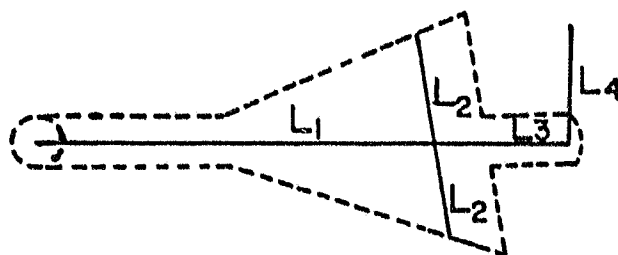
$B_L$	$B_T$	$D_F$
19	13	19
	30	
	41	

\* only occurrence

TABLE 5.2. RESONANCES OF F-106B MODEL

Resonance	Config. 1			Config. 2			Config. 3			Config. 4		
	B <sub>L</sub>	B <sub>T</sub>	D <sub>F</sub>	B <sub>L</sub>	B <sub>T</sub>	D <sub>F</sub>	D <sub>L</sub>	B <sub>T</sub>	D <sub>F</sub>	B <sub>L</sub>	B <sub>T</sub>	D <sub>F</sub>
7	X		X	X		X	X		X			
13	X			X				X			X	
16								X				
19	X	X	X	X	X	X	X			X		X
24	X	X		X	X							
29			X			X	X				X	
35	X	X		X	X							
41		X	X		X	X		X			X	

ORIGINAL PAGE IS  
OF POOR QUALITY



$$L_1 = 27 \text{ in.}$$

$$L_2 = 10 \text{ in.}$$

$$L_3 = 9 \text{ in.}$$

$$L_4 = 7.5 \text{ in.}$$

Figure 5.18. Stick model configuration.

assumed to be 20 and increased until the maximum order of 36 was reached. Consistent results were just beginning to be seen at this high order and so it was used for all model waveforms. Only three windows were used in the sliding window method to save computer run time, which becomes large when such a high order is used. It is still easy to distinguish the physical from the curve-fitting poles using only 3 windows. Every 6th point was taken in the waveforms yielding a sampling interval of 300 ps and a folding frequency of 1.7 GHz, still above the highest frequency content of the waveforms.

The dominant natural frequencies for configurations 1 and 2 are shown in Figure 5.19. Those for configuration 3 and 4 are shown in Figures 5.20 and 5.21, respectively. The values of the natural frequencies are listed in Table 5.3 for each configuration. These values are averages derived from the sliding window method. Each natural frequency for a given configuration was taken from whichever waveform had that particular resonance most dominant.

Figure 5.19 shows 4 dominant natural frequencies. Note that as the wire is moved from the fuselage to the wing, the first two show a decreased damping rate. This indicates that the modes had current flowing off of the rear wire, which was stopped when the wire was removed from the fuselage. Therefore, these modes both involve current flow on the rear of the fuselage. The third shows the opposite effect with



ORIGINAL PAGE IS  
OF POOR QUALITY

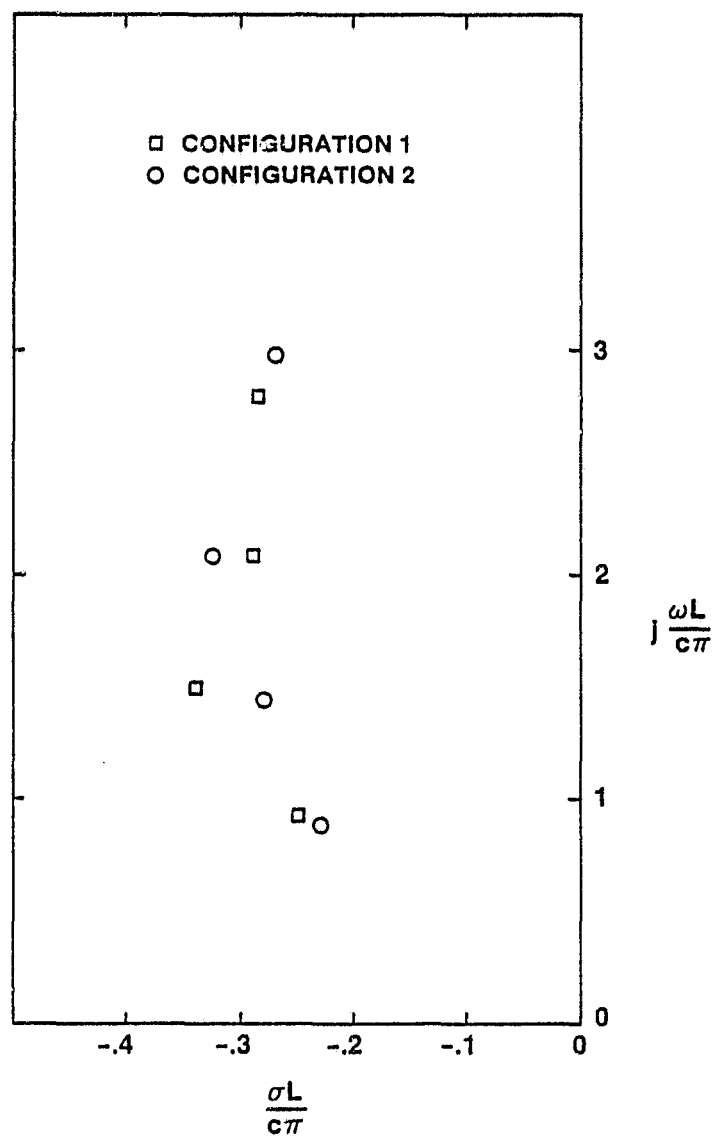


Figure 5.19. Dominant natural frequencies of model configurations 1 and 2.

ORIGINAL MODEL IS  
OF POOR QUALITY

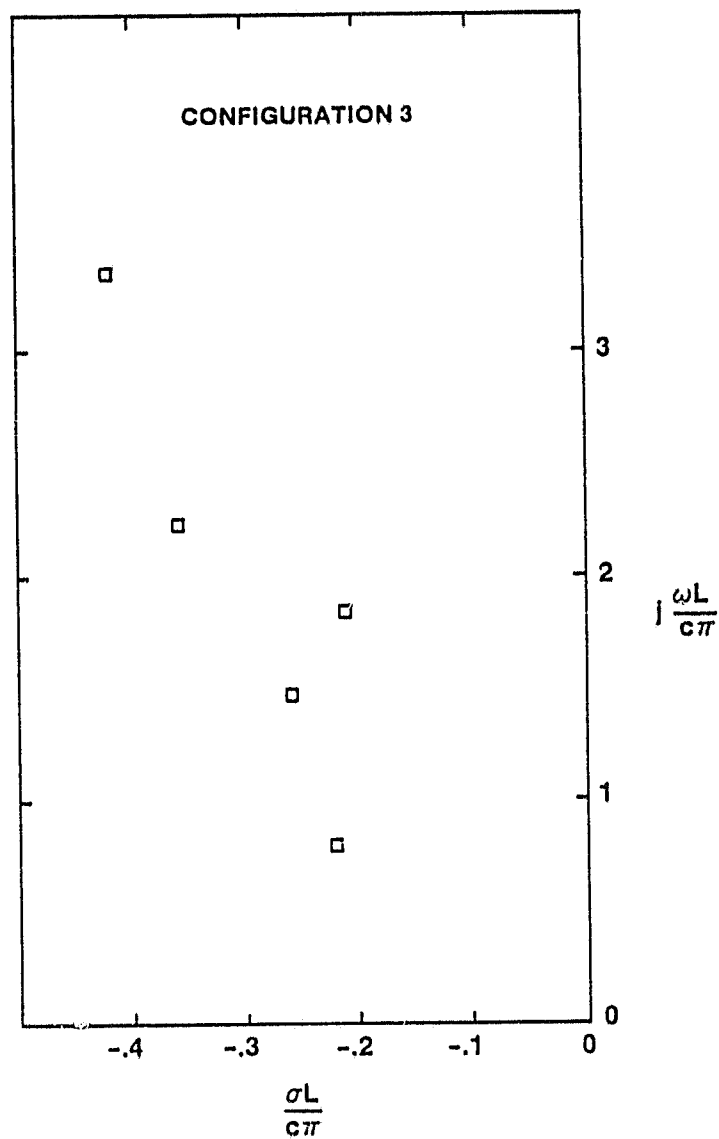


Figure 5.20. Dominant natural frequencies of model configuration 3.

ORIGINAL PAGE IS  
OF POOR QUALITY

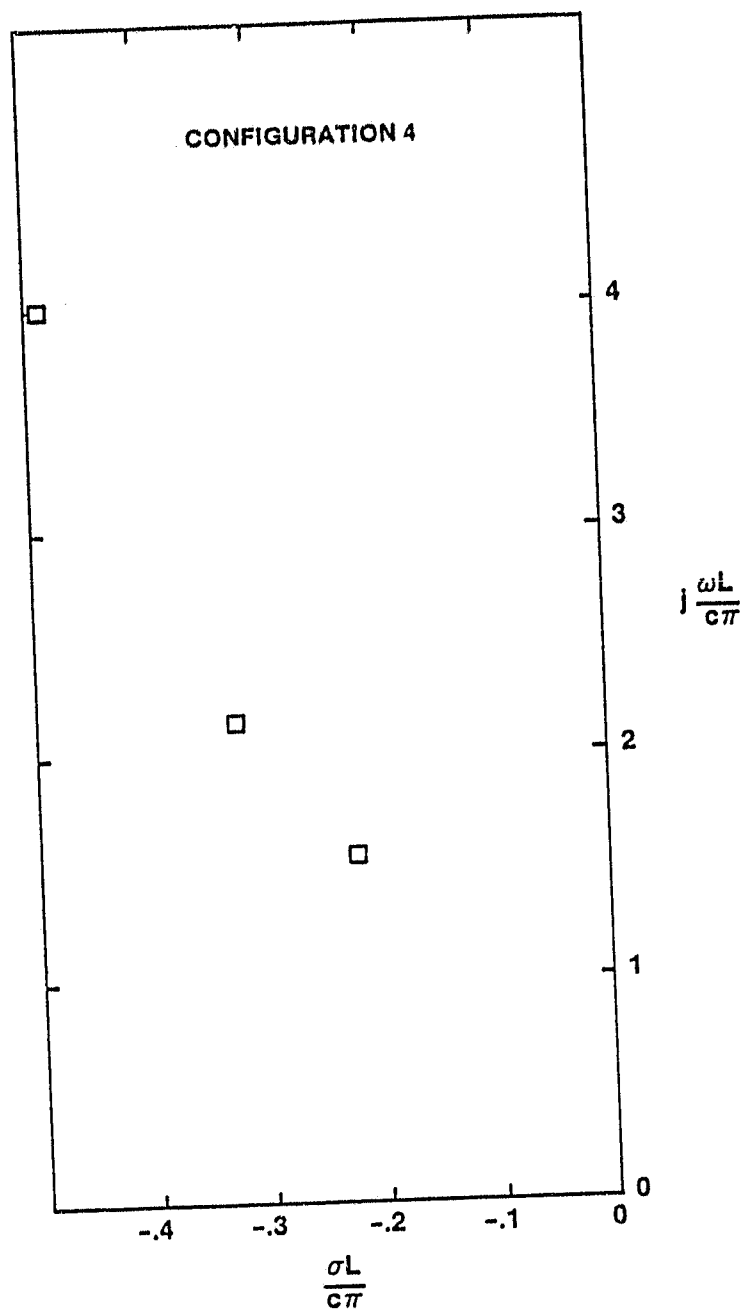


Figure 5.21. Dominant natural frequencies of model configuration 4.

TABLE 5.3. NATURAL FREQUENCIES OF F-106B MODEL

Configuration 1		Configuration 2	
Natural frequency	f,MHz	Natural frequency	f,MHz
$-.25 + j0.93$	8.1	$-.23 + j0.88$	7.7
$-.34 + j1.50$	13.1	$-.28 + j1.45$	12.6
$-.29 + j2.09$	18.2	$-.35 + j2.09$	18.2
$-.28 + j2.80$	24.4	$-.27 + j2.98$	25.9

Configuration 3		Configuration 4	
Natural frequency	f,MHz	Natural frequency	f,MHz
$-.22 + j0.80$	7.0	$-.22 + j1.55$	13.5
$-.26 + j1.47$	12.8	$-.33 + j2.15$	18.8
$-.21 + j1.84$	16.1*	$-.49 + j4.00$	34.9
$-.36 + j2.23$	19.5		
$-.42 + j3.35$	29.3		

\* only occurrence

heavier damping. This mode is due primarily to the delta-wing and so the current flows off when the wire is attached to the wing tip. The fourth natural frequency was poorly excited compared to the first three and shows a change in frequency rather than damping.

Figure 5.20 for configuration 3 includes 5 dominant natural frequencies. The one which appears out of line with the others is the one at 16 MHz in its only appearance. The other configurations do not excite this mode.

Figure 5.21 for configuration 4 includes only 3 dominant natural frequencies. Note again that the lowest one is not present indicating that it was not excited in this particular configuration.

The values of the natural frequencies in Table 5.3 correspond well to the transfer functions. The damping rates compare favorably with the width of the peaks and the resonant frequencies compare well with the centers of the peaks except in configuration 3, where the Prony analysis does not show the low 6 MHz resonance but puts it at 7 MHz. The frequency has indeed been lowered in this configuration, but the transfer function spectrum has too much quantization error to obtain the resonant frequency accurately. The Prony analysis is the more accurate spectral estimator of the two methods. The 41 MHz resonance was also extracted by the Prony analysis,

but it was not included because it is above the bandwidth of the B-dot sensor and is probably unreliable.

The Prony analysis has yielded natural frequencies which agree well with the resonances shown in the transfer function spectra. Comparisons of these results with computations on direct and nearby strike data in the next chapter will shed new light on the nature of the lightning channel.

## CHAPTER VI

### COMPARISONS WITH IN-FLIGHT DATA

#### Overview

A discussion of the in-flight lightning strike data obtained in the 1980 and 1981 campaigns is given in reference [14]. A total of 20 strikes to the aircraft were reported along with several nearby strikes. Observations discussed here are for magnetic and electric fields measured with the longitudinal B-dot sensor over the starboard wing and the nose D-dot sensor. The bandwidth of these measurements is 50 MHz with a sampling interval of 10 ns. Lightning pulse lengths ranging from 25 ns to 7  $\mu$ s have been observed.

The strikes seen thus far have had relatively small peak currents, typically hundreds of amperes. On one occasion, however, an I sensor on the noseboom recorded a large stroke of 14 kA peak current shortly after the B-dot sensor had triggered on a very small pulse. Thus, it appears that streamering on the aircraft may be occurring which triggers the derivative sensors and causes subsequent large-current strokes to be missed. Even so, these short, small excitations contain high frequencies which excite aircraft resonances.

### Direct Strikes

Five examples of B-dot records from direct lightning strikes to the aircraft are shown in Figures 6.1 through 6.5, along with their frequency spectra, magnitude only. Two D-dot records are shown in Figures 6.6 and 6.7. All records are from 1980 flight 38 except for the D-dot in Figure 6.7 from flight 18.

In some cases, particularly in Figures 6.1 and 6.2, the spectra indicate that aliasing is present since the magnitudes do not approach zero at the 50 MHz folding frequency but are actually increasing. Although the sensor outputs are low-pass filtered at 50 MHz, the filter attenuation is rather gradual and some higher frequencies are allowed to pass through to the digitizers. Probably this affects only the higher frequency range of the spectra between 25 and 50 MHz.

Comparisons of the spectral peaks with those for the model show excellent agreement except for the 19 MHz resonance, which appears consistently at 21 MHz in the in-flight data. This resonance is due to the delta-wing and the discrepancy might be explained by the fact that the elevons on the rear of the wing are somewhat electrically isolated from the rest of the aircraft. They make up about 10% of the wing and aft fuselage surface area which accounts for the frequency increase on the F-106B. Two examples of a 16 to 18 MHz resonance are seen. One is the small 16 MHz peak in the



ORIGINAL PAGE IS  
OF POOR QUALITY

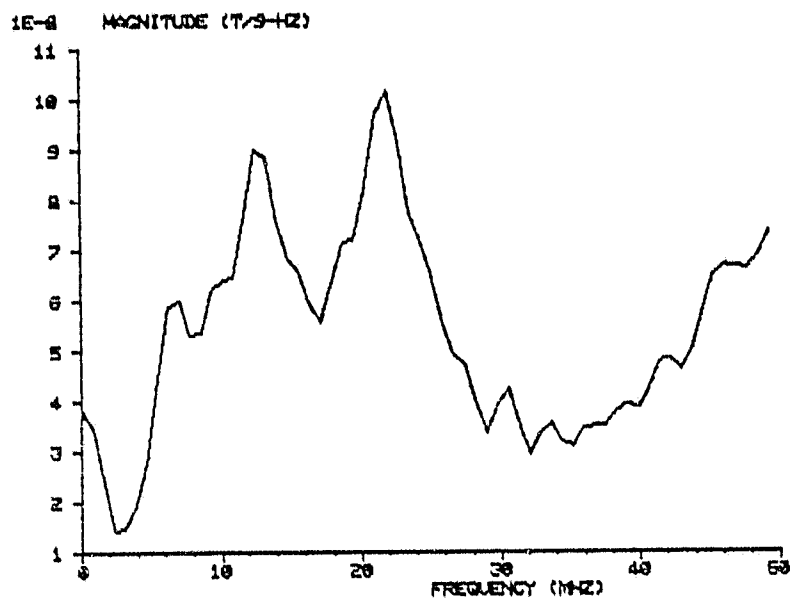
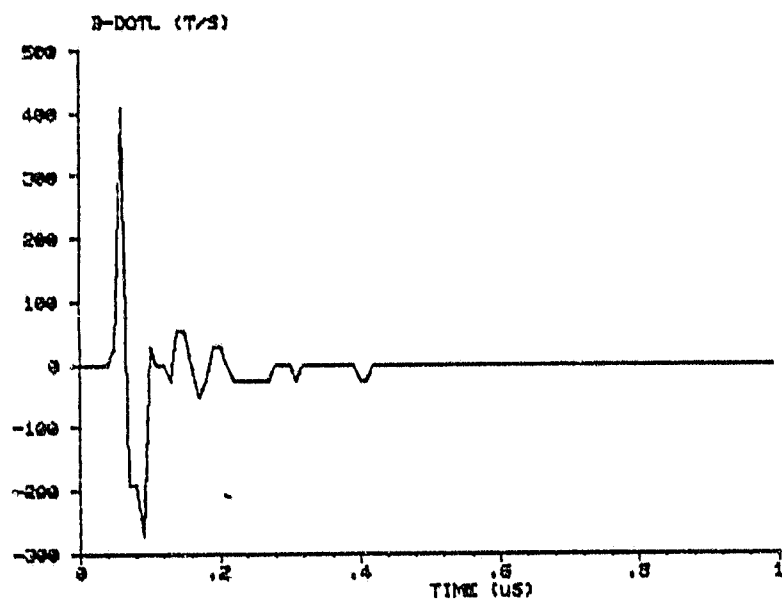


Figure 6.1. B-dot record from direct strike 80-038-01.

ORIGINAL PAGE IS  
OF POOR QUALITY

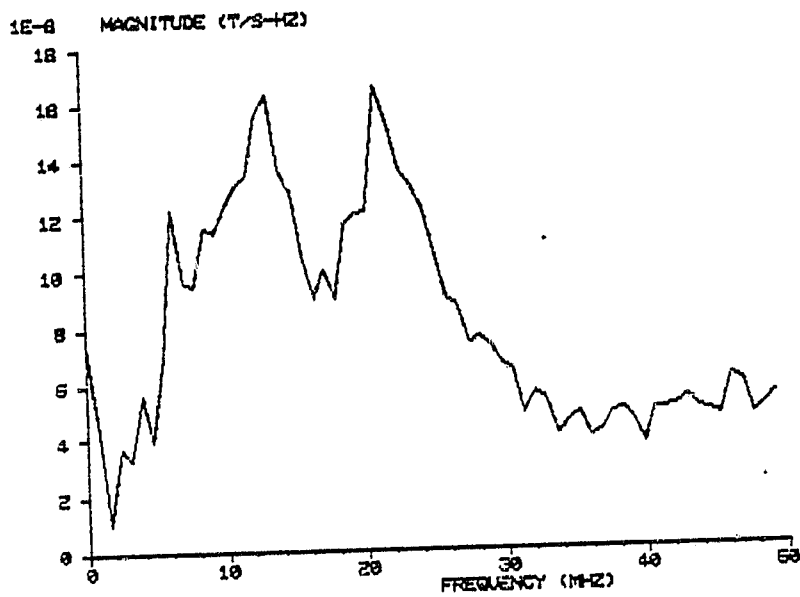
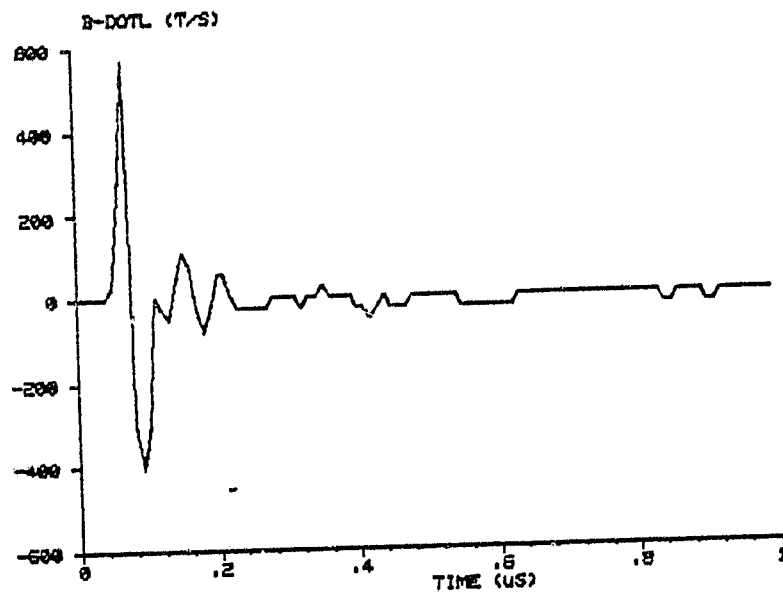


Figure 6.2. B-dot record from direct strike 80-038-05.

ORIGINAL PAGE IS  
OF POOR QUALITY

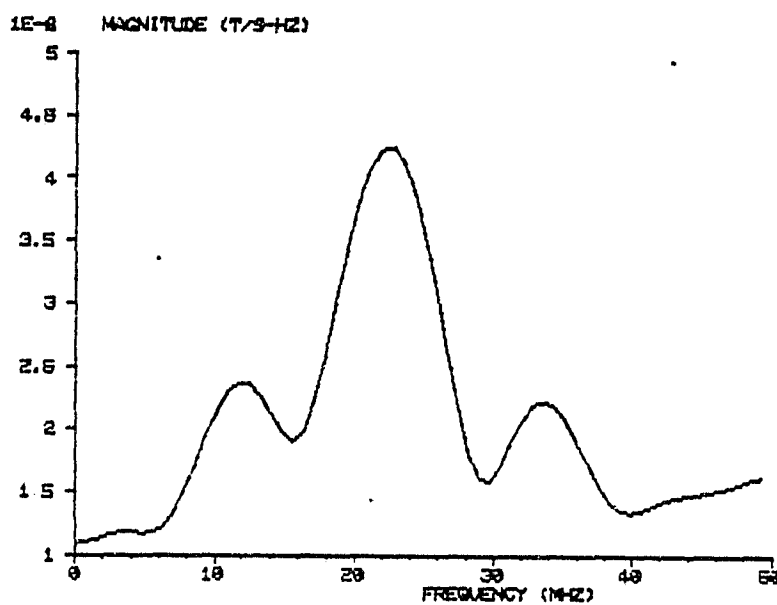
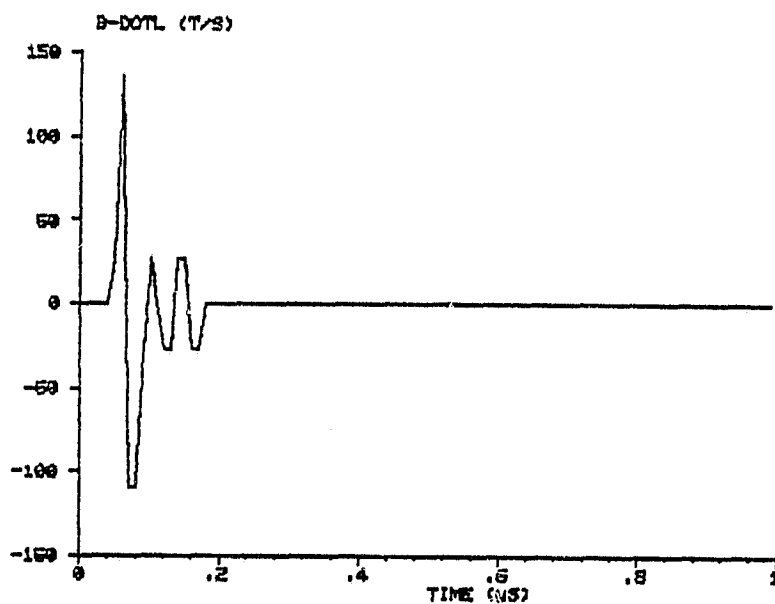


Figure 6.3. B-dot record from direct strike 80-038-03A.

ORIGINAL PAGE IS  
OF POOR QUALITY

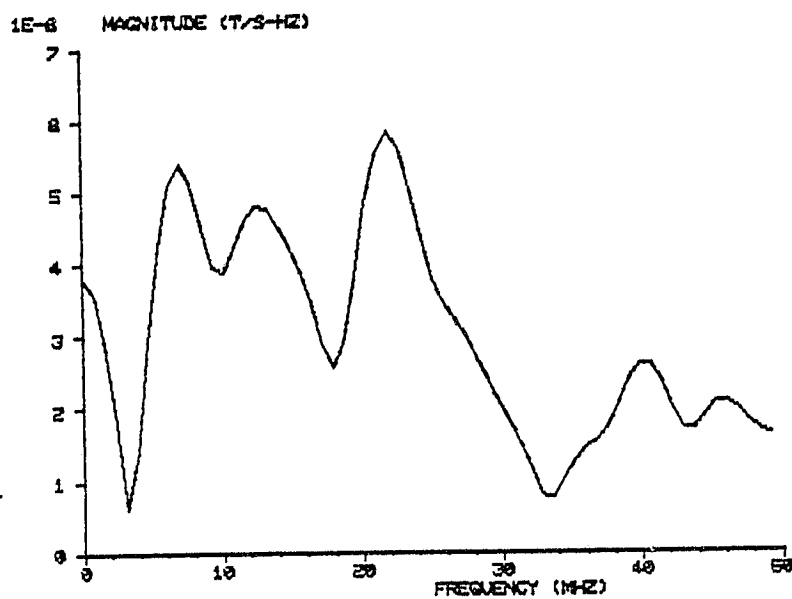
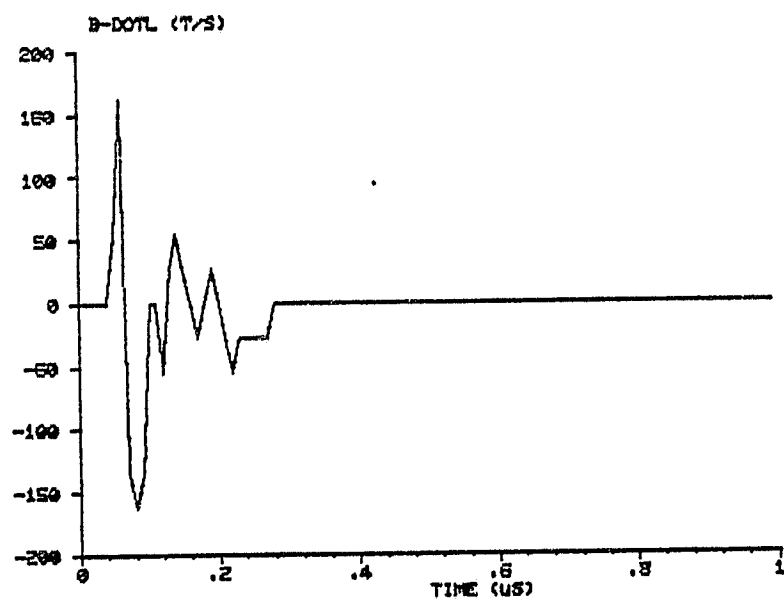


Figure 6.4. B-dot record from direct strike  
80-038-03B.

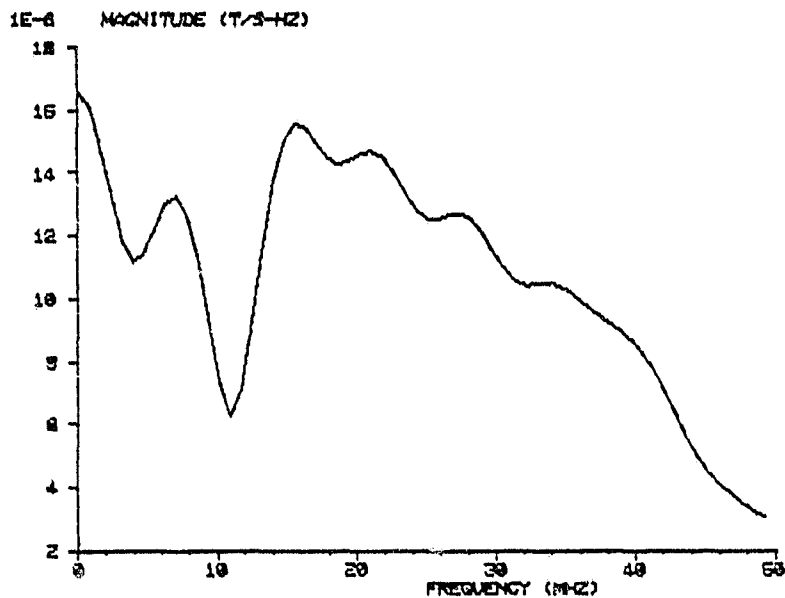
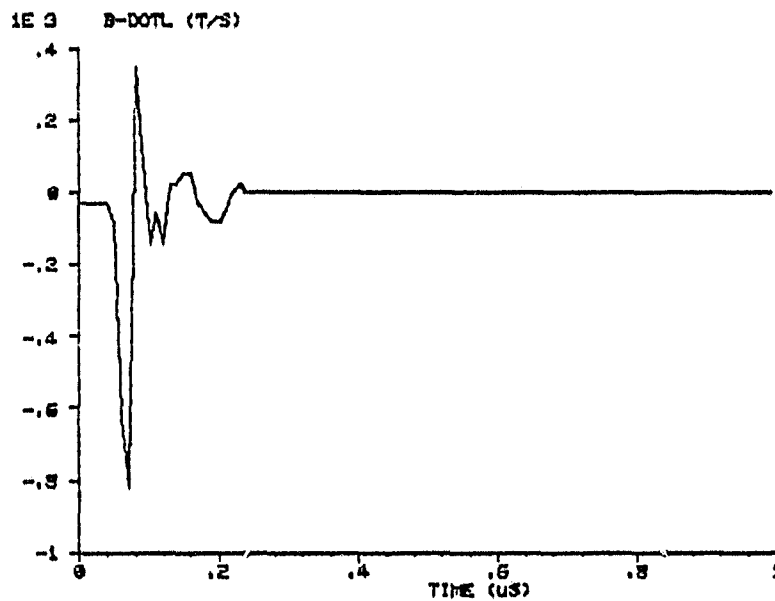


Figure 6.5. B-dot record from direct strike 80-038-04.

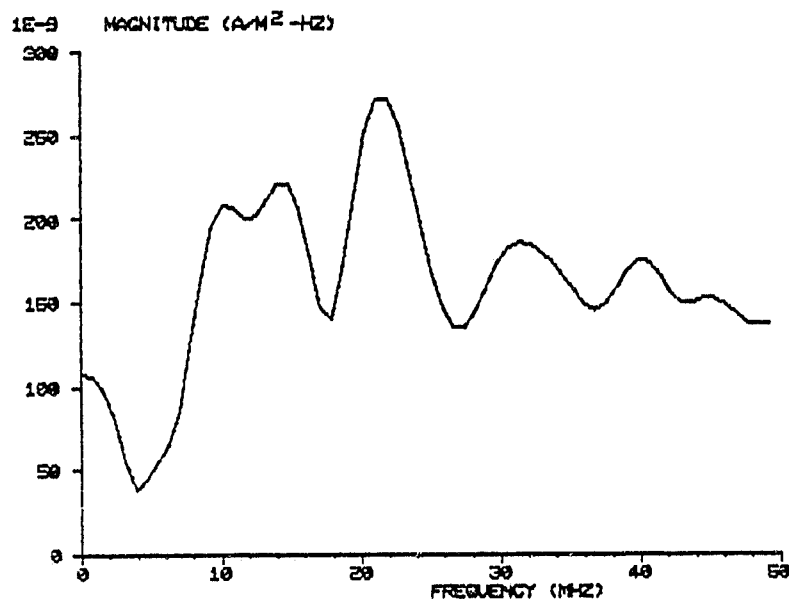
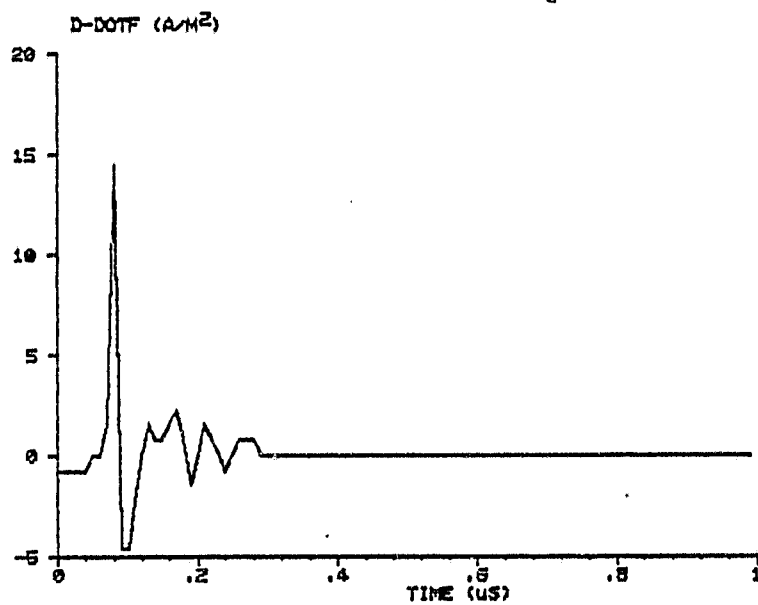
ORIGINAL RECORD  
OF POOR QUALITY

Figure 6.6. D-dot record from direct strike 80-038-04.

ORIGINAL PAGE IS  
OF POOR QUALITY

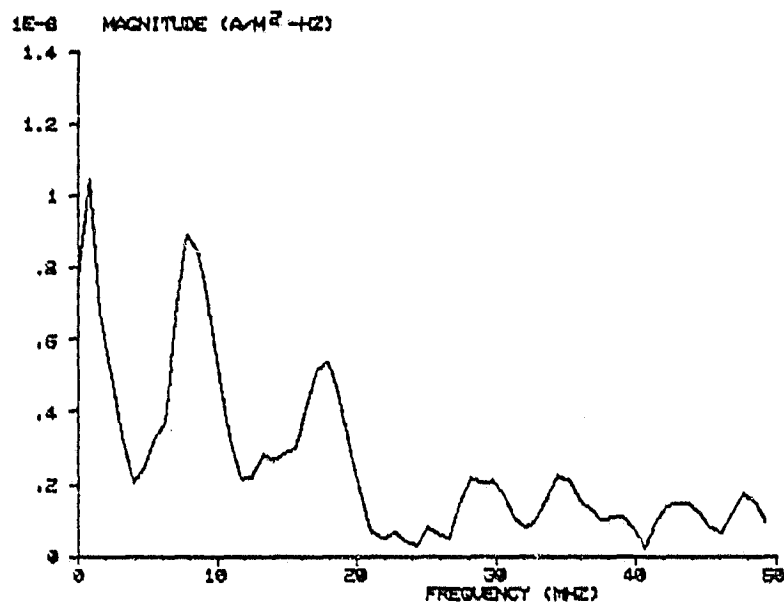
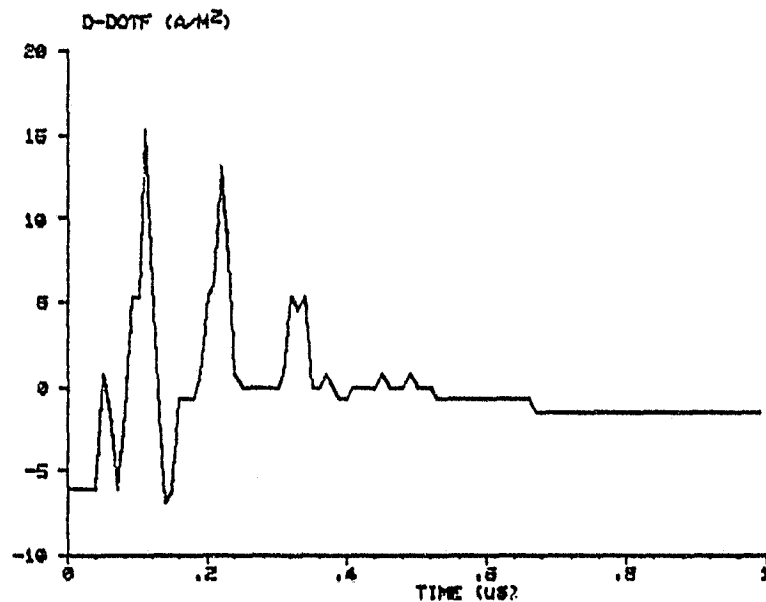


Figure 6.7. D-dot record from direct strike 80-018-01.

B-dot spectrum of Figure 6.5 and the other is the 17.5 MHz peak in the D-dot spectrum of Figure 6.7. The higher frequency peaks in the various spectra also show the higher resonances seen on the model. A summary of the resonant frequencies indicated in the direct-strike data is given in Table 6.1. All model resonances are seen except for the 24 MHz resonance where only a small shoulder is indicated in 3 spectra. B-dot 38-4 and D-dot 38-4 have spectral peaks below and above the 29 MHz resonance, respectively.

Prony analysis has been applied to all the above direct-strike records. The methods used were identical to those used in previous chapters. A difficulty to be expected in this is that the lightning, which is the input to the aircraft-channel system, will contribute some natural frequencies to the measured waveforms. These must be fitted by the Prony analysis along with those from the system, presenting added difficulty to the extraction of accurate natural frequencies of the system.

The results from these Prony analyses are given in Table 6.2. The natural frequencies from flight 38 B-dot records 1 and 5 are almost identical. This was expected due to the similarity of the spectra from the two. Of the three natural frequencies from record 3A, the second agrees well with the corresponding one in records 1 and 5. The first has greater



TABLE 6.1. F-106B RESONANCES FROM IN-FLIGHT DIRECT LIGHTNING STRIKES

Model Resonance	38-1	38-5	B-dot 38-3A	38-3B	38-4	D-dot 38-4	18-1
7	6.2	6.2		7.0	7.0		8.0
13	13.0	13.0	12.0	12.5			
16					16.0		17.5
19	21.0	21.0	22.2	22.0	21.0	22.0	
24	*	*		*			
29					27.0	31.0	29.0
35			34.0				35.0
41				40.5		40.5	

\* shoulder

ORIGINAL PAGE IS  
OF POOR QUALITY

TABLE 6.2. NATURAL FREQUENCIES FROM DIRECT-STRIKE IN-FLIGHT DATA

B-dot

38-1		38-5	
Natural frequency	f,MHz.	Natural frequency	f,MHz
$-.215 + j1.50$	13.1	$-.21 + j1.54$	13.4
$-.295 + j2.50$	21.8	$-.31 + j2.48$	21.7

38-3A		38-3B	
Natural frequency	f,MHz	Natural frequency	f,MHz
$-.26 + j1.34$	11.7	$-.29 + j0.73$	6.3
$-.32 + j2.48$	21.6	$-.26 + j1.28$	11.1
$-.22 + j4.00$	34.9	$-.37 + j2.53$	22.1

38-4	
Natural frequency	f,MHz
$-.23 + j0.90$	7.8
$-.27 + j1.61$	14.1
$-.30 + j4.02$	35.1
$-.47 + j4.61$	40.2

D-dot

38-4		18-1	
Natural frequency	f,MHz	Natural frequency	f,MHz
$-.29 + j2.54$	22.1	$-.08 + j0.86$	7.7
		$-.13 + j2.03$	17.7

ORIGINAL OF  
POOR QUALITY

damping and lower frequency and the third was not present in either previous record. Record 3B is the first to show the aircraft's lowest natural frequency. It has greater damping than that seen before for the lowest resonance in either in-flight or model data. The third is also highly damped compared to other in-flight results. Only the first natural frequency from record 4 corresponds well to a peak in its spectrum. This spectrum is unusual since it is almost smooth except for a dip at 11 MHz. The other natural frequencies at 14, 35, and 40 MHz do not correspond well to peaks in the spectrum but do correspond fairly well with aircraft resonances, however. The dominant natural frequency in D-dot record 4 agrees with previous results.

D-dot record 1 from flight 18 shows the lowest damping recorded in the in-flight data. It is also unusual in that it contains resonant oscillations with a step occurring after they begin. The reason for the low damping is unclear unless it is indicative of more than one lightning pulse.

#### Nearby Strikes

Results from nearby strikes can be used to determine the natural frequencies of the F-106B for the case of no channel attachment. This is the limiting case where the damping is the lightest. Again, the lightning itself is the system input for these records and problems may occur in the accurate extraction of the aircraft resonances.

ORIGINAL PAGE IS  
OF POOR QUALITY

B-dot and D-dot records from a nearby lightning strike are shown in Figures 6.8 and 6.9, respectively, along with their corresponding magnitude spectra. The B-dot record utilized only 8 levels of quantization in the largest peak whereas the D-dot record used 31. The B-dot will thus suffer more from quantization error. Aliasing is also present in both magnitude spectra. The first four aircraft resonances are shown at 7.3, 11.9, 15.4, and 21 MHz, the 15.4 MHz being only a shoulder in each spectrum. These are in agreement with those obtained from the model and previous in-flight data. D-dot waveforms and spectra from two other nearby strikes are shown in Figures 6.10 and 6.11. These waveforms are unusual because of their unipolar shape, which indicates that D increased to some value and remained there. The spectra show the first aircraft resonance at about 7 MHz. All the nearby strike records are from 1981.

The first two records are from the same lightning event, so the natural frequencies should agree. They do agree except for the damping on the 15.3 MHz resonance and for the frequency on the 21 MHz resonance. Neither of these resonances are as well excited in the D-dot record as they are in B-dot, so the B-dot results are the most reliable. This is supported by the fact that the 21 MHz resonance in B-dot agrees with all previous in-flight results.

ORIGINAL PAGE IS  
OF POOR QUALITY

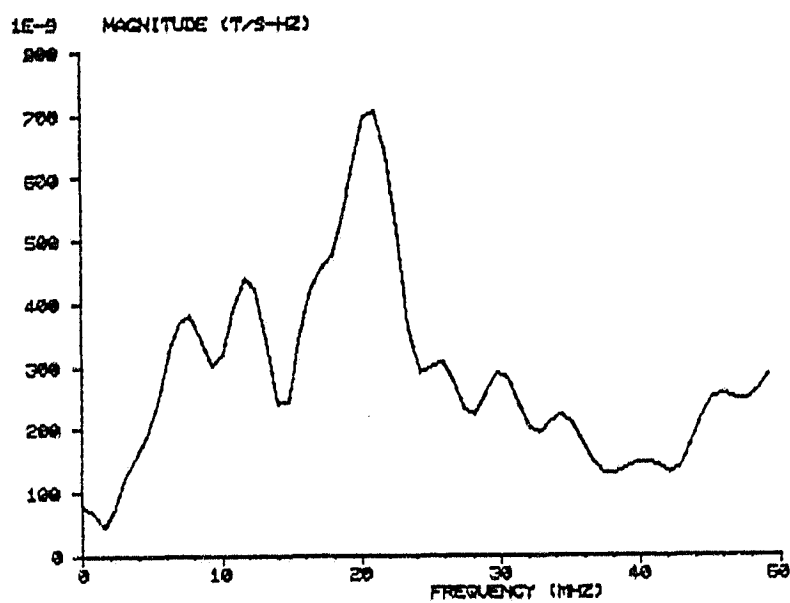
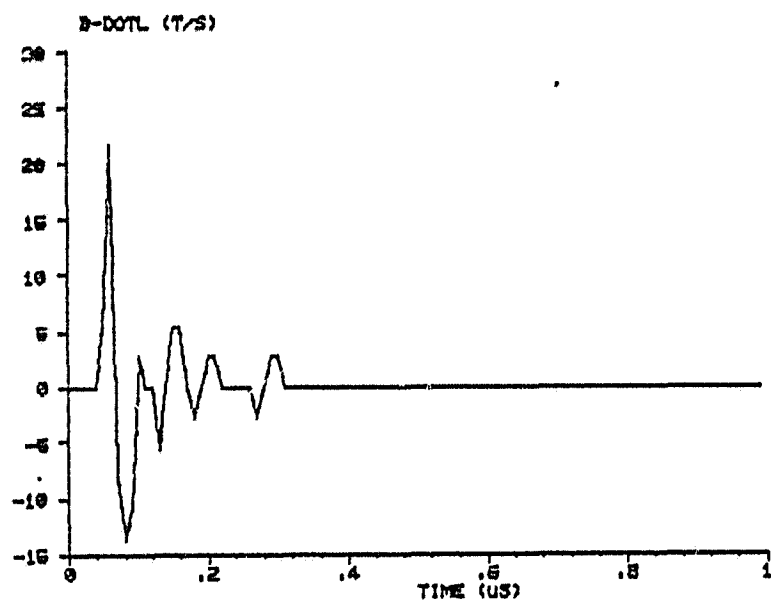


Figure 6.8. B-dot record from nearby strike 91-026-10.

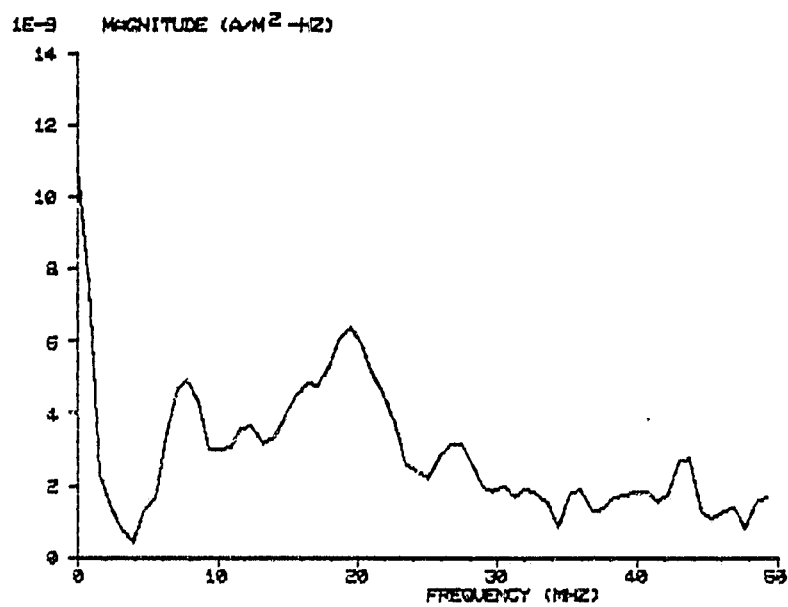
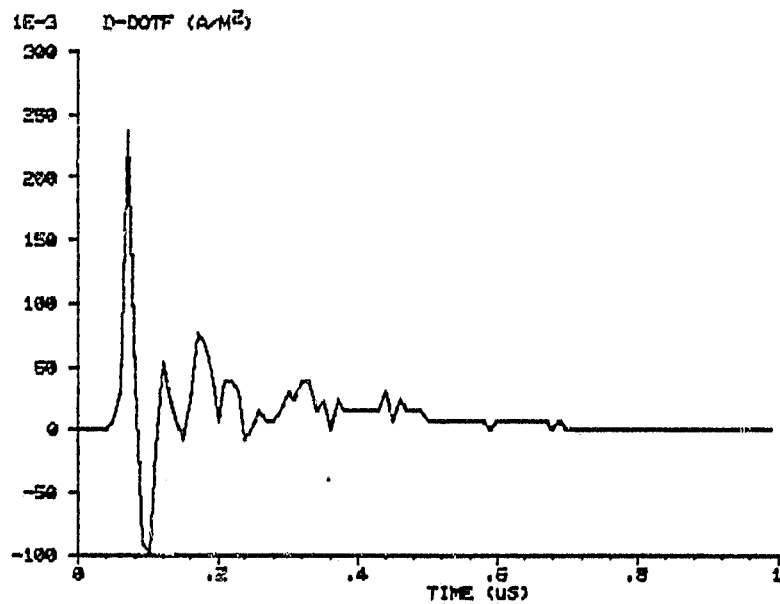


Figure 6.9. D-dot record from nearby strike 81-026-10.

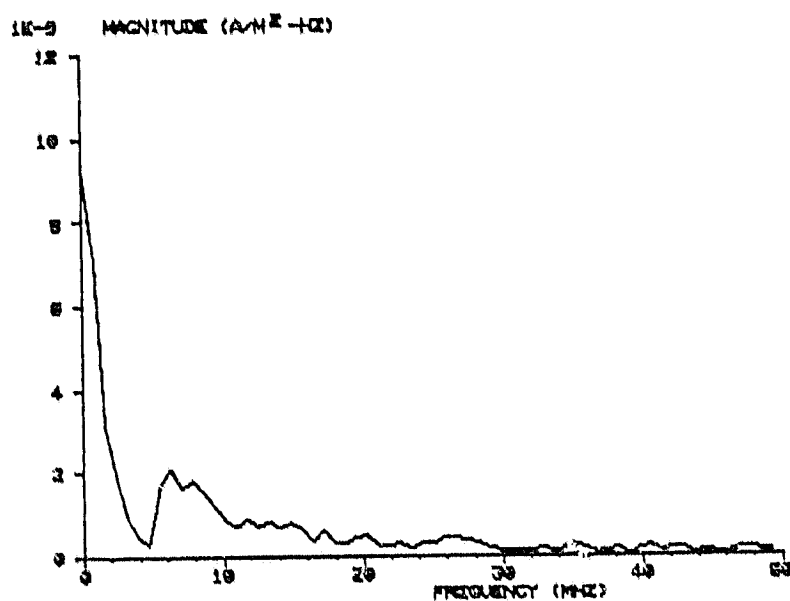
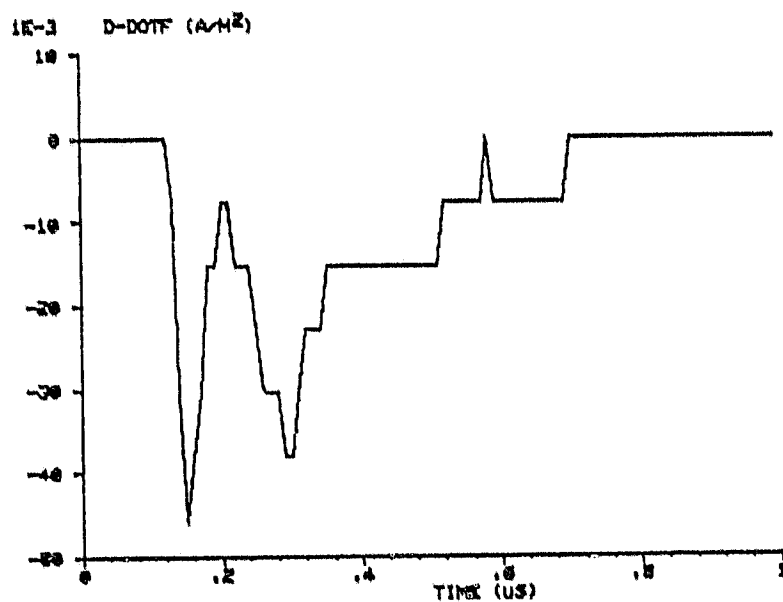


Figure 6.10. D-dot record from nearby strike  
81-026-03.

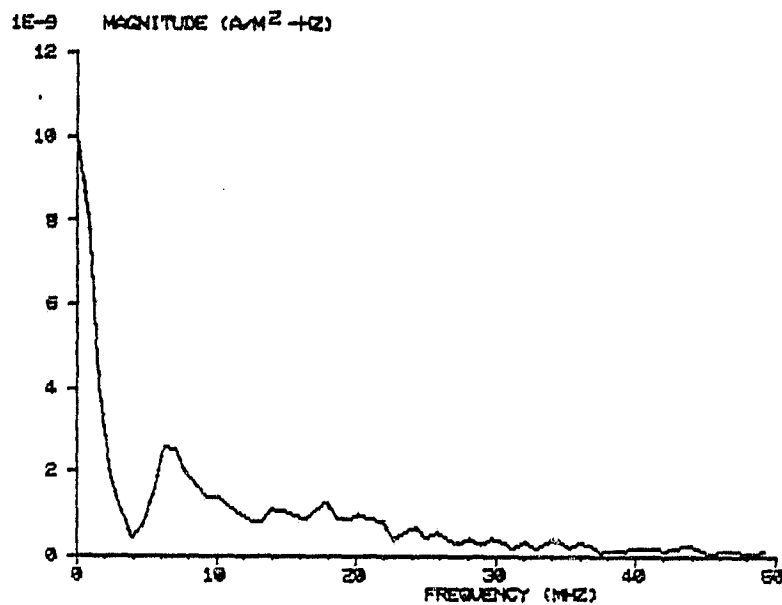
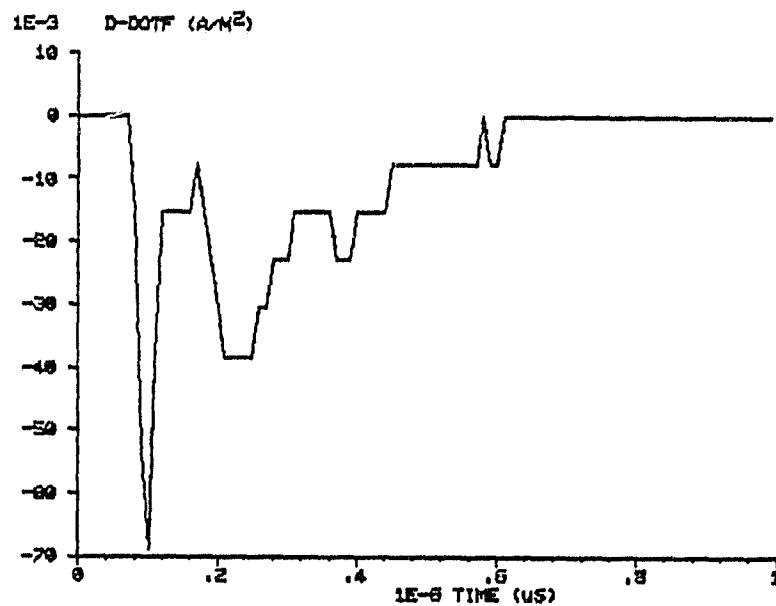


Figure 6.11. D-dot record from nearby strike  
81-026-07.



Of greater interest are the results from Prony analysis since the damping for each resonance should be at its minimum value. These results are listed in Table 6.3. The dampings of the resonances are indeed lighter than those obtained previously from either the model or direct-strike in-flight data, indicating that the dampings are representative of the isolated aircraft. The only exception is the unusual D-dot record from flight 18. This is an anomalous case which cannot be explained using these techniques. In regard to the natural frequencies extracted from records 81-026-03 and 07 it should be pointed out that, because of the coarse quantization inherent in these waveforms, the Prony analysis is somewhat approximate. The RMS error between the waveforms and their Prony reconstructions ranged up to 20%, so there is some uncertainty in the values of the natural frequencies.

The heaviest damping of the resonances should occur on the model, since it has fairly large, highly conducting wires. This does occur except for the first and third natural frequencies from B-dot record 38-3B. Perhaps multiple channels caused the high damping in this case.

The natural frequencies from flight 38 direct-strikes and from nearby-strikes are plotted in the scaled complex plane in Figure 6.12. Also shown are the results from model configuration 2 since it is most similar to the actual attachment configuration for these strikes. The third natural frequency from the nearby-strike records is not shown since there is no corresponding frequency in the direct-strike results. The natural frequencies from the lone D-dot record

TABLE 6.3. F-106B NATURAL FREQUENCIES FROM NEARBY LIGHTNING STRIKES

B-dot 26-10	
Natural frequency	f, MHz
$-.19 + j0.84$	7.4
$-.16 + j1.35$	11.8
$-.13 + j1.76$	15.4
$-.21 + j2.41$	21.1

D-dot 26-3	
Natural frequency	f, MHz
$-.14 + j0.79$	6.9

D-dot 26-10	
Natural frequency	f, MHz
$-.14 + j0.84$	7.3
$-.15 + j1.36$	11.9
$-.24 + j1.76$	15.3
$-.17 + j2.19$	19.1

D-dot 26-7	
Natural frequency	f, MHz
$-.16 + j0.71$	6.2

ORIGINAL PAGE IS  
OF POOR QUALITY

□	80-038-01, 80-038-05
Δ	80-038-03A
◇	80-038-03B
+	80-038-04
	D-dot
▽	80-038-04

• In-flight Nearby  
(average)  
X Model Configura-  
tion 2

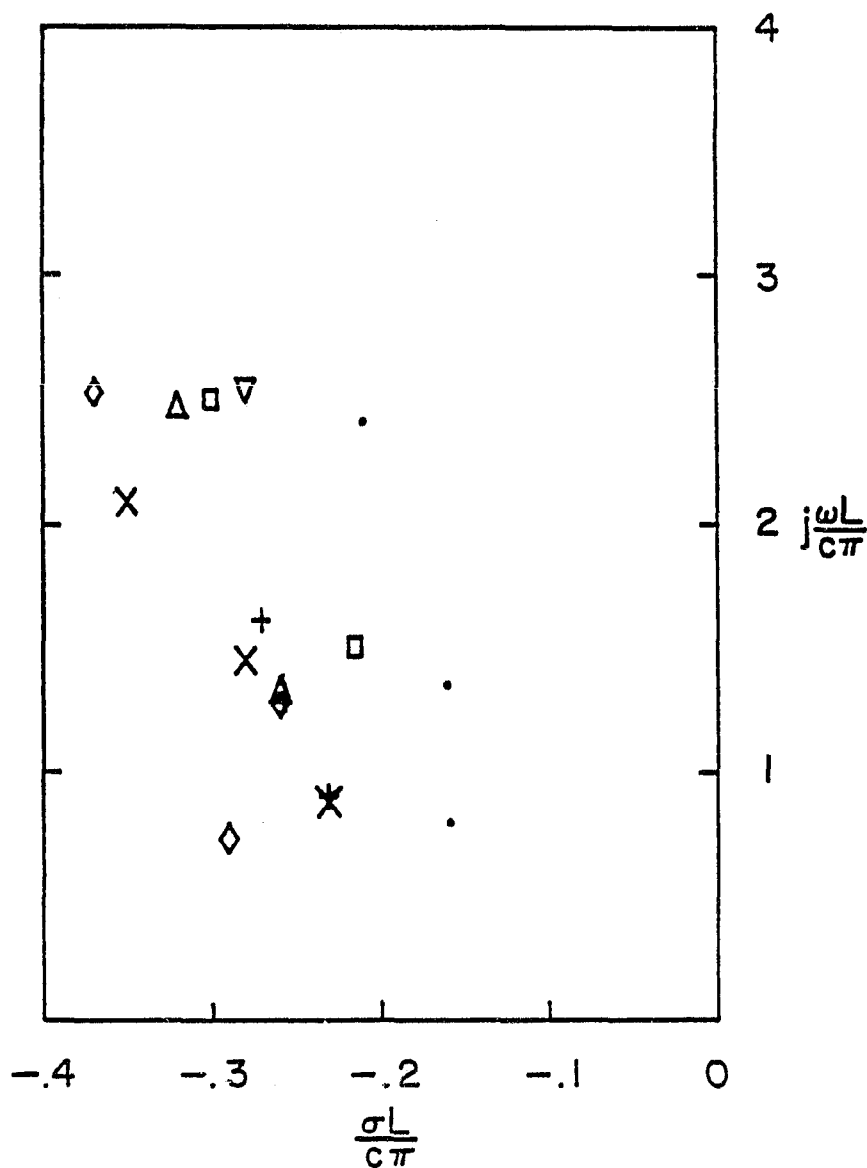


Figure 6.12. F-106B natural frequencies.

from flight 18 are plotted in Figure 6.13 along with model configuration 3 since it was the only one which showed a 16 MHz resonance.

The general tendency is for the in-flight results to show lighter damping than the model. This indicates that possibly the streamer theory discussed earlier is true, meaning that the aircraft is almost isolated. Another possibility is that a second attachment point, or a detachment point, has not occurred since the leader probably travels only a few cm in the time of most events, about 1  $\mu$ s. Therefore, only one attachment is present and the resonances are more lightly damped than expected. A third possibility is that the channel, being lossy, is inducing higher Q in the resonances since the current cannot flow off the aircraft as readily as on the highly conducting wires on the model.

ORIGINAL PAGE IS  
OF POOR QUALITY

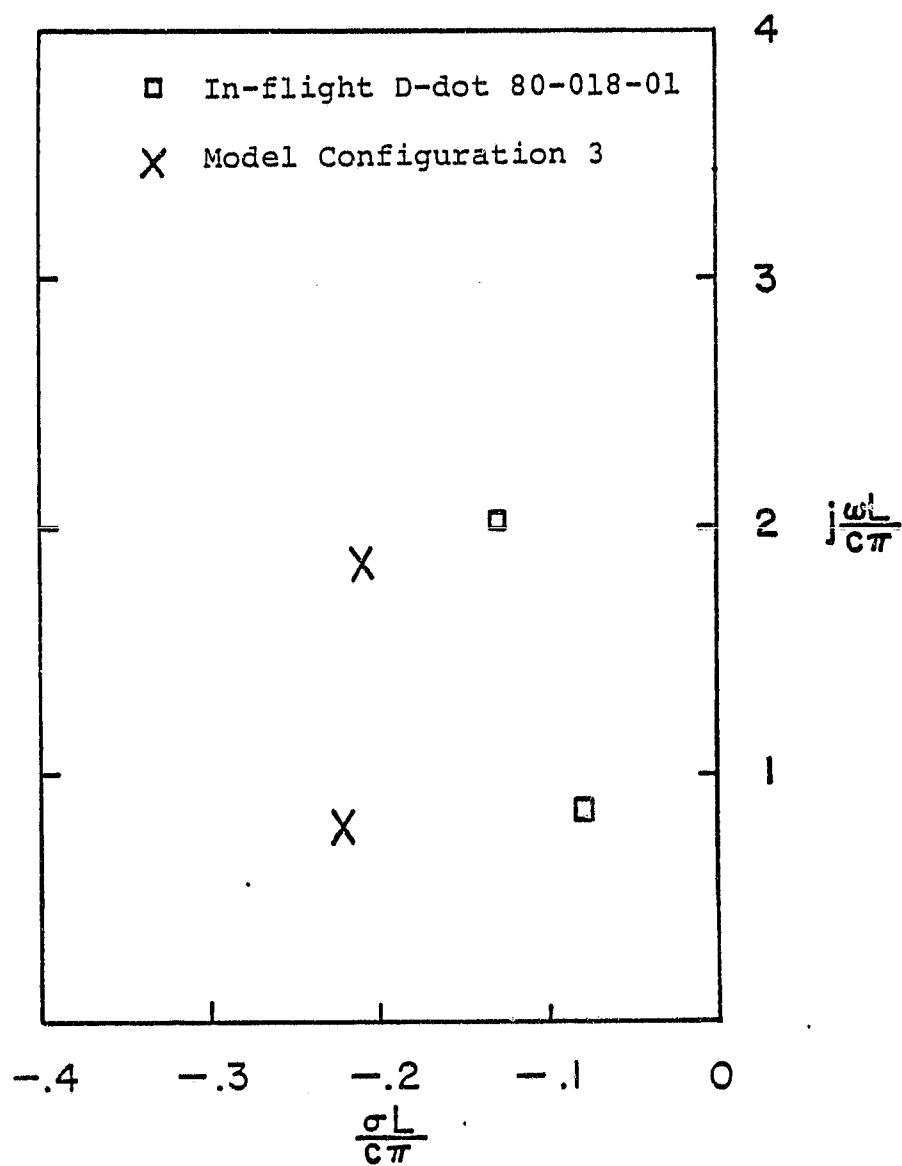


Figure 6.13. F-106B natural frequencies.

CHAPTER VII

CONCLUSIONS

The laboratory modeling and analysis techniques described in this report constitute a high signal-to-noise ratio method for studying the external response of an aircraft to injected current pulses. This has been shown to be a useful approach to modeling direct lightning strikes to the aircraft. The idea is not to try to duplicate in the laboratory the waveforms observed in a direct strike, but rather to determine the resonances or natural frequencies of both the laboratory and in-flight waveforms and then to use the comparison between them to help in the interpretation of the in-flight results.

As an initial test of the method, application to circular cylinders has provided new information on the effect of wire attachments on scatterers as compared to their isolated behavior. The wires cause the damping of each resonance to increase since they remove energy from the cylinder, adding to that removed by radiation. They also increase the frequencies of the resonances slightly since they make the cylinder electrically shorter.

Using the F-106B aircraft model, good agreement has been seen in comparisons with the rather limited amount of in-flight data that is available. Resonances excited by direct and nearby lightning strikes are substantially the same as those

on the model. However, detailed comparisons of model natural frequencies with those computed for direct-strike data almost always show higher  $Q$  in the in-flight case. This is indicative of either a lightning channel with a higher impedance than the wires on the model, only one channel attachment point, or short streamers instead of a long channel. More in-flight data may help to sort this out. For the nearby strike data, where the aircraft is isolated, the  $Q$  is the highest (except for one anomalous case). The average damping for the lowest resonance is  $-0.16$  as compared to  $-0.24$  for the model with its highly conducting wires. The value of  $-0.16$  for the isolated aircraft is comparable to that of an isolated cylinder with  $D/L = 0.17$  but is somewhat higher than typical stick model results for various aircraft [25]. Quantization errors limit the accuracy of the Prony analysis on the in-flight data.

Twelve waveforms were recorded on the model under short-pulse excitation conditions for the determination of the natural frequencies. (See figures 5.9, 5.10, 5.13, and 5.16) Four different wire attachment configurations were used. The waveforms contain information on characteristics to be expected on the airplane such as the ratios of  $E$  to  $H$  and of one component of  $H$  to the other. The natural frequencies extracted from these waveforms constitute a set of basic parameters for comparison with future in-flight data. (See Table 5.3.)

One area which might be addressed in future research is that of achieving a closer approximation to the lightning channel by modifying the wires on the model. This would involve using wires of smaller diameter and/or higher resistance and observing whether the natural frequencies of the model could be brought into agreement with those in-flight.

If the present modeling technique were applied to other types of aircraft, one would expect generally similar results. The similarity would probably be strongest for other aircraft which have the delta-wing shape of the F-106B. These include the shuttle, the F-16XL, various foreign-made aircraft, and several variable-wing aircraft such as the B-1 which are similar to a delta-wing when their wings are in the swept position. One would expect in the case of an aircraft containing large amounts of composite materials that the resonances would be more highly damped due to the lower electrical conductivity.

ORIGINAL PAGE IS  
OF POOR QUALITY



ORIGINAL PAGE IS  
OF POOR QUALITY

LIST OF REFERENCES

- [1] USNC/URSI National Radio Science Meeting Abstracts, Jan. 1982, National Acad. Sci., Washington, D.C.
- [2] J. M. Butler, et al., "Theoretical and Experimental Investigations of Thin-Wire Structures: Junction Conditions, Currents, and Charges," EMP Interaction Note 238, Air Force Weapons Lab, Kirtland AFB, NM, (February 1975).
- [3] F. J. Deadrick, "Transient Electromagnetic Measurements of a Brass Ship Model," Lawrence Livermore Laboratory Report UCRL-52454, (April 1978).
- [4] H. S. Cabayan, et al., "Surface Field Measurements on Scale Models in the Time Domain," EMP Interaction Note 410, Air Force Weapons Lab, Kirtland AFB, NM, (February 1981).
- [5] S. M. Kay and S. L. Marple, Jr., "Spectrum Analysis-A Modern Perspective," Proc. IEEE, Vol. 69, (11), 1380-1419 (November 1981).
- [6] M. L. Van Blaricum and R. Mittra, "A Technique for Extracting the Poles and Residues of a System Directly from Its Transient Response," IEEE Transactions on Antennas and Propagation AP-23, p. 777 (November 1977).
- [7] A. J. Poggio et al., "Evaluation of a Processing Technique for Transient Data," IEEE Transactions on Antennas and Propagation AP-26, p. 165 (January 1978).
- [8] M. L. Van Blaricum and R. Mittra, "Problems and Solutions Associated with Prony's Method for Processing Transient Data," IEEE Transactions on Antennas and Propagation AP-26, p. 174 (January 1978).
- [9] H. G. Hudson and D. L. Lager, "Observations on the Operation of the SEMPEX Code," Lawrence Livermore Laboratory Report UCID-17440, pp. 11-30 (1976).
- [10] E. K. Miller, "Data Characterization and Compression," Lawrence Livermore Laboratory Report UCID-17511, p. 15 (1977).
- [11] A. J. Poggio, "PARET: A Parameter Estimation Technique for Physical Applications," Energy and Technology Review, Lawrence Livermore Laboratory, pp. 24-30.
- [12] L. B. Felsen, ed., Transient Electromagnetic Fields, (New York, Heidelberg, Berlin: Springer-Verlag, 1976), pp. 129-179.

- [13] T. F. Trost and C. D. Turner, "Transient Electromagnetic Fields on a Delta-Wing Aircraft Model with Injected Currents," Proc. International Aerospace Conference on Lightning and Static Electricity, pp. D5-0--D5-7 (March 1982).
- [14] T. F. Trost and F. L. Pitts, "Analysis of Electromagnetic Fields on an F-106B Aircraft During Lightning Strikes," Proc. International Aerospace Conference on Lightning and Static Electricity, pp. D5-8--D5-15 (March 1982).
- [15] F. L. Pitts and M. E. Thomas, "1981 Direct Strike Lightning Data," NASA Technical Memorandum 83273 (March 1982).
- [16] F. L. Pitts, "Electromagnetic Measurement of Lightning Strikes to Aircraft," AIAA Journal of Aircraft, Vol. 19, (3), p. 246, (March 1982).
- [17] R. A. Perala and T. H. Rudolph, "The Interaction of Electromagnetic Fields with Aircraft During a Lightning Event," Proc. International Aerospace Conference on Lightning and Static Electricity, pp. C3-0--C3-13 (March 1982).
- [18] T. H. Rudolph and R. A. Perala, "Interpretation Methodology and Analysis of In-flight Lightning Data," Electro Magnetic Applications, Inc. Report EMA-82-R-21 (March 1982).
- [19] Fortran/RT-11 Extensions Manual, Digital Equipment Corporation No. AA-2124D-TC (October 1977).
- [20] C. D. Turner, "Laboratory Modeling and Analysis of Aircraft-Lightning Interactions," Ph.D. dissertation, August, 1982, Texas Tech University.
- [21] A. E. Knowlton, ed., Standard Handbook for Electrical Engineers, (New York: McGraw-Hill, 1949), p. 2-79.
- [22] S. A. Schelkunoff and H. T. Friis, Antennas Theory and Practice, (London: Wiley, 1952), pp. 104-106.
- [23] R. E. Matlick, Transmission Lines for Digital and Communications Networks, (New York: McGraw-Hill, 1969), p. 192.
- [24] RT-11 Fortran Scientific Subroutines Package Reference Manual, Digital Equipment Corporation No. DEC-11-ARSMA-A-D (1975).
- [25] G. Bedrosian, "Stick-Model Characterization of the Natural Frequencies and Natural Modes of the Aircraft," EMP Interaction Note 326, Air Force Weapons Lab, Kirtland AFB, NM, (1977).

- [27] K. S. H. Lee, EMP Interaction: Principles, Techniques, and Reference Data Air Force Weapons Laboratory Report AFWL-TR-80-402 (1980).
- [28] D. L. Moffatt and R. K. Mains, "Detection and Discrimination of Radar Targets," IEEE Transactions on Antennas and Propagation AP-23, (3), pp. 358-367 (May 1975).
- [29] C. W. Chuang and D. L. Moffatt, "Natural Resonances of Radar Targets Via Prony's Method and Target Discrimination," IEEE Transactions on Aerospace and Electronic Systems AES-12, (5), pp. 583-589 (September 1976).

APPENDIX I  
LISTING OF DATA ACQUISITION CODE

```

C      ***** DATA ACQUISITION CODE *****
C
C      DIMENSION IDATAA(512),IDATAB(512),IDATAC(512),IDATAD(512),
X      IDATAE(512),IDATAF(512),IDATAG(512),IDATAH(512),
X      IDATAI(512),IDATAJ(512),IDATAK(512),RDATA(512),A(3)
      BYTE NAME(16)
      RLSB=4.8828E-3
      CALL DATE(A)
      GO TO 60
50     TYPE 200
      ACCEPT 510,L
      IF(L.EQ.0)GO TO 900
60     TYPE 300
      ACCEPT 310,NAME
      TYPE 400
      ACCEPT 410,NSAMPL
      TYPE 500
      ACCEPT 510,IFIRST
      TYPE 710
      ACCEPT 410,IDIV
      IF(IDIV.EQ.200)SGAIN=1.02
      IF(IDIV.EQ.100)SGAIN=2.08
      IF(IDIV.EQ.50)SGAIN=4.1
      IF(IDIV.EQ.20)SGAIN=10.2
      IF(IDIV.EQ.10)SGAIN=20.25
      IF(IDIV.EQ.5)SGAIN=41.0
      IF(IFIRST.EQ.0.OR.IFIRST.EQ.1)GAIN=10.34*SGAIN
      IF(IFIRST.EQ.2.OR.IFIRST.EQ.3)GAIN=10.08*SGAIN
      IF(IFIRST.EQ.4)GAIN=2.01*SGAIN
      IF(IFIRST.EQ.5)GAIN=2.01*SGAIN
      IF(IFIRST.EQ.6)GAIN=108.8*SGAIN
      IF(IFIRST.EQ.7)GAIN=105.5*SGAIN
C      TYPE 600
C      ACCEPT 510,NCHANN

```

ORIGINAL PAGE IS  
OF POOR QUALITY.

```

C      TYPE 700
C      ACCEPT 410,IMODE
      NCHANN=1
      IMODE=0
      COR=RLSB/GAIN
      INC=1
      DO 5 I=1,512
      IDATAA(I)=0
      IDATAB(I)=0
      IDATAC(I)=0
      IDATAD(I)=0
      IDATAE(I)=0
      IDATAF(I)=0
      IDATAG(I)=0
      IDATAH(I)=0
      IDATAI(I)=0
      IDATAJ(I)=0
      IDATAK(I)=0
5      RDATA(I)=0.
      TYPE 850
      ACCEPT 860,SWTIM
      TYPE 870
      ACCEPT 860,SWLEN
      RATE=(40.*SWLEN)/SWTIM
      RCONT=1.E6/RATE
      ICOUNT=INT(RCONT)
      RCOUNT=FLOAT(ICOUNT)
      IF((RCOUNT-ICOUNT).GE.0.5)RCOUNT=RCOUNT+1.
      RATEAC=1.E6/RCOUNT
      SINT=2000./((RATEAC*SWTIM)/SWLEN)
      TYPE 890,RCOUNT,RATE,RATEAC,SINT
      IFLG=0
      IFLG1=0
      CALL RTS(IDATAA,512,,NSAMPL,IFIRST,NCHANN,,IMODE,IFLG,IDUM)
      CALL SETR(1,13,RCOUNT,IFLG1)

```

ORIGINAL PAGE IS  
OF POOR QUALITY

```

CALL LWAIT(IFLG,0)
CALL SETR(-1,,)
IFLG=0
CALL RTS(IDATAB,512,,NSAMPL,IFIRST,NCHANN,,IMODE,IFLG,IDUM)
CALL SETR(1,13,RCOUNT,IFLG1)
CALL LWAIT(IFLG,0)
CALL SETR(-1,,)
IFLG=0
CALL RTS(IDATAC,512,,NSAMPL,IFIRST,NCHANN,,IMODE,IFLG,IDUM)
CALL SETR(1,13,RCOUNT,IFLG1)
CALL LWAIT(IFLG,0)
CALL SETR(-1,,)
IFLG=0
CALL RTS(IDATAD,512,,NSAMPL,IFIRST,NCHANN,,IMODE,IFLG,IDUM)
CALL SETR(1,13,RCOUNT,IFLG1)
CALL LWAIT(IFLG,0)
CALL SETR(-1,,)
IFLG=0
CALL RTS(IDATAE,512,,NSAMPL,IFIRST,NCHANN,,IMODE,IFLG,IDUM)
CALL SETR(1,13,RCOUNT,IFLG1)
CALL LWAIT(IFLG,0)
CALL SETR(-1,,)
IFLG=0
CALL RTS(IDATAF,512,,NSAMPL,IFIRST,NCHANN,,IMODE,IFLG,IDUM)
CALL SETR(1,13,RCOUNT,IFLG1)
CALL LWAIT(IFLG,0)
CALL SETR(-1,,)
IFLG=0
CALL RTS(IDATAG,512,,NSAMPL,IFIRST,NCHANN,,IMODE,IFLG,IDUM)
CALL SETR(1,13,RCOUNT,IFLG1)
CALL LWAIT(IFLG,0)
CALL SETR(-1,,)
IFLG=0
CALL RTS(IDATAH,512,,NSAMPL,IFIRST,NCHANN,,IMODE,IFLG,IDUM)
CALL SETR(1,13,RCOUNT,IFLG1)

```

ORIGINAL PAGE IS  
OF POOR QUALITY

```

CALL LWAIT(IFLG,0)
CALL SETR(-1,,)
IFLG=0
CALL RTS(IDATAI,512,,NSAMPL,IFIRST,NCHANN,,IMODE,IFLG,IDUM)
CALL SETR(1,13,RCOUNT,JFLG1)
CALL LWAIT(IFLG,0)
CALL SETR(-1,,)
IFLG=0
CALL RTS(IDATAJ,512,,NSAMPL,IFIRST,NCHANN,,IMODE,IFLG,IDUM)
CALL SETR(1,13,RCOUNT,JFLG1)
CALL LWAIT(IFLG,0)
CALL SETR(-1,,)
IFLG=0
CALL RTS(IDATAK,512,,NSAMPL,IFIRST,NCHANN,,IMODE,IFLG,IDUM)
CALL SETR(1,13,RCOUNT,JFLG1)
CALL LWAIT(IFLG,0)
CALL SETR(-1,,)
DO 10 I=1,NSAMPL
RDATA(I)=IDATAB(I)+IDATAC(I)+IDATAD(I)+IDATAE(I)+IDATAF(I)
10 X RDATA(J)=RDATA(I)+IDATAG(I)+IDATAH(I)+IDATAI(I)+IDATAJ(I)
    +IDATAK(I)
DO 12 I=1,NSAMPL
12 RDATA(I)=((RDATA(I)/10.)-2048.)*COR
    TYPE 320,NAME
    TYPE 330,A
DO 15 I=1,NSAMPL,5
15 TYPE 20,RDATA(I),RDATA(I+1),RDATA(I+2),RDATA(I+3),RDATA(I+4)
    OPEN(UNIT=2,NAME=NAME,TYPE='UNKNOWN',RECORDSIZE=1,
X ACCESS='DIRECT',ASSOCIATEVARIABLE=INC)
DO 17 J=1,512
17 WRITE(2'JNC) RDATA(I)
    CLOSE(UNIT=2,DISPOSE='SAVE')
GO TO 50
20 FORMAT(1X,5E12.4)
200 FORMAT(1X,'SAMPLE ANOTHER WAVEFORM?'/1X,'TYPE 1 IF Y,0 IF N: ',*)

```

ORIGINAL PAGE IS  
OF POOR QUALITY



```

300  FORMAT(1X,'ENTER FILE NAME,AS "DY0:XXXXXX.XXX"',,$)
310  FORMAT(16A1)
320  FORMAT(/26X,16A1)
330  FORMAT(27X,3A4)
400  FORMAT(1X,'TAKE HOW MANY SAMPLES?',$)
410  FORMAT(I5)
500  FORMAT(1X,'FIRST CHANNEL TO BE SAMPLED?',$)
510  FORMAT(I1)
600  FORMAT(1X,'HOW MANY CHANNELS TO BE SAMPLED?',$)
700  FORMAT(1X,'MODE?',$)
710  FORMAT(1X,'OSCILLOSCOPE MILLIVOLTS/DIV?',$)
850  FORMAT(1X,'SWEEP TIME?',$)
870  FORMAT(1X,'SWEEP LENGTH?',$)
880  FORMAT(F10.2)
890  FORMAT(/5X,'RCOUNT=',F10.2,/5X,'DESIRED SAMPLING RATE=',
X   F10.2,' Hz',5X,'ACTUAL SAMPLING RATE=',F10.2,' Hz'/
X   5X,'SAMPLING INTERVAL=',F10.5,' PS')
900  CALL EXIT
      END

```

ORIGINAL PAGE IS  
OF POOR QUALITY

ORIGINAL PAGE IS  
OF POOR QUALITY

APPENDIX II  
LISTING OF PRONY CODE

```

C*****
C
C          SINGULARITY EXPANSION
C
C          USING
C
C          PRONY'S METHOD
C
C          MAXIMUM OF 36 DEGREES OF FREEDOM
C
C*****
COMMON/DATA/RDATA(512)
COMMON/READ/TDATA(512)
COMMON/NDATA/AVDATA(72)
COMMON/PARA/N,NN,NS,NSHIF
COMMON/DAY/NAME,A
COMMON/PRO/DELTA,DELT
DIMENSION WW(37),ROOTRE(36),ROOTIM(36),ALMAT(36,36),ALPHA(37)
BYTE NAME(16),A(16)
CALL DATE(A)
TYPE 125
ACCEPT 310,NRESUM
IF(NRESUM.EQ.0)GO TO 1
TYPE 126
ACCEPT 310,NEWSFT
NEWSFT=NEWSFT+1
GO TO 60
1 TYPE 200
ACCEPT 210,NAME
TYPE 320
ACCEPT 330,DELT
C TYPE 325
C ACCEPT 310,NRECON
C TYPE 205
C ACCEPT 210,PNAME

```

ORIGINAL PAGE IS  
OF POOR QUALITY

```

C
C***** READ DATA FROM DISK *****
C
      CALL READ(NAME)
C
C***** INITIALIZATION *****
C
      2   NEWSFT=0
          NRESUM=0
          TYPE 220
          ACCEPT 310,N
          M=N+1
          NN=2*N
          TYPE 300
          ACCEPT 310,NS
          TYPE 340
          ACCEPT 350,DCLEV
          NSAMPL=NS*NN
          IF(NSAMPL.GT.432)GO TO 80
          DELTA=NS*DELT
C
C***** DO SHIFTING *****
C
          TYPE 100
          ACCEPT 310,NSHIF
      60   TYPE 150
          ACCEPT 310,NSHIFS
          TYPE 48,DELTA
      48   FORMAT(1X,'DELTA=',E15.5)
      62   NSHIFT=NSHIF-1+NEWSFT
          DO 70 J=1,NSHIFS
              CALL SETERR(10,11)
              NSHIFT=NSHIFT+1
          DO 10 I=1,452
      10   RDATA(I)=TDATA(I+NSHIFT)+DCLEV

```

ORIGINAL PAGE IS  
OF POOR QUALITY

```

C
C***** FORM REDUCED WAVEFORM *****
C***** ADD DC LEVEL IF REQUIRED *****
C
      TYPE 45,NSHIFT
45  FORMAT(/1X,'NSHIFT=',I5)
      DO 30 I=1,NN
      K=I-1
30  AVDATA(I)=RDATA(1+(K*NS))
C      TYPE 47
47  FORMAT(26X,'AVDATA')
C      DO 49 I=1,NN,5
C49  TYPE 50,AVDATA(I),AVDATA(I+1),AVDATA(I+2),AVDATA(I+3)
C      X,AVDATA(I+4)
50  FORMAT(1X,5E12.4)
C
C***** CALL PRONY SUBROUTINE *****
C
70  CALL PRONY(ALMAT,ALPHA,ROOTRE,ROOTIM,WW,N,M)
      GO TO 90
80  TYPE 700
90  TYPE 500
      ACCEPT 310,IOVER
      IF(IOVER.EQ.1)GO TO 2
      TYPE 600
      ACCEPT 310,IOVER
      IF(IOVER.EQ.1)GO TO 1
      GO TO 900
100 FORMAT(1X,'NUMBER OF POINTS TO SHIFT(+=SHIFT LEFT;-=SHIFT
X RIGHT)? ',I)
125 FORMAT(1X,'RESUME ON PREVIOUS WAVEFORM? ',I)
126 FORMAT(1X,'SHIFTS TO SKIP? ',I)
150 FORMAT(1X,'NUMBER OF SHIFTS? ',I)
200 FORMAT(1X,'ENTER DATA FILE NAME, AS "DYO:XXXXXX.XXX" ',I)
205 FORMAT(1X,'ENTER POLE FILE NAME, AS "DYO:XXXXXX.XXX" ',I)

```

ORIGINAL FILE NO.  
OF POOR QUALITY

```

210  FORMAT(16A1)
220  FORMAT(1X,'ORDER? ',,$)
300  FORMAT(1X,'TAKE EVERY ?th POINT? ',,$)
310  FORMAT(I5)
320  FORMAT(1X,'WAVEFORM SAMPLING INTERVAL? ',,$)
325  FORMAT(1X,'RECONSTRUCT AND COMPUTE RMS ERROR? ',,$)
330  FORMAT(E20.5)
340  FORMAT(1X,'DC LEVEL ADDED? ',,$)
350  FORMAT(F10.5)
500  FORMAT(1X,'ANOTHER EXPANSION ON SAME WAVEFORM? ',,$)
600  FORMAT(1X,'ANOTHER EXPANSION ON DIFFERENT WAVEFORM? ',,$)
700  FORMAT(1X,'REDUCED WAVEFORM EXTENDS TOO LONG IN TIME')
900  CALL EXIT
      END

```

```

      SUBROUTINE READ(NAME)
C***** ROUTINE TO READ DATA FROM DISK *****
      COMMON/READ/TDATA(512)
      INC=1
      OPEN(UNIT=2,NAME=NAME,TYPE='OLD',RECORDSIZE=1000,
XACCESS='DIRECT',ASSOCIATEVARIABLE=INC)
      READ(2'INC')(TDATA(I),I=1,512)
      CLOSE(UNIT=2,DISPOSE='SAVE')
      RETURN
      END

```

```

      SUBROUTINE PRONY(ALMA,ALPH,ROOTR,ROOTI,W,N,M)
      COMMON/PRO/DELTA,DELT
      COMMON/NDATA/AVDATA(72)
      DIMENSION ALMA(N,N),ALPH(M),ROOTR(N),ROOTI(N),W(M),POLEF(36)
      COMPLEX RESMAT(36,36),POLE(36),POLTP(36),RESIDU(36),CMPLX,CLOB
C
C***** SET UP THE ALPHA MATRIX *****
C
      DO 10 I=1,N

```

ORIGINAL PAGE IS  
OF POOR QUALITY

```

      K=I-1
      ALPH(I)=-AVDATA(I+N)
      DO 10 J=1,N
10    ALMA(I,J)=AVDATA(J+K)
C
C***** SOLVE FOR THE ALPHAS *****
C
      CALL SIMQ(ALMA,ALPH,N,KS)
      IF(KS.EQ.0)GO TO 30
      TYPE 65
      GO TO 100
30    ALPH(N+1)=1.0
C
C***** SOLVE FOR POLES AS ZEROS OF Nth ORDER POLYNOMIAL *****
C
      CALL POLRT(ALPH,W,N,ROOTR,ROOTI,IER)
      IF(IER.EQ.0)GO TO 40
      TYPE 67,IER
      GO TO 100
40    DO 22 I=1,N
      POLE(I)=CMPLX(ROOTR(I),ROOTI(I))
22    POLE(I)=(1./DELTA)*CLOG(POLE(I))
C
C***** LOOK FOR POLES WITH POSITIVE REAL PARTS *****
C***** REMOVE WHEN FOUND *****
C
      L=0
      DO 24 I=1,N
      IF(REAL(POLE(I)).GT.0.)GO TO 23
      L=L+1
      GO TO 24
23    POLE(I)=(0.,0.)
24    CONTINUE
C
C*** COMPUTE RESIDUES USING ONLY POLES WITH NEGATIVE REAL PARTS ***

```

ORIGINAL PAGE IS  
OF POOR QUALITY

```

C      CALL MATRD(RESMAT,POLE,RESIDU,POLEF,POLTP,L)
65     FORMAT(1X,'ALPHA MATRIX IS SINGULAR!')
67     FORMAT(1X,'ERROR IN SUBROUTINE POLRT!',5X,'IER=',I5)
100    RETURN
      END

      SUBROUTINE MATRD(RESM,POLE,RESI,POLF,POLT,L)
C
C***** ROUTINE TO SETUP MATRIX AND VECTOR FOR COMPUTATION OF
C      RESIDUES, AND TO PRINT OUTPUT *****
      COMMON/DATA/RDATA(512)
      COMMON/PARA/N,NN,NS,NSHIF
      COMMON/DAY/NAME,A
      COMMON/PRO/DELTA,DELT
      DIMENSION RES(36),POLF(L),RCDATA(512)
      COMPLEX RESM(L,L),POLE(36),RESI(L),POLT(L),CEXP,CMLPX
      BYTE NAME(16),A(16)
      II=1
      DO 30 I=1,N
      IF(POLE(I).EQ.(0.,0.))GO TO 30
      POLT(II)=POLE(I)
      II=II+1
30     CONTINUE
      DO 10 J=1,L
      K=I-1
      RES(I)=RDATA(1+(K*NS))
      DO 10 J=1,L
10     RESM(I,J)=CEXP(POLT(J)*DELTA*K)
      DO 40 I=1,L
40     RESI(I)=CMLPX(RES(I),0.0)
C
C***** COMPUTE RESIDUES *****
C
      CALL SIMQC(RESM,RESI,L,KS)

```

GROUP 1, PAGE 15  
 OF POOR QUALITY



```

        IF(KS.EQ.0)GO TO 70
        TYPE 69
69      FORMAT(1X,'RESIDUE MATRIX IS SINGULAR!')
        GO TO 500
C
C***** PRINT RESULTS *****
C
70      TYPE 100,NAME
        TYPE 110,A
        TYPE 400
        DO 80 I=1,L
C      IF(AIMAG(POLT(I)).LT.0)GO TO 80
        TYPE 410,POLT(I),RESI(I)
80      CONTINUE
        TYPE 412
        IF(DELT.EQ.50.E-12.OR.DELT.EQ.100.E-12)GO TO 82
        SCALF=1.82399E-8
        FREQ=1.591549E-7
        GO TO 84
82      SCALE=9.70209E-10
        FREQ=8.465688E-9
84      DO 90 I=1,L
        IF(AIMAG(POLT(I)).LT.0)GO TO 90
        POLF(I)=AIMAG(POLT(I))*FREQ
        POLT(I)=POLT(I)*SCALE
        RESMAG=CABS(RESI(I))
        TYPE 411,POLT(I),POLF(I),RESMAG
90      CONTINUE
C
C***** RECONSTRUCT WAVEFORM *****
C
C      IF(NRCON.EQ.0) GO TO 500
        DO 190 I=1,512
190     RCDATA(I)=0.0
        DO 200 I=1,L

```

ORIGINAL PAGE IS  
OF POOR QUALITY

```

200  POLT(I)=POLT(I)/SCALE
      DO 250 I=1,L
      IF(AIMAG(POLT(I)).LT.0)GO TO 250
      IF(AIMAG(POLT(I)).EQ.0)RESI(I)=CMPLX(REAL(RESI(I))*0.5,
X    AIMAG(RESI(I)))
      IF(DELT.EQ.10.E-9)GO TO 210
      NREC=400-NSHIF
      GO TO 230
210  NREC=40
230  DO 300 J=1,NREC
      TIME=(J-1)*DELT
300  RCDATA(J)=RCDATA(J)+2*(EXP(REAL(POLT(I))*TIME))*
X    (REAL(RESI(I))*COS(AIMAG(POLT(I))*TIME)-
X    AIMAG(RESI(I))*SIN(AIMAG(POLT(I))*TIME))
250  CONTINUE
C    DO 310 I=1,50,5
C310  TYPE 320,RCDATA(I),RCDATA(I+1),RCDATA(I+2),RCDATA(I+3),
C    XRCDATA(I+4)
320  FORMAT(1X,5E12.4)
C
C***** COMPUTE RMS ERROR *****
C
      RMSERR=0.
      RMSRSP=0.
      DO 350 I=1,NREC
      RMSERR=RMSERR+(RCDATA(I)-RDATA(I))**2
350  RMSRSP=RMSRSP+(RDATA(I))**2
      RMSERR=(SQRT(RMSERR/RMSRSP))*100.
      TYPE 420,NREC,RMSERR
100  FORMAT(26X,16A1)
110  FORMAT(27X,16A1)
400  FORMAT(20X,'POLES',35X,'RESIDUES')
410  FORMAT(1X,E15.5,5X,'+J',E15.5,5X,E15.5,5X,'+J',E15.5)
411  FORMAT(5X,F10.2,5X,'+J',F10.2,5X,F10.2,10X,E15.5)
412  FORMAT(15X,'SCALED POLES',10X,'FREQUENCY,MHZ',9X,'RESIDUE

```

CONFIDENTIAL  
 OF POLAR GROUND

```
XMAGNITUDE')  
420  FORMAT(/1X,'NREC=',I5,5X,'RMS ERROR=',E12.4,' %')  
500  RETURN  
      END)
```

ORIGINAL PAGE IS  
OF POOR QUALITY

SUBROUTINE SIMQ

## PURPOSE

OBTAIn SOLUTIOn OF A SET OF SIMULTANEous LINEAR EQUATIOnS,  
AX=B

## USAGE

```
CALL SIMQ(A,B,N,KS)
```

## DESCRIPTION OF PARAMETERS

A - MATRIX OF COEFFICIENTS STORED COLUMNWISE. THESE ARE DESTROYED IN THE COMPUTATION. THE SIZE OF MATRIX A IS N BY N.

B - VECTOR OF ORIGINAL CONSTANTS (LENGTH N). THESE ARE REPLACED BY FINAL SOLUTION VALUES, VECTOR X.

N - NUMBER OF EQUATIONS AND VARIABLES, N MUST BE .GT. ONE.

KS - OUTPUT DIGIT

## 6 FOR A NORMAL SOLUTION

# 1 FOR A SINGULAR SET OF EQUATIONS

REMARKS

MATRIX A MUST BE GENERAL.

IF MATRIX IS SINGULAR , SOLUTION VALUES ARE MEANINGLESS.  
AN ALTERNATIVE SOLUTION MAY BE OBTAINED BY USING MATRIX  
INVERSION (MJNV) AND MATRIX PRODUCT (GMPRD).

## SUBROUTINES AND FUNCTION SUBPROGRAMS REQUIRED

NONE

## METHOD

METHOD OF SOLUTION IS BY ELIMINATION USING LARGEST PIVOTAL DIVISOR. EACH STAGE OF ELIMINATION CONSISTS OF INTERCHANGING

# OF POOR QUALITY

```

C      ROWS WHEN NECESSARY TO AVOID DIVISION BY ZERO OR SMALL
C      ELEMENTS.
C      THE FORWARD SOLUTION TO OBTAIN VARIABLE N IS DONE IN
C      N STAGES. THE BACK SOLUTION FOR THE OTHER VARIABLES IS
C      CALCULATED BY SUCCESSIVE SUBSTITUTIONS. FINAL SOLUTION
C      VALUES ARE DEVELOPED IN VECTOR B, WITH VARIABLE 1 IN B(1),
C      VARIABLE 2 IN B(2),....., VARIABLE N IN B(N).
C      IF NO PIVOT CAN BE FOUND EXCEEDING A TOLERANCE OF 0.0,
C      THE MATRIX IS CONSIDERED SINGULAR AND KS IS SET TO 1. THIS
C      TOLERANCE CAN BE MODIFIED BY REPLACING THE FIRST STATEMENT.
C
C      .....
C
C      SUBROUTINE SIMQ(A,B,N,KS)
C      DIMENSION A(1),B(1)
C
C      FORWARD SOLUTION
C
C      TOL=0.0
C      KS=0
C      JJ=-N
C      DO 65 J=1,N
C      JY=J+1
C      JJ=JJ+N+1
C      BIGA=0
C      IT=JJ-J
C      DO 30 I=J,N
C
C      SEARCH FOR MAXIMUM COEFFICIENT IN COLUMN
C
C      IJ=JT+I
C      IF(ABS(BJGA)-ABS(A(IJ))) 20,30,30
C 20  BIGA=A(IJ)
C      IMAX=I
C 30  CONTINUE

```

ORIGINAL PAGE IS  
OF POOR QUALITY

```

C
C      TEST FOR PIVOT LESS THAN TOLERANCE (SINGULAR MATRIX)
C
      IF (ABS(BIGA)-TOL) 35,35,40
35  KS=1
      RETURN
C
C      INTERCHANGE ROWS IF NECESSARY
C
40  I1=J+N*(J-2)
      IT=IMAX-J
      DO 50 K=J,N
          I1=I1+N
          I2=I1+IT
          SAVE=A(I1)
          A(I1)=A(I2)
          A(I2)=SAVE
C
C      DIVIDE EQUATION BY LEADING COEFFICIENT
C
50  A(I1)=A(I1)/BIGA
      SAVE=B(IMAX)
      B(IMAX)=B(J)
      B(J)=SAVE/BIGA
C
C      ELIMINATE NEXT VARIABLE
C
      IF (J-N) 55,70,55
55  IQS=N*(J-1)
      DO 65 IX=JY,N
          IXJ=IQS+IX
          IT=J-IX
          DO 60 JX=JY,N
              IXJX=N*(JX-1)+IX
              JJX=IXJX+IT

```

ORIGINAL PAGE IS  
OF POOR QUALITY

```
60 A(IXJX)=A(IXJX)-(A(IXJ)*A(JJX))
65 B(IX)=B(IX)-(B(J)*A(IXJ))
```

C  
C  
C

# BACK SOLUTION

```
70 NY=N-1
   IT=N*N
   DO 80 J=1,NY
     IA=IT-J
     IB=N-J
     IC=N
     DO 80 K=1,J
       B(IB)=B(IB)-A(IA)*B(IC)
     IA=IA-N
80  IC=IC-1
   RETURN
   END
```

ORIGINAL PAGE IS  
OF POOR QUALITY

.....

SUBROUTINE SIMGC

## PURPOSE

# OBTAIN SOLUTION OF A SET OF SIMULTANEOUS LINEAR EQUATIONS, AX=B, WITH COMPLEX COEFFICIENTS

## USAGE

CALL SIMGC(A,B,N,KS)

## DESCRIPTION OF PARAMETERS

A - MATRIX OF COEFFICIENTS STORED COLUMNWISE. THESE ARE DESTROYED IN THE COMPUTATION. THE SIZE OF MATRIX A IS N BY N.

B - VECTOR OF ORIGINAL CONSTANTS (LENGTH N). THESE ARE REPLACED BY FINAL SOLUTION VALUES, VECTOR X.

N - NUMBER OF EQUATIONS AND VARIABLES. N MUST BE .GT. ONE.

KS - OUTPUT DIGIT

### 0 FOR A NORMAL SOLUTION

# 1 FOR A SINGULAR SET OF EQUATIONS

REMARKS

MATRIX A MUST BE GENERAL.

IF MATRIX IS SINGULAR , SOLUTION VALUES ARE MEANINGLESS.

AN ALTERNATIVE SOLUTION MAY BE OBTAINED BY USING MATRIX  
INVERSION (MINV) AND MATRIX PRODUCT (GMPRD).

### SUBROUTINES AND FUNCTION SUBPROGRAMS REQUIRED

NONE

## METHOD

METHOD OF SOLUTION IS BY ELIMINATION USING LARGEST PIVOTAL DIVISOR. EACH STAGE OF ELIMINATION CONSISTS OF INTERCHANGING

ORIGINAL PAGE IS  
OF POOR QUALITY



```

C      ROWS WHEN NECESSARY TO AVOID DIVISION BY ZERO OR SMALL
C      ELEMENTS.
C      THE FORWARD SOLUTION TO OBTAIN VARIABLE N IS DONE IN
C      N STAGES. THE BACK SOLUTION FOR THE OTHER VARIABLES IS
C      CALCULATED BY SUCCESSIVE SUBSTITUTIONS. FINAL SOLUTION
C      VALUES ARE DEVELOPED IN VECTOR B, WITH VARIABLE 1 IN B(1),
C      VARIABLE 2 IN B(2),....., VARIABLE N IN B(N).
C      IF NO PIVOT CAN BE FOUND EXCEEDING A TOLERANCE OF 0.0,
C      THE MATRIX IS CONSIDERED SINGULAR AND KS IS SET TO 1. THIS
C      TOLERANCE CAN BE MODIFIED BY REPLACING THE FIRST STATEMENT,

```

.....

```
SUBROUTINE SJMQC(A,B,N,KS)
COMPLEX A,B,BIGA,SAVE
DIMENSION A(1),B(1)
```

C  
C FORWARD SOLUTION  
C

```

TOL=0.0
KS=0
JJ=-N
DO 65 J=1,N
  JY=J+1
  JJ=JJ+N+1
  BIGA=0
  IT=JJ-J
  DO 30 I=J,N

```

```

C
C      SEARCH FOR MAXIMUM COEFFICIENT IN COLUMN
C

```

```

      1J=J+J
      IF (CABS(RJGA)-CABS(A(IJ))) 20,30,30
20  BIGA=A(IJ)
      IMAX=I

```

POOR QUALITY

```

30 CONTINUE
C
C      TEST FOR PIVOT LESS THAN TOLERANCE (SINGULAR MATRIX)
C
      IF (CABS(BIGA)-TOL) 35,35,40
35 KS=1
   RETURN
C
C      INTERCHANGE ROWS IF NECESSARY
C
40 I1=J+N*(J-2)
   IT=IMAX-J
   DO 50 K=J,N
     I1=I1+N
     I2=I1+IT
     SAVE=A(I1)
     A(I1)=A(I2)
     A(I2)=SAVE
C
C      DIVIDE EQUATION BY LEADING COEFFICIENT
C
50 A(I1)=A(I1)/BIGA
   SAVE=B(IMAX)
   B(IMAX)=B(J)
   B(J)=SAVE/BIGA
C
C      ELIMINATE NEXT VARIABLE
C
      IF (J-N) 55,70,55
55 IQS=N*(J-1)
   DO 65 IX=JY,N
     IXJ=IQS+IX
     IT=J-IX
     DO 60 JX=JY,N
       IXJX=N*(JX-1)+IX

```

ORIGINAL PAGE IS  
OF POOR QUALITY

```

      JJX=IXJX+IT
60  A(IXJX)=A(IXJX)-(A(IXJ)*A(JJX))
65  B(JX)=B(IX)-(B(J)*A(IXJ))
C
C      BACK SOLUTION
C
70  NY=N-1
      IT=N*N
      DO 80 J=1,NY
        IA=IT-J
        IB=N-J
        IC=N
        DO 80 K=1,J
          B(IB)=B(IB)-A(IA)*B(IC)
          IA=IA-N
80  IC=IC-1
      RETURN
      END

```

APPROVED FOR RELEASE  
 BY NSA/CSS/CSS/INT  
 DATE 08-01-2013



C  
C  
C  
C  
C  
C  
C  
C  
C

METHOD

NEWTON-RAPHSON ITERATIVE TECHNIQUE. THE FINAL ITERATIONS  
ON EACH ROOT ARE PERFORMED USING THE ORIGINAL POLYNOMIAL  
RATHER THAN THE REDUCED POLYNOMIAL TO AVOID ACCUMULATED  
ERRORS IN THE REDUCED POLYNOMIAL.

.....  
SUBROUTINE POLRT(XCOF,COF,M,ROOTR,ROOTI,IER)  
DIMENSION XCOF(1),COF(1),ROOTR(1),ROOTI(1)  
DOUBLE PRECISION XO,YO,X,Y,XPR,YPR,UX,UY,V,YT,XT,U,XT2,YT2,SUMSQ,  
1 DX,DY,TEMP,ALPHA,DABS

C  
C  
C  
C  
C  
C  
C  
C  
C  
C  
C  
C  
C  
C  
C  
C

.....  
IF A DOUBLE PRECISION VERSION OF THIS ROUTINE IS DESIRED, THE  
C IN COLUMN 1 SHOULD BE REMOVED FROM THE DOUBLE PRECISION  
STATEMENT WHICH FOLLOWS.

DOUBLE PRECISION XCOF,COF,ROOTR,ROOTI

THE C MUST ALSO BE REMOVED FROM DOUBLE PRECISION STATEMENTS  
APPEARING IN OTHER ROUTINES USED IN CONJUNCTION WITH THIS  
ROUTINE.

THE DOUBLE PRECISION VERSION MAY BE MODIFIED BY CHANGING THE  
CONSTANT IN STATEMENT 78 TO 1.0D-12 AND IN STATEMENT 122 TO  
1.0D-10. THIS WILL PROVIDE HIGHER PRECISION RESULTS AT THE  
COST OF EXECUTION TIME

.....  
IFJT=0  
N=M  
IER=0

ORIGINAL FILE IS  
OF POOR QUALITY

```

      IF(XCOF(N+1))10,25,10
10  IF(N) 15,15,32
C
C      SET ERROR CODE TO 1
C
      15 IER=1
      20 RETURN
C
C      SET ERROR CODE TO 4
C
      25 IER=4
      GO TO 20
C
C      SET ERROR CODE TO 2
C
      30 IER=2
      GO TO 20
      32 IF(N-36) 35,35,30
      35 NX=N
         NXN=N+1
         N2=1
         KJ1 = N+1
         DO 40 L=1,KJ1
            MT=KJ1-L+1
      40 COF(MT)=XCOF(L)
C
C      SET INITIAL VALUES
C
      45 X0=.00500101
         Y0=0.01000101
C
C      ZERO INITIAL VALUE COUNTER
C
      IN=0
      50 X=XI

```

ORIGINAL PAGE IS  
OF POOR QUALITY

C  
C            INCREMENT INITIAL VALUES AND COUNTER  
C

X0=-10.0\*Y0  
Y0=-10.0\*X

C  
C            SET X AND Y TO CURRENT VALUE  
C

X=X0  
Y=Y0  
IN=IN+1  
GO TO 59  
55 IFIT=1  
XPR=X  
YPR=Y

C  
C            EVALUATE POLYNOMIAL AND DERIVATIVES  
C

59 ICT=0  
60 UX=0.0  
UY=0.0  
V =0.0  
YT=0.0  
XT=1.0  
U=COF(N+1)  
IF(U) 65,130,65  
65 DO 70 I=1,N  
L =N-I+1  
TEMP=COF(L)  
XT2=X\*XT-Y\*YT  
YT2=X\*YT+Y\*XT  
U=U+TEMP\*XT2  
V=V+TEMP\*YT2  
FI=I  
UX=UX+FI\*XT\*TEMP

ORIGINAL PAGE IS  
OF POOR QUALITY

```

      UY=UY-FI*YT*TEMP
      XT=XT2
70  YT=YT2
      SUMSQ=UX*UX+UY*UY
      IF(SUMSQ) 75,110,75
75  DX=(V*UY-U*UX)/SUMSQ
      X=X+DX
      DY=-(U*UY+V*UX)/SUMSQ
      Y=Y+DY
78  IF(DABS(DY)+DABS(DX)-1.0D-05) 100,80,80
C
C      STEP ITERATION COUNTER
C
80  ICT=ICT+1
      IF(ICT-500) 60,85,85
85  IF(IFIT)100,90,100
90  IF(IN-5) 50,95,95
C
C      SET ERROR CODE TO 3
C
95  IER=3
      GO TO 20
100 DO 105 L=1,NXX
      MT=KJ1-L+1
      TEMP=XCOF(MT)
      XCOF(MT)=COF(L)
105 COF(L)=TEMP
      ITEMP=N
      N=NX
      NX=ITEMP
      IF(IFIT) 120,55,120
110 IF(IFIT) 115,50,115
115 X=XPR
      Y=YPR
120 IFIT=0

```

ORIGINAL PAGE IS  
OF POOR QUALITY



```

122 IF(DABS(Y)-1.0D-4*DABS(X)) 135,125,125
125 ALPHA=X+X
    SUMSQ=X*X+Y*Y
    N=N-2
    GO TO 140
130 X=0.0
    NX=NX-1
    NXX=NXX-1
135 Y=0.0
    SUMSQ=0.0
    ALPHA=X
    N=N-1
140 COF(2)=COF(2)+ALPHA*COF(1)
145 DO 150 L=2,N
150 COF(L+1)=COF(L+1)+ALPHA*COF(L)-SUMSQ*COF(L-1)
155 ROOTI(N2)=Y
    ROOTR(N2)=X
    NZ=N2+1
    IF(SUMSQ) 160,165,160
160 Y=-Y
    SUMSQ=0.0
    GO TO 155
165 IF(N) 20,20,45
    END

```

ORIGINAL PAGE IS  
OF POOR QUALITY